

ISSN • 2708-6437 (Online)  
• 2708-6429 (Print)

# Journal of Engineering Advancements

**Editor-in-Chief:**

**Prof. Dr. Mohammad Mashud**

**Volume 04 Issue 04**



**Published by:  
SciEn Publishing Group**

# Journal of Engineering Advancements

Apt. # 6 C-D, House # 191  
Road # 12/A, Dhanmondi R/A  
Dhaka-1209, Bangladesh

Email: [jea@scienpg.com](mailto:jea@scienpg.com)

Website: [www.scienpg.com/jea/](http://www.scienpg.com/jea/)

---

## *Editor-in-Chief*

Prof. Dr. Mohammad Mashud  
The University of Texas at El Paso, USA  
Email: [mmashud@utep.edu](mailto:mmashud@utep.edu)

## *Executive Editors*

Prof. Dr. Md. Arifuzzaman  
Khulna University of Engineering & Technology  
Khulna-9203, Bangladesh.  
Email: [arif48@me.kuet.ac.bd](mailto:arif48@me.kuet.ac.bd)

Prof. Dr. Md. Shariful Islam  
Khulna University of Engineering & Technology  
Khulna-9203, Bangladesh.  
Email: [msislam@me.kuet.ac.bd](mailto:msislam@me.kuet.ac.bd)

## *Editors*

Dr. Miklas Scholz  
University of Salford  
Email: [m.scholz@salford.ac.uk](mailto:m.scholz@salford.ac.uk)

Dr. Yasuhiro Okamura  
The University of Tokushima  
Email: [okamura.yasuhiro@tokushima-u.ac.jp](mailto:okamura.yasuhiro@tokushima-u.ac.jp)

Dr. Abul Mukid Mohammad Mukaddes  
Shahjalal University of Science and Technology  
Email: [mukaddes1975@gmail.com](mailto:mukaddes1975@gmail.com)

Dr. Seock Sam Kim  
University Malaysia Sabah  
Email: [sskim@ums.edu.my](mailto:sskim@ums.edu.my)

Dr. Mesbahuddin Chowdhury  
University of Canterbury  
Email: [mesbahuddin.chowdhury@canterbury.ac.nz](mailto:mesbahuddin.chowdhury@canterbury.ac.nz)

Dr. Chu Chi Ming  
University Malaysia Sabah  
Email: [chrischu@ums.edu.my](mailto:chrischu@ums.edu.my)

Dr. Sabuj Mallik  
University of Derby  
Email: [s.mallik@derby.ac.uk](mailto:s.mallik@derby.ac.uk)

Dr. Mohammad H. Rahman  
University of Wisconsin-Milwaukee  
Email: [rahmanmh@uwm.edu](mailto:rahmanmh@uwm.edu)

Dr. Sivakumar Kumaresan  
University Malaysia Sabah  
Email: [shiva@ums.edu.my](mailto:shiva@ums.edu.my)

Dr. Monir Hossen  
Khulna University of Engineering & Technology  
Email: [mhossen@ece.kuet.ac.bd](mailto:mhossen@ece.kuet.ac.bd)

Dr. Mohd Suffian Bin Misaran  
University Malaysia Sabah  
Email: [suffian@ums.edu.my](mailto:suffian@ums.edu.my)

Dr. Md. Mizanur Rahman  
World University of Bangladesh  
Email: [mizanur.rahman@mte.wub.edu.bd](mailto:mizanur.rahman@mte.wub.edu.bd)



Published in: December 2023

Published by: SciEn Publishing Group

Price: Each Issue BDT 200.00 (US\$ 15)

ISSN: 2708-6437 (Online) 2708-6429 (Print)

# Journal of Engineering Advancements

Apt. # 6 C-D, House # 191  
Road # 12/A, Dhanmondi R/A  
Dhaka-1209, Bangladesh

Email: [jea@scienpg.com](mailto:jea@scienpg.com)

Website: [www.scienpg.com/jea/](http://www.scienpg.com/jea/)

---

Dr. Zahir Uddin Ahmed  
Khulna University of Engineering & Technology  
Email: [zuahmed@me.kuet.ac.bd](mailto:zuahmed@me.kuet.ac.bd)

Dr. Riaz U. Ahmed  
University of Wisconsin-Green Bay  
Email: [ahmedm@uwgb.edu](mailto:ahmedm@uwgb.edu)

Dr. Mohammad Ilias Inam  
Khulna University of Engineering & Technology  
Email: [iliasinam@me.kuet.ac.bd](mailto:iliasinam@me.kuet.ac.bd)

Dr. Kazi Mostafijur Rahman  
Khulna University of Engineering & Technology  
Email: [mostafij@me.kuet.ac.bd](mailto:mostafij@me.kuet.ac.bd)

Dr. Md. Mahfuz Sarwar  
AECOM  
Email: [mahfuzsarwar@yahoo.com](mailto:mahfuzsarwar@yahoo.com)

Dr. Md. Rashedul H. Sarker  
University of Indianapolis  
Email: [sarkerm@uindy.edu](mailto:sarkerm@uindy.edu)

Dr. Md. Abdullah Al Bari  
University of Calgary, Canada  
Email: [mdabdullahal.bari@ucalgary.ca](mailto:mdabdullahal.bari@ucalgary.ca)

Dr. Md. Najmul Hossain  
Pabna University of Science & Technology  
[najmul\\_eece@pust.ac.bd](mailto:najmul_eece@pust.ac.bd)

Dr. Shehata Eldabie Abdel Raheem  
Assiut University  
Email: [shehatarahem@gmail.com](mailto:shehatarahem@gmail.com)

Dr. Yakubu Ajiji Makeri  
King Ceasor University  
Email: [icydtorg.ug@gmail.com](mailto:icydtorg.ug@gmail.com)

Dr. Smita A Francis  
Namibia University of Science and Technology  
Email: [smitafrancis@gmail.com](mailto:smitafrancis@gmail.com)

Dr. Md Rafiqul Islam  
University of Technology Sydney (UTS), Australia  
Email: [mdrafiqul.islam@uts.edu.au](mailto:mdrafiqul.islam@uts.edu.au)

---

# Journal of Engineering Advancements

Volume 04, Issue 04

December 2023

## CONTENTS

### Original Articles

Sl. No.	Paper Title and Authors	Page No.
01.	Effect of Nano-filler on the Manufacturing and Properties of Natural Fiber-based Composites: A Review <i>Md Sanaul Rabbi, Snigdha Das, Tasfia Tasneem, M Maruf Billah, Afnan Hasan</i>	101
02.	Optimal Tuning of a LQR Controlled Active Quarter Car System Using Global Best Inertia Weight Modified Particle Swarm Optimization Algorithm <i>Oghenenyoreme Emakpo Agbroko, Erastus Olarewaju Ogunti</i>	116
03.	Development of a Weighted Productivity Model for a Food Processing Industry <i>B Kareem, A S Ilori, A S Lawal</i>	124
04.	Design and Performance Analysis of Defected Ground Slotted Patch Antenna for Sub-6 GHz 5G Applications <i>Md. Najmul Hossain, Al Amin Islam, Md. Abdur Rahim, Md. Imran Hossain, Md. Arifour Rahman</i>	130

# Journal of Engineering Advancements

## Editor-in-Chief

Prof. Dr. Mohammad Mashud  
Department of Mechanical Engineering,  
Khulna University of Engineering & Technology, Khulna, Bangladesh

## Executive Editors

Prof. Dr. Md. Shariful Islam  
Department of Mechanical Engineering,  
Khulna University of Engineering & Technology, Khulna, Bangladesh

&

Prof. Dr. Md. Arifuzzaman  
Department of Mechanical Engineering,  
Khulna University of Engineering & Technology, Khulna, Bangladesh



**Published by: SciEn Publishing Group**

Apt. # 6 C-D, House # 191, Road # 12/A  
Dhanmondi, Dhaka-1209, Bangladesh  
Email Address: [jea@scienpg.com](mailto:jea@scienpg.com)

[www.scienpg.com/jea/](http://www.scienpg.com/jea/)

This page is left intentionally blank

# Effect of Nano-filler on the Manufacturing and Properties of Natural Fiber-based Composites: A Review

M S Rabbi<sup>1,\*</sup>, Snigdha Das<sup>1</sup>, Tasfia Tasnim<sup>2</sup>, M Maruf Billah<sup>1</sup>, Afnan Hasan<sup>1</sup>

<sup>1</sup>Department of Mechanical Engineering, Chittagong University of Engineering & Technology, Chattogram 4349, Bangladesh

<sup>2</sup>Department of Mechanical Engineering, Bangladesh Army University Science & Technology, Saidpur 5311, Bangladesh

Received: July 09, 2023, Revised: September 02, 2023, Accepted: September 02, 2023, Available Online: November 04, 2023

## ABSTRACT

Natural fiber reinforced polymer composite offers ecological safety towards a sustainable environment. Meanwhile, the deficiency of the poor interfacial bonding between fiber and matrix draws the attention of researchers to be sorted out. The use of inorganic nanofiller is considered as a possible solution to overcome the hurdle nowadays besides strengthening the composite properties. This article thoroughly reviews the use of inorganic nanofillers in natural fiber composites, covering different manufacturing processes and properties. Factors of various manufacturing techniques occupied for composite fabrication are investigated. Moreover, the influences of different nanofillers on mechanical, thermal, chemical, and physical properties of composites are discussed. In addition, Scanning Electron Microscopy (SEM) images of the bio composites are critically reviewed that usually exhibit the interfacial bonding and the fractures of the specimen. Furthermore, application of such natural fiber composites and the future investigation pathway in using inorganic nanofiller in composite are narrated.

Keywords: Natural Fiber-based Composites, Nanofiller, Manufacturing, Properties



Copyright @ All authors

This work is licensed under a [Creative Commons Attribution-Non Commercial 4.0 International License](https://creativecommons.org/licenses/by-nc/4.0/).

## 1 Introduction

Polymers reinforced with natural fiber are nowadays a challenging and promising field in composite material research due to the rising need for sustainable and biodegradable materials. The policy of using petroleum-based synthetic polymers is under scrutiny in many countries because they are difficult to recycle and environmentally dangerous due to their non-degradability characteristics, which ultimately has a detrimental influence on nature and human health [1]. Natural fiber, on the other hand, is an excellent alternative to synthetic fiber because it is non-toxic, environment-friendly, less expensive, renewable, and recyclable, has superior damping qualities, and is widely available [2]-[4]. Performance of such composites is significantly influenced by the fiber properties (physical, thermal, mechanical, water absorption, etc.), fiber-matrix composition (volume percentage, stacking sequence, fiber orientation, etc.), and surface treatment of fiber [5], [6]. Natural fibers also have high tensile strength which offers their polymer composites good mechanical and thermal properties in applications including automobiles, load-bearing applications, packaging, and aerospace [7],[8]. A study found that using fiber-based composites reduced overall aircraft weight by 35% and had a positive effect on fuel efficiency and performance [9]. Due to these qualities, most of the components used by aircraft producers including Boeing, Dreamliner, and Airbus now employ composites [10]. Furthermore, it's been claimed that employing fiber composite parts can reduce vehicle weight and prices by 20 and 30 percent, respectively [11].

Three fundamental categories, including animal fiber, plant fiber, and mineral fibers, can be used to classify natural fiber [12]. Plant fibers like cotton, flax, hemp, and jute are formed of cellulose, while animal fibers such as hair, silk, and wool are made of proteins. In plant-based composite material, cellulose

containing jute, sisal, banana, bamboo, rice, corn, hemp, kenaf, coir, flax, banana, aloe vera and pineapple are frequently used. Though having several benefits, such composites have several drawbacks, including poor interfacial bonding, dimensional instability, excessive moisture absorption due to the hydrophilicity of the fibers, brittle failure of the polymers, a tendency to aggregate during processing, and average strength [13]-[15]. It is troublesome for industrial and structural applications when the properties of a polymer composite deteriorate due to inadequate interfacial contact between natural fibers (hydrophilic) and a polymer (hydro-repellent) [16].

A variety of methods, including surface modification through chemical or enzymatic treatments, the addition of various interfacial additives or fillers, hybridization, coupling agent addition etc. are highly effective overcoming these difficulties [17]-[19]. The hybrid composite qualities are solely attributed to the fiber content, fiber length, and orientation, as well as the degree of fiber intermingling, fiber arrangement, and fiber-matrix bonding [20]. To adhere the bonding between fiber and matrix, surface treatment of the fiber is often made. Common surface treatments are alkali, silane, acetylation, benzoilation, peroxide, permanganate, and sodium chlorite [16], [21]-[25]. Alkaline treatment is a very well-known and straightforward technique for improving the adhesive properties of the fiber matrix. Commonly, sodium hydroxide (NaOH) is used in this process to change the cellulose structure of natural fibers, accelerating the breakdown and disaggregation of the fibers [26]. During the alkaline process, lignin, pectin, wax, and oil are removed from the fibers, leaving a smooth, clean surface and a higher elasticity [27]. The following chemical reaction happened [24],[28],[29].



Nanocomposites are designed by adding nanoscale fillers to a polymer matrix to fulfill the expanding needs for specific qualities in a variety of industrial and practical applications [30]. Nanocomposite materials have at least one phase with a dimension of 100 μm or less [20]. Mechanical, optical, electrical, magnetic, and thermal characteristics of nanomaterials are different from those of pure polymers [31]-[33]. Therefore, these particular properties can be improved by incorporating nanofillers, enabling a wider range of applications [28],[34],[35]. Numerous research is currently being conducted on different filler materials. Chowdary et al. [36] examined the influence of nano-silica on Sisal/Kevlar composites and found out that at 4% nano-silica addition, mechanical strength improved by a significant percentage. In the addition of nano-silica, thermal, flammability, and morphological characteristics of the composites are improved [37]. The incorporation of nano-clay considerably improved the fibers-matrix interface adhesion and compatibility of kenaf-coir hybrid composites [38]. Impact strength increases and water absorption percentages decrease with the increasing number of nanoparticles [39].

This study provides a comprehensive review of mechanical, thermal, and morphological studies on nanocomposites made from natural or bio fibers, various types of fabrication processes, and the application of the nanocomposites in different sectors.

**2 Nanocomposites: Types and Properties**

Nano-sized silica, zinc, alumina, titanium dioxide, calcium carbonate, lead oxide, silicon carbide, carbon black, nano clay, and various kinds of nanofibrils and cellulose nanocrystals are commonly incorporated in composite materials. They can be differentiated as organic and inorganic nanofillers. Different types of nanofillers that improve material characteristics without sacrificing density, toughness, or processability [12], [40] are depicted in Fig 1. Modern microscopic techniques such as SEM, TEM, STM, NMR, XPS, WAXS, AFM, DSC, and FTIS are commonly used to analyze nanoparticles [25], [41].

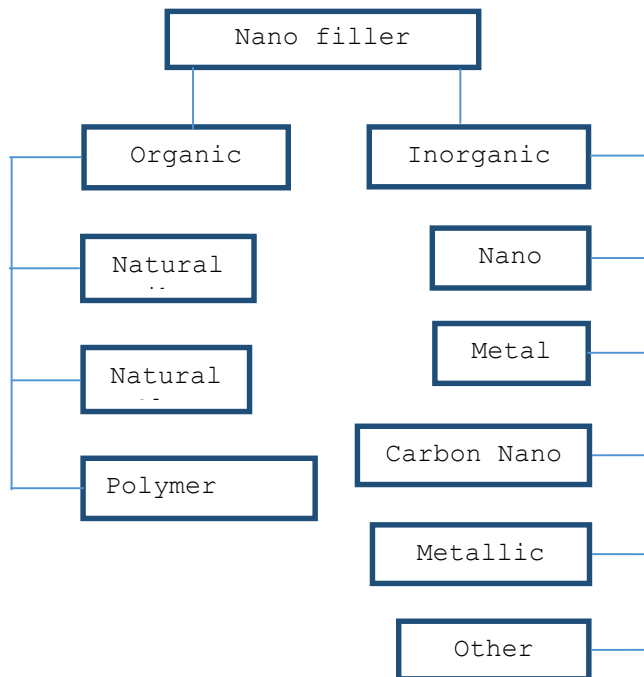


Fig 1 Different types of organic and inorganic filler material [42]

Nanoscale fillers have an extremely high surface-to-volume ratio due to their properties such as catalytic reactivity, electrical and chemical resistivity, etc., [43],[44]. Adding nano fillers provides a large interaction zone between them which involves several interaction mechanisms, particularly based on the type and nature of the filler and matrix used. The schematic interpretation of filler-matrix interaction is interpreted in Fig 2. Significant improvements in crystallinity, the formation process, the polymer chain's order, chemical properties and corrosion resistance are also addressed [45],[46]. At the nanoscale, quantum confinement, energy quantization, molecular mobility, and electromagnet forces become more prominent. As a result of these processes, there will be an increase in intermolecular bonding, hydrogen bonding, van der Waals, hydrophobic effect, catalysis, magnetism, surface energy, and other effects. Based on the effects of hydrophobicity, catalysis, hydrogen bonding, surface energy, etc., nanotechnology and nanostructured materials have been developed [42]. Due to the very small number of nanoparticles introduced in comparison to the bulk phase, the material weight also decreases [14]-[16]. However, the incorporation of higher filler concentration may cause in more microscopic voids, eventually lowering the properties due to weaker bonding between the reinforcement and matrix [47],[48].

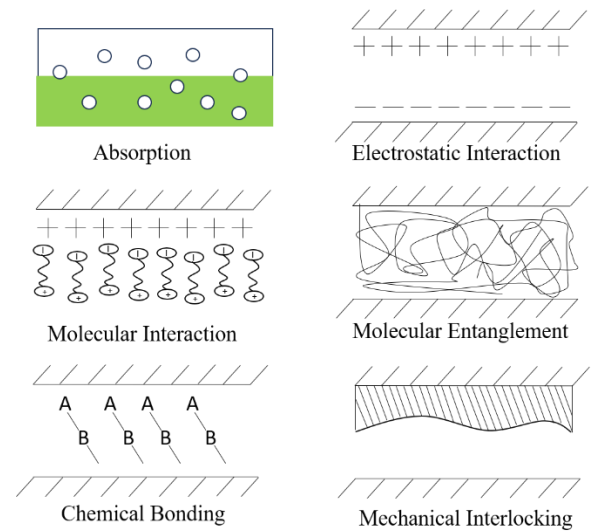


Fig 2 Schematic of the interaction mechanism at the fiber-matrix interface [49]

Aside from these, nanoscience and nanotechnology researchers have recently become interested in cellulose-based nanomaterials because of the abundance of renewable natural sources [50]. The terms nanocellulose and "nano-fibrillated cellulose" are usually used to describe cellulose nanofibers (CNF) and cellulose nanocrystals/whiskers (CNC). In the host polymer matrix, CNC exhibits a strong propensity for self-association, which is helpful for the development of load-bearing percolating structures [51]. Various techniques, including chemo-mechanical, grinding, cryo crushing, micro fluidization, and ultrasonication have been used to create CNFs from natural fibers [52]-[54] while CNCs are commonly produced using acid hydrolysis of cellulosic materials dispersed in water [55]. Notable properties of Poly Vinyl Alcohol (PVA) based nanocomposites reinforced with sugarcane bagasse nanocellulose investigated by Mandal et al. [56] and it was found that Crosslinked PVA and linear PVA nanocomposite exhibited the highest tensile strength at 5 wt.% and 7.5 wt.%

of nanocellulose respectively. Rosamah et al. [57] examined the impact of bamboo nanocellulose in kenaf fiber-polyester composite. It was found that the addition of 3% of nanofillers contributed to a strong bonding and increased wettability with the matrix, resulting in superior mechanical properties and thermal properties of the composite.

### 3 Manufacturing Techniques

In general, the manufacturing process of nanocomposites is like that of conventional polymer composites. Before compounding the matrix with the fiber, nanoparticles are usually mixed with the matrix using various stirrers as per the required proportion. Common compounding techniques are single/twin screw extruders, two- and three-roll mill ball machines, Brabender, Ragogna, and HAAKE mixers, k-mixers, mechanical and magnetic stirrers, and other common pieces of machinery are some of the prominent ones used to compound filler and polymer matrix [38],[58]-[62]. Nowadays, mixing matrices with nanomaterials frequently involves the use of mechanical stirrers and ultrasonic probes [38],[63]-[67]. To introduce specific nanofillers into the matrix and to prevent contamination, uniform dispersion of nanofillers is a crucial step in the manufacturing of nanocomposites [42].

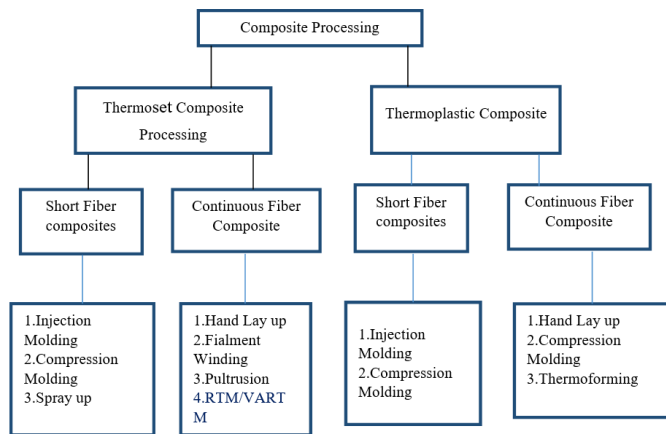


Fig 3 Various fabrication processes of composite

Fig 3 depicts the types of manufacturing techniques where nanoparticles can take place as fillers.

#### 3.1 Hand lay-up

The Hand Lay-up technique can be used to manufacture hybrid composites using long natural fibers, although this method does not permit considerable fiber loading [68],[69]. Nanoparticles are inserted in the sample by mixing the particles with a matrix with an appropriate ratio. Samples are used to be cured at room temperature [70]. Modern technologies for curing composite parts include autoclaves, electron beams (E-beam), microwaves, X-rays, and ultraviolet (UV) light [71]. This approach is constrained by factors like the greater possibility of voids due to the uneven distribution of resin. Mixing of resin and the composition is crucial in this labor-intensive process [69]. The composite quality is significantly influenced by fiber loading. Additionally, this is influenced by the fibers' physical traits, such as the lumens in their intra-fiber gaps.

#### 3.2 Compression Molding

A common method of producing high-volume natural fiber-reinforced polymer nanocomposite is compression molding [72]. Fabrication of natural fiber-reinforced nanocomposites typically

involves preheating the fiber components, followed by compression at high pressure until solidification takes place [16],[73]. The hot and cold compression methods are two different ways to produce the composite by this technique. Using two flat plates, the mixture is compacted in hot compression before being heated to cure it. Consequently, in this process, both pressure and temperature are required at the same time, in contrast to cold compression curing, which occurs at room temperature and only uses pressure [69].

Less waste, excellent productivity, and high repeatability are all present together with low cycle time and cost [71],[74]-[76]. Because the components are placed carefully, there is relatively little fiber damage throughout the composite's production process. Long and short fibers can both be employed as reinforcement; however short natural fibers can be pre-combined with resin and nanofiller to lessen the shrinkage of the final specimen [72]. This method is primarily suitable for fabricating small parts [69]. Molding conditions, curing temperature, heating time, interfacial interaction between fiber and matrix, and cooling time are all different factors that should be considered. A careful consideration of temperature is required since, in general, there is a small gap between the processing temperature of a given matrix and the temperature at which fiber deterioration will take place [77]. The tensile strength of fibers is demonstrated to be reduced at temperatures between 150° C and 200° C, with a 10% decline in strength occurring in just 10 minutes [78]. However, depending on the sheet's thickness and the material used, these variables may change [79].

#### 3.3 Resin Transfer Molding Process

Resin transfer molding (RTM) has recently gained a lot of popularity for fabricating high-performance thermosets. A mechanically clamped, stiff, closed mold is used in which long or weaved fibers are inserted. Then, at low pressure, the resin, nanoparticles, and other additives are pressed into the mold holding the preform, and then heat is applied to solidify them [80]. The items produced with this technique feature great surface finishing, good dimensional tolerances, minimal void content, cheap tooling costs, nearly no air entrapment, and no thermomechanical degradation [74],[81]. Major challenges to this method are the need for resin with low viscosity, variation in the composite part's thickness as a result of uneven compaction pressure, less productivity, and poor shrinkage quality [82],[83],[84]. Low viscous resins are commonly used in this process. Mold configuration, resin properties, resin preheated temperature, injection pressure, and fiber content all affect this technique [85],[86]. Due to lower degrees of fiber alignment, natural fiber composites are less compactable than glass fiber composites during this phase where the structure of the fibers, particularly the impact of lumen closing, influences the compaction [87]. However, a high injection pressure could result in the fiber preform being washed out of the mold and deformed. Premature resin gelation and short shot can be caused by an extremely high mold temperature. Each process variable is connected to the others and influences how final goods behave mechanically [88].

The RTM process known as VARI/VARTM is one of the new molding technologies that is expanding very fast. The main distinction between the two is that resin is injected under pressure in RTM rather than employing a vacuum and high heat or pressure [71]. The VARTM process creates a vacuum-tight seal. Typically, a "manifold" made up of several carefully placed ports and feed lines allows resin mixed with additives to enter the

structure. A vacuum pump is typically used to remove the air [89],[90]. Air cavities can thus be minimized to the point that the resulting composite part has little open space, producing composite products with superior mechanical properties [91],[92]. A network of internal passages helps to wet out the fibers as it is pulled into the reinforcements by vacuum. For the impregnation of the fiber tows during the VARI process, the capillary effect of natural fibers was crucial [52]. With the use of VARTM's low-cost tooling, it is affordable to make large, complex parts with a larger fiber volume fraction in a single step [93]. They do, however, have several disadvantages, such as thickness variance, poor surface smoothness, installation challenges for supplemental equipment, such as sealant tape, porous peel ply, vacuum bag, distribution medium, and breather, non-reusability, high waste production, etc. [94],[95].

### 3.4 Spray Up Method

In this process the fiber can be uniformly encapsulated into the polymer matrix directly through spray drying [76]. The mold is initially prepared with mold release and gel coat. Then, using a handgun, resin, nanoparticles, and finely chopped fiber are sprayed into the mold. The fiber is then aired out and moistened using a roller and brushes. It is then possible to add a second layer made of wood, foam, or another core material. After that, the portion is dried, chilled, and taken out of the reusable mold [71]. This approach only provides one-sided surface finishing and uses low viscosity resin, which is not suited for high dimensional accuracy items [72],[75]. Before the specimen is completely cured, the sprayed fiber and resin combination is rolled to prevent bubbles and voids [96].

### 3.5 Pultrusion

Pultrusion is a continuous method for producing composites with unique cross-sections and long lengths [97]. It is the best approach for large-scale, swift, long, and consistent cross-sections of parts and continuous composite in any dimension [71],[75]. In this technique, warmed dies are used to force integrated continuous fibers through a heated resin-nano filler solution. Material is subsequently molded into the desired shape after passing through several forming guides. The finished shape is then cut to the correct length after cooling employing a cut-off saw [98]. Pulling is done to prevent fiber damage. As matrices, epoxies, polyester, phenol, and vinyl ester are frequently utilized. The advantages of this approach include stronger strength, better surface finishing, thin wall construction, a wide range of cross-sectional forms, less fiber damage and the potential for a high level of automation [75],[79]. The mechanical qualities are impacted by variables like die temperature, pulling rate, and fiber content. The qualities are found to increase with higher die temperatures, higher fiber contents, and lower pulling rates. Post-curing is also a useful tool for enhancing the characteristics [99].

### 3.6 Injection Molding

One of the quickest mass production methods for intricate parts with a range of sizes and forms and minimal labor costs is injection molding [100]. Injection molding is superior to other processes in several ways, including mass production, a shorter production cycle, and tighter tolerances for complicated products [101]. Through a feed hopper with a funnel-like shape and a rotating twin-screw extruder, the fibers-typically pellets containing chopped fibers, nanoparticle mixed with resin are fed individually into a heated compression barrel. Through thermal compression, the pellets are forced into closed mold cavities made of matching metals, which facilitates thoroughly transferring the stress from matrix to fiber. The polymer solidifies inside the mold, which is tightly pushed against injection pressure. After proper solidification, the mold is removed from the closed mold with the proper shape [72]. The resulting products have a high level of surface finish and outstanding dimensional precision, and this process works with both thermoset and thermoplastic composites. It is a very significant and productive technique for making everything from very small things like bottle tops to extremely huge automotive body sections [79]. The critical length of the fiber, fiber content, residual stress, mold temperature, injection pressure and cooling time are some significant parameters that need to be controlled [102],[103]. If the fiber exceeds the critical length and may risk breaking before the matrix fails. The modulus distribution of the composites is impacted by residual stress and fiber orientation [104].

### 3.7 Filament Winding

Although filament winding has received very little research so far, it is a viable alternative for producing symmetrical and convex-shaped components [105],[106]. It is a continuous fabrication technique that is inexpensive to fabricate highly automated, and reproducible. The technology for continuous thermosetting resin adhesive-impregnated synthetic fiber winding is quite advanced [107],[108]. The mandrel rotational rate and the way the fiber is fed into the mandrel both affect how the fiber is oriented in this procedure. In the x-direction, fibers that have been resin-impregnated are coiled and formed around a revolving mandrel. To regulate the resin in this process, nips and dies are employed. Inside the oven, the damaged area is repaired [75]. This method is quick and economical. Discontinuation of natural fiber is the limitation of this process. To prepare continuous pre-preg belts, natural fibers can be twisted or weaved. Most frequently preferred are roving or stand fibers coupled with low-viscosity resins. The filament winding method, which is quick and affordable, is used to create pipelines, oxygen tanks, etc.

A summary of the various types of Fabrication processes with their benefits and limitations are listed in Table 1.

Table 1 Various manufacturing techniques along with their relative advantages and limitations

Process	Fiber type	Curing Temp. and pressure	Advantages	Limitations
Hand Lay-up	Long, short, woven	Room/High temp	Suitable for large components parts.	Heterogenous distribution of Resin.
Compression Molding	Long and short	High temperature and pressure for hot compression and room temp. for cold compression	Less cycle time, cost and waste, High productivity, and Reproducibility.	Suitable for small parts' production.
RTM	Long/woven	Room temp. and high pressure	Good surface finish, fewer voids, less waste, and less tooling cost.	Less productivity and low shrinkage quality.
VARI/VARTM	Long/woven	High heat and pressure	Excellent mechanical qualities, Fewer voids.	Bad surface finish, Thickness variation, High Waste.

Process	Fiber type	Curing Temp. and pressure	Advantages	Limitations
Spray Up	Short	Room temperature	Low cost, large product components.	One-sided surface finishing, difficulties in fiber volume and thickness control, unsuitable for high dimensional accuracy parts.
Pultrusion	Long and continuous	Controlled temperature	Higher strength, better surface finishing, thin wall structures, a large variety of cross-sectional shapes.	High tooling cost, restriction for a particular type of cross-section Components.
Injection Molding	Chopped	High injection pressure and high heat	Low labor cost, high quality of surface finish, and excellent dimensional accuracy.	High Initial cost, limitation in mold design.
Filament Winding	Long continuous, roving or stand fiber	Room temp. and pressure	Convenient for symmetrical and convex-shaped parts, comparatively economical.	Difficult to manufacture.

#### 4 Mechanical Properties

It is reported by numerous researchers regarding the enhancement of mechanical properties by incorporating nano clay, nano silica, carbon nanotubes and other nano metal oxides as well as nano cellulose [109], [110]-[114]. In Jute fiber with nano clay, the tensile properties show the best results for 30 mm fiber length and nano clay of 5 wt.% [115]. For Nano clay infused banana fiber composite the compressive properties were enhanced by about 28%, Young's modulus increased by 25% and maximum strain energy shown in tensile mode increased from 19.27 J/m<sup>2</sup> to 71.83 J/m<sup>2</sup> when compared with pristine banana fiber composite [60]. The hybrid composite composed of 2 wt.% of MMT (montmorillonite-clay) with 5 wt.% of curauá fiber exhibited the best mechanical performance. Adding TiO<sub>2</sub> in epoxy polymer causes higher reluctance to impact effect during 5% volume fraction of TiO<sub>2</sub> and the property decreases with the increased portion of TiO<sub>2</sub>. By increasing the value, this behavior was found to be the same as pristine epoxy when the volume percentage reaches 10% TiO<sub>2</sub> [116]. Effect of 2 wt.% to 3 wt.% nano clay on the mechanical properties of bamboo fiber-reinforced composite was found significant [117]. It is reported that the flexural performance of Napier grass-based composite is improved by incorporating of 3 wt.% of nano clay [118]. The tensile modulus retain rate was improved by 33.8% after the grafting of nano-clay into flax fiber-based epoxy [119]. Hybrid composite characterization with 10% epoxidized soybean oil and 1.5 wt.% nano clay causes retention of the real stiffness while improving toughness [120]. Nano clay inclusions of 5 wt.% in curauá fiber-based polyester composites reinforced enhance the tensile strength by 39.22% and flexural behavior by 25.43 % [121]. A hybrid composite of pineapple leaf fiber and polypropylene matrix with nano clay produces better mechanical response [122].

Alongside TiO<sub>2</sub>, SiO<sub>2</sub>, Al<sub>2</sub>O<sub>3</sub>, and ZnO metallic oxides, inorganic nano-sized powders are used as nano-fillers in different natural fiber nanocomposites. Stiffness behaviors are mostly enhanced by adding these particles with various polymer matrices. Reduction in crack growth, better interfacial bonding and lamination in basalt fiber-based composite was noticed when it was doped with SiO<sub>2</sub> powder. Adding TiO<sub>2</sub> in epoxy polymer causes higher reluctance to impact effect during 5% volume fraction of TiO<sub>2</sub> and the property decreases with the increased portion of TiO<sub>2</sub> [116]. By increasing the value, this behavior was found to be the same as pristine epoxy when the volume

percentage reaches 10% TiO<sub>2</sub>. When nano-SiO<sub>2</sub> of 5 wt.% was added to bagasse fiber-reinforced composites, MOE increased by 221.84 percent in comparison to pure HDPE. The flexural strength and modulus of rupture (MOR) of the composites improved as the nano-SiO<sub>2</sub> concentration of the composites increased [123]. When bagasse fibers and nano-SiO<sub>2</sub> (5 wt.%) are combined, the tensile modulus of pure HDPE is increased threefold [113].

Behzad Kord et al [124] examined the influence of including nano-SiO<sub>2</sub> on mechanical and physical properties of hemp fiber-based polypropylene composite. They concluded that the tensile strength and modulus improved up to 3% loading percentage of nano-infusion and then decreased. On the other hand, Singh et al. [125] found that in case of hemp-sisal-based epoxy hybrid composite with 0-4 wt.% of nano-silica inclusion, the addition of 2 wt.% nano-silica revealed higher tensile and impact strengths and 3 wt.% of nano-silica showed highest flexural properties. The addition of bamboo nanoparticles of concentration (0-5) wt.% into kenaf/unsaturated polyester natural composite results in the enhancement of mechanical characteristics for up to 3 wt.% of bamboo nano-infusion in the experiment conducted by Rosamah et al. [57]. Zhou et al. [126] added a small amount (0-1wt%) of CRN (carbonized ramosissima nanoparticles) in the bamboo fiber-reinforced epoxy composite. In this study, the tensile properties increased by 18.35% when CRN was 0.5 wt.% and shear strength was maximum for 0.25 wt.% which was increased by 38.96%. Ghalenho et al. [127] studied pine wood/polyethylene with a different weight percentage of TiO<sub>2</sub> nanoparticles (0%, 1%, 3%, and 5%) where the highest tensile and bending strength was achieved for 3 wt.% of TiO<sub>2</sub> through the addition of TiO<sub>2</sub> nanoparticles lowered the impact strength due to the higher brittleness. Sumesh et al. [128] examined the effect of nano-alumina up to 3% mass fraction on hybrid banana coir, hybrid sisal coir and hybrid sisal banana composites. The study showed improved results for mechanical properties but due to agglomeration, these characteristics tend to decrease at 5 wt% nano-addition.

The influences of nano-fillers (metal oxides, nano clay cellulosic fibers, carbon nanofibers) are shown in Table 2. In most cases, 1-5wt.% of nano clay and metal oxides were used and showed some prominent results. In the case of nano-graphene addition, positive results were achieved using 0-2% weight percentage. However, exceptions were found for nano-cellulose as it is sometimes used as reinforcing material for composites.

Table 2 Influence of various nano materials on the mechanical properties of natural fiber

Fiber	Fiber content	Matrix	Manufacturing method	Nanofiller (%wt.)	Tensile strength (MPa)	Tensile modulus (G Pa)	Flexural Strength (MPa)	Flexural modulus (G Pa)	Impact Strength (kJ/mm <sup>2</sup> )	Ref.
Banana	40 vol%	Epoxy	Hand Layup	Na <sup>+</sup> Cloisite (3%)	173	10	88	8.102	—	[60]
Agave	—	epoxy	Vacuum Assisted Resin Infusion (VARI)	ZnO (2%)	23	2.8	—	—	—	[129]
<i>Coccinia indica</i>	—	Epoxy	Hand Layup and Compression molding	Cloisite 30B (3%)	38.29	—	92.77	—	67.25E-6	[130]
Curaua	5 wt. %	SBS	Melt blending	Cloisite 10A (2%)	7.8 ± 0.2	4.8 ± 0.2E-3	—	—	2	[121]
Vakka	44 wt. %	Polyester	Hand layup	Nanoclay	94.75	2.486	145.67	145.67	—	[110]
Ginger	—	Polyvinylidene fluoride	Sol-gel technique	Nano-silica (0-1%)	8-13	—	—	—	—	[131]
Jute fabric mat	41 g	Polyester	Compression molding	MMT K10/Egg shell powder (±1.5%)	29.5 ± 0.24	—	39.52 ± 0.52	—	0.312 ± 0.018	[132]
Woven basalt fibers	50 wt. %	Aluminum-Epoxy	Hand layup	MMT K10 (5%)	—	—	641.30 ± 11.56	122.22 ± 2.55	—	[133]
Sugar palm	—	Polyester	Hot pressing	OMMT (4%)	24.56	3.683	68.12	3.786	69.19E-6	[134]
Jute	—	Natural rubber	Roll-milling mixing	Cellulose nanocrystals (CNC) (5%)	21.8±0.7	—	—	—	—	[135]
Jute	—	Polyester	—	Bentonite	40.39	2.62	337.93	12.51	0.157	[136]
Sisal	40 wt. %	rPP	Compression molding	Cloisite 30B (5%)	55.95	1.7003	—	—	8.76E-6	[59]
Sawdust	80%	epoxy	Compression molding	ZnO (5%)	—	—	89.60	—	3.82	[137]
Sisal	50 wt. %	Epoxy	Vacuum-assisted resin infusion molding	Cloisite 30B (3%)	55	23	—	—	—	[60]
Hemp	21 wt. %	Polyester	Compression molding	Cloisite 30B (1.5%)	24	6	—	—	—	[120]
baggage	15-30%	Polypropylene	Injection Molding	Nano-graphene (0-1%)	32-46.3	2.2-3.4	55-59	1.8-2.6	39-44 J/m	[138]
Rice straw	40%	Polypropylene	Injection Molding	Nano-silica (0-3%)	—	2.3-2.5	—	1.9-2.8	20.5-21.5 J/m	[139]
Coir	30 wt. %	Polypropylene	Hot pressing	MMT (2%)	9	3	—	—	—	[140]
Wood	30 wt. %	Polypropylene	Hot pressing	MMT (0-2%)	12	4	—	—	—	[140]
Coir fiber	0-10%	Synthetic epoxy	Hand layup	TiC nanoparticle (0.5,10%)	30-58	1.2-2.2	115.05-124	3.9-4.8	4.5-8.8 kJ/m <sup>2</sup>	[67]
Pineapple leaf	30 wt. %	Polypropylene	Compression molding	Cloisite 20A (3%)	45.14	6.45	65.01	4.46	—	[122]
Kenaf	30%	Unsaturated Polyester	Hand-layup	ZnO (5%)	58	5.60	68	13	31	[114]
Jute	20 wt. %	Epoxy	Hand layup and Compression molding	Cloisite 20A (5%)	103.05	1.298	162.8	2.8	0.358	[110]
Curauá	10-30 wt. %	Polyester	Cold Pressing	Organophilic Clay (2.5-10%)	36.13	—	32.55	—	—	[121]

Fiber	Fiber content	Matrix	Manufacturing method	Nanofiller (%wt.)	Tensile strength (MPa)	Tensile modulus (G Pa)	Flexural Strength (MPa)	Flexural modulus (G Pa)	Impact Strength (kJ/mm <sup>2</sup> )	Ref.
Coconut (coir pith)	—	Polyester	Hand layup	Nano-alumina (1%)	46	—	83.1	—	—	[141]
Hemp	—	epoxy	Hand layup	Graphene (0.3%)	68	—	47.22	—	—	[142]
Luffa fiber	20%	epoxy	Hand layup	Graphene (2%)	12.228	2.10	67.05	—	3.548	[29]
Flax/PLA	28%	epoxy	Vacuum Bagging	Al <sub>2</sub> O <sub>3</sub> , MgO (3%)	46, 50	4.2, 5.2	95, 64	5.8, 3.8	70, 76 kJ/m <sup>2</sup>	[34]
Jute	15 wt.%	Polyester	Hand layup	MMT (5%)	40.38	—	234.93	—	—	[34]
Hemp	—	Epoxy	In-situ polymerization	Hemp nano cellulose (2%)	77.09	2.43	95.78	4.14	21.82 kJ/m <sup>2</sup>	[65]
Wild cane grass	40 vol%	Polyester	Compression molding	MMT (4%)	99.57	2.26	221.61	4.192	—	[143]
Sisal	25 wt.%	General polymer	Compression molding	Garamite (3%)	109	—	6980	—	—	[144]
Jute/Coir	105 g fiber/ 630 g of resin	Polyester	Compression molding	Garamite (3%)	43	—	—	—	—	[145]
Wood craft pulp nano-cellulose	5-20%	Polyvinyl alcohol	Mechanical stirring and casting	Nano-silica (5-20%)	2.85-4.69	—	—	—	—	[146]
Sugarcane baggace	—	Poly vinyl alcohol	Mechanical stirring and casting	Sugarcane baggace nano-cellulose (2.5, 5, 7.5, 10%)	41.3-57.7 (linear) 52-83 (crosslinked)	—	—	—	—	[56]
TEMPO-mediated oxidized cellulose nanofibers	—	Polyvinyl Alcohol-Chitosan blend	Mechanical stirring and casting	Cellulose nanofiber (0-1.5%)	15-29	—	—	—	—	[50]
Kenaf, coconut	40%	Polyester	Hand layup	Oil palm sell nanoparticles (1-5%)	30.10±1.03-37.56±1.12	0.76±0.04-1.15±0.05	60.42±2.19-75.27±2.43	4.41±0.24-6.17±0.38	10.84±.56-13.42±0.49	[147]
Basalt fiber	—	Epoxy	Hand layup	Coir micro particles and TiC nanoparticle (5-10%)	46.32±1.09-112.87±5.09	1.5-7.8	60-220	2-11	4.8-27.67±1.14	[67]
Hemp fiber	—	Epoxy	Hand layup	Eggshell nanoparticles (0, 7, 14, 21%)	69.99-74.32	—	170-220	—	6-10	[39]
Flax	—	Epoxy	Vacuum-assisted resin infusion	OMMT (1.3%)	87.5	7.55	140	6.2	—	[119]

## 5 Thermal Properties

Nano clay-infused natural fiber nanocomposites express a higher value of thermal expansion coefficient, enhanced thermal resistance, flammability, and composites [110],[112]. Higher heat deflection temperature of the composites is achieved by these nanofillers which elevated dimensional stability and flame retardation. Moreover, the thermal barrier characteristic is the outcome of the high aspect format of nanoparticles. The larger aspect ratio of nano clay provides a convoluted gateway making it tough for the vapor and gas particles to permeate the composite material [112]. Nanofillers cause layers of lower heat flux over the surface of a material which is used as a fire retardant in composites. These are used as the replacement of halogen to act as a fire inhibitor [148]. The thermal stability of the nanocomposite increased with the addition of Nano cellulose and

Nano oxide silicon, particularly at the 5wt% loading, possibly because of the high thermal stability behavior of Nano silicon dioxide [146]. Three-dimensional inorganic ZnO nanoparticles show better thermal stability in different polymer composites [135]. The existence of ZnO significantly influences the mechanical and thermal properties of kenaf/polyester composites [149].

The effect of nano organic and inorganic particles on the thermal properties of different natural fiber composites was introduced in Table 3. In most of the cases, higher thermal stability was attained for adding (0-5) wt.% of nano-fillers. Furthermore, the thermal degradation temperature was mostly above 300°C for these nanoparticle-aided composites and crystallization temperature and enthalpy were also found higher in several cases.

Table 3 Effect of Nanomaterials on Thermal property of various composites

Nano-filler	Type	Fiber/matrix	Thermal property	Ref.
Nanoclay	organic	Sisal-polypropylene	Higher thermal stability	[59], [150]
Nanoclay-MMT (montmorillonites)	organic	Jute- polypropylene	Better results for 1% and 5% nanoclay in thermogravimetric analysis	[151]
MWCNT (multi walled carbon nanotube)	organic	epoxy	The glass transition temperature, thermal stability and decomposition temperature increased	[148]
ZnO nanoparticles	inorganic	Kenaf/polyester	Significant improvement in thermal stability	[114]
ZnO powder	inorganic	polymer	Enhanced thermal stability	[123]
Nano-alumina	inorganic	Coir/polyester	TGA) and DTG shows highest thermal stability.	[141]
Nanoclay-MMT	organic	Rice husk/high density polyethylene	The crystallization temperature, crystallization enthalpy and crystallinity level increased	[152]
Nano- $Al_2O_3$	inorganic	sisal/coir/epoxy, sisal/banana/epoxy, banana/coir/epoxy	Degradation temperature improved	[153]

## 6 Physical and Chemical Properties

The water absorption capacity of nano clays depends on the number of exchangeable cations in interlayer [148]. Inorganic  $SiO_2$ , ZnO and  $TiO_2$  nanofillers are used as corrosion-resistant substances in organic coatings [135]. The Addition of Montmorillonite nano clay improved the water absorption capability of hybrid composite combinations of various natural fibers (kenaf, coir, and wood) and polypropylene [154]. On the contrary, the addition of montmorillonite nano clay in natural fiber-reinforced hybrid nanocomposites, manufactured by compression molding technique with wood particles, hemp fiber, and polypropylene decreases the water absorption property [99]. Ferric oxides added to fiber boards result in enhanced thickness swelling and water absorption properties. The brittleness of the thermoset can be significantly reduced by adding a metal oxide nanofiller where hardness is improved due to the improved density [135]. It is generally believed that because of the barrier effect of the nano clay, which impedes penetration of  $O_2$  into the sample, the destruction of the nanocomposite occurs at a higher temperature [154]. Besides, natural fibers have better specific properties than synthetic fibers, which in combination with another reinforcing (nanofillers) enhances the performance. Weight gain and FTIR spectrum analysis indicated that 5% nano clay addition gave favorable reduction in the water absorption behaviors of vinyl-ester eco-nanocomposites [155]. Alumina and Magnesia were used as nanofillers and found improved water absorption characteristics in flax/PLA bio composites [156] and jute/epoxy nanocomposite [157].

It is obvious from Table 4 that the hydrophilic characteristics of natural fibers give rise to weight gain whereas the hydrophobicity of nanoparticles reduces the water uptake of the hybrid composites. Moreover, nanoparticles decrease the thickness swelling. The effect continued with increased density and decreased void fraction of the composites by the addition of nanoparticles. The higher percentage of fiber shows higher biodegradability in composites.

## 7 Scanning Electron Microscope (SEM)

Many researchers have presented studies that provide information on the influence of the addition of nanofillers to interactions between the filler and matrix at the interface via SEM analysis. K. R. Sumesh et al. [164] studied the surface property of banana-pineapple fiber after the flexure test with the addition of 0% and 3%  $TiO_2$  nanofiller and it was observed the reduction of void formation and resulting in improved flexural properties (Figure 9). It was reported that the addition of 4 wt.% nano-silica in the kenaf-sisal hybrid composite shows less crack formation after flexural test [165] though fiber pullout was observed.

E. Rosamah et al. [57] analyzed the tensile fracture surface of kenaf/coconut mat with the addition of 0-5% Oil Palm Shell nanoparticles. It was found that an enhanced portion of nano OPS up to 3% provided better matrix formation with reduced voids and fiber fracture. However, after increasing the amount from 3-5%, higher numbers of voids were detected which is probably due to the poor wetting of the fiber due to higher OPS nanoparticles content in the polymer matrix.

In an experiment conducted by K. G. Ashok et al. [29] with the incorporation of PbO nanoparticles with Luffa Fiber, it was figured that pull out of fibers from the surfaces which is due to the agglomeration of nano PbO particles and particle-particle interaction at higher weight percentage, thus restricting the interaction of the nanoparticles with the matrix fiber interface (Figure 10).

From the micrograph of ZnO nanofiller-based composites, it is concluded that the void content decreased with the incorporation of ZnO [163].

Fig 4(a) shows the fractured surface of the Sugar Palm fiber/Polyester composite without any additive whereas Fig 4(b) depicts the composite with 2% nano clay [134]. By investigating the impact energy for both samples, it was reported that the sample without nanofiller exhibits poor interfacial bonding.

Table 4 Effect of nanoparticle in the physical properties of different composites

Nano-filler	Fiber-matrix	Types of tests	Result	Reference
Montmorillonite (2 phr)	Kenaf-coir-polypropylene	Water absorption, Biodegradability	The water absorption increased steadily until 100 days then became constant and hybrid composites absorb more water than the single composites.	[158]
Nano-SiO <sub>2</sub> (0, 2, and 5 wt%)	Baggage-high density polyethylene (HDPE)	Water absorption, Thickness swelling	The percentage of water absorption depended upon the wt% of SiO <sub>2</sub> nanoparticle. The maximum absorption of water was found at 5 wt% of nano infusion. The highest percentage of thickness swelling was at 2 wt% of nano-SiO <sub>2</sub> after 2h.	[113]
Nano-ZnO (5 wt%)	Kenaf-unsaturated polyester	Water absorption, biodegradability	Water uptake was tested with 4 different layers of kenaf fiber where 2 and 3 layers of kenaf showed more water absorption compared to 1 and 2 layers of kenaf in 5 wt% ZnO filled nanocomposite. Because of the highest kenaf contained, 4 layers kenaf/ZnO/polyester composite gave higher degree of degradation compared to other	[114]
Silica nanoparticle (0, 1, 2, 3, and 4 wt%)	Hemp-sisal-epoxy	Theoretical density, experimental density, and void fraction	Density increased with the addition of nanoparticle and void fraction decreased with the increasing nano silica content	[125]
Bamboo nanoparticle (0-5 wt%)	Woven/nonwoven kenaf-unsaturated polyester	Theoretical density, measured density, void fraction, and water absorption	Unfilled composites had the highest void contents whereas 3 wt% of nano particle for both woven and nonwoven kenaf fiber composite provided lowest voids. The percentage of water absorption decreased with concentration of nanoparticles.	[147]
Calcium carbonate nanoparticle	Kenaf-polyester	Water resistance test	CaCO <sub>3</sub> caused increment of water absorption in the composite	[159]
Nanographene (0,1,2, and 4 phr)	Wood flour-HDPE-foaming agent	Water absorption, thickness swelling	Water absorption and thickness swelling reduced with the addition of graphene nanoparticle	[160]
Carbon nanotube (0, 1 and 2 phr)	Wood flour-PVC	Cell density, water absorption, thickness swelling	Highest cell density was found by the incorporation of 2 phr CNTs into the composite.	[161]
Nanoclay (0, 2, and 5 phr)	Wheat straw flour-foamed HDPE	Water absorption, thickness swelling	the water absorption and thickness swelling found lower	[162]
Nano-ZnO (0, 1, 2, and 4 phc)	Wood flour-polypropylene	Water absorption, thickness swelling	The moisture absorption and dimensional stability of the composites progressively decreased with an increasing nano-ZnO loading. Highest thickness swelling was found with 4 phc ZnO-nano filler	[163]

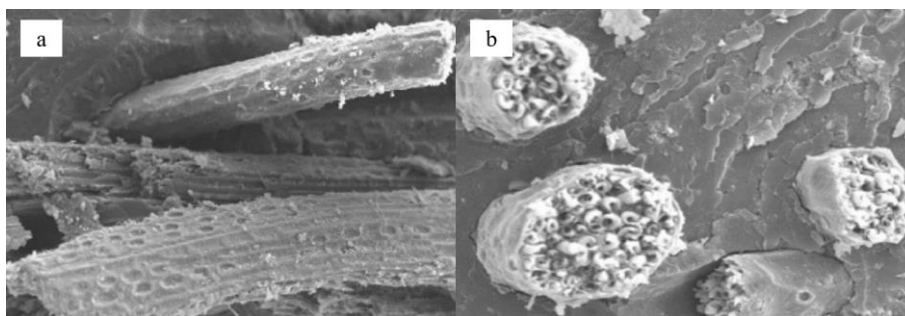


Fig 4 SEM images of the (a) 0% Nano Clay and (b) 2% Nano Clay composites [134]

Majid, et al. [2] investigated the mechanical and morphological properties of napier/epoxy composites. The SEM interrogations of the fabricated specimen reveals that the higher wt% incorporation of the filler material reduces the fiber pull out from the matrix. Delamination or low interfacial properties can be considered the key drawback of using such green composites. Delamination can be occurred due to the presence of residual stresses during the manufacture. For designing such structures, it's inevitable to gather the concept of interlaminar fracture properties. Influence of fiber architectures on the mode-I and mode-II interlaminar fracture toughness of flax fiber epoxy

composites were investigated [166]. The mode-I interlaminar fracture toughness (G<sub>Ic</sub>) of flax, glass and hybrid flax-glass fibre woven composites were studied using a DCB test and observed by SEM images [167]. The effect of water absorption on the interlaminar fracture toughness behavior of woven flax and flax/basalt reinforced vinyl ester composite laminates were examined and it was found that hybridization of basalt fiber improved the interlaminar fracture toughness [168]. Results of adding TiO<sub>2</sub> on flax fiber reinforced epoxy composites depicts the significant improvement in the Mode I and Mode II interlaminar fracture toughness [169]. It was found that nano

TiO<sub>2</sub> at 0.4 wt% addition improved the GIc value by 52% and 0.5 wt% addition resulted in 73% improvement in the GIc value. Mode I and Mode II interlaminar fracture toughness for 0.4 wt% and 0.5 wt% addition of TiO<sub>2</sub> correspondingly is depicted in Fig 5. SEM images of the composites (fiber failure at various tests) depicts that the addition of various nano particle at certain percentages enhance the mechanical properties though at higher percentages the properties deteriorate due to the agglomeration of the nano fillers. Moreover, it can be said that the void between the matrix and fiber significantly reduced by incorporating nano filler. Therefore, it is highly recommended to add nano fillers with calculated proportion in the fabrication of composites for getting the optimum characteristics.

**8 Applications**

Bio-based composites provide a versatile area for potential use in various sectors such as in automobiles, home appliances, medicine, weapons, civic infrastructure, the navy, sports, packaging, electronics, etc. [149], [170]. Ford was the first automaker to use plant fibers in composites in 1930 for body panels [171]. Following that, Mercedes-Benz constructed the door structure of jute/epoxy in the 1990. It was reported that the annual use of natural fiber composites by the German car industry is 19 kt, of which 64% are flax, 11% are jute/kenaf, 10% are hemp, and 7% are sisal [172].

For increasing the mechanical and physical properties of polymer composites, nanoparticles are currently considered to be a viable filler material. Bio composites with nanoparticles are employed to obtain fine properties of organic coatings. As a result, these nanocomposites have been thoroughly researched to produce organic anticorrosion coatings that are also advantageous to the environment. The functionalization of natural fiber-based composites with different nanoparticles has a good prospect such as waterproofing, flexible processability, fire resistance, high magnetic properties antibacterial qualities, UV protection, insulation, self-cleaning capabilities, etc. The fact that they are made of bio-based ingredients and naturally decompose makes them significant environmentally safe and harmless materials. Recently, in the biomedical field, nanocellulose is increasingly gaining popularity for its use in tissue engineering, bone regeneration, drug delivery systems, skin replacement after burns, and wound dressings [173]. A CS-based composite containing selenium nanoparticles was developed by Kalishwaralal et al [174] for tissue engineering applications. By employing nanocellulose, food storage, transportation, and shelf life are all improved. White cheese was kept in storage for 30 days at 7° C. After 15 days of storage, the composite with 2%, 4%, and 8% filler added lowers coliforms when compared to the control film [175].

A summary of the applications of different natural fiber based nano composites are listed in Table 5.

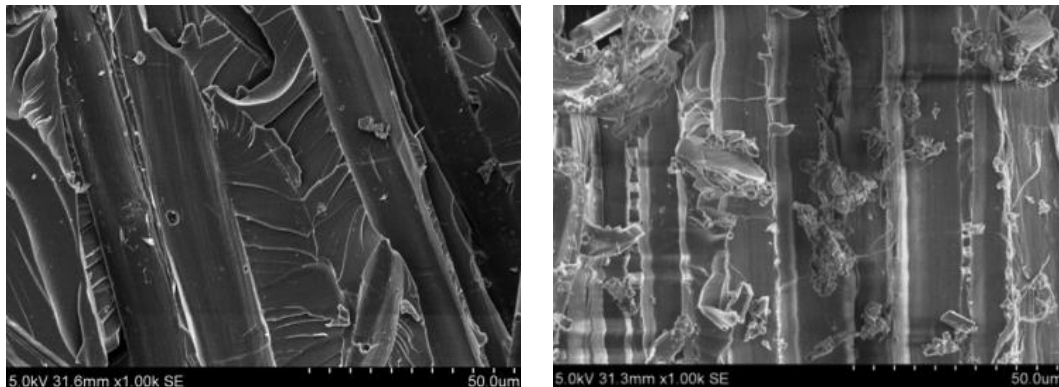


Fig 5 SEM images of (left) Mode I test specimens fractured surface for 0.4 wt.% (right) Mode II test specimens fractured surface for 0.5 wt.% added of TiO<sub>2</sub> in flax fiber reinforced epoxy composites [169]

Table 5 Application of natural fiber based nano composites in different sectors

Sectors	Fiber used	Nano particle used	Application Sectors
Automobile and Aerospace	abaca, pineapple leaf, coir, oil palm, bagasse, bamboo, wheat straw, curaua, and rice husk	Graphene, nano clay,	seats, body panels, carpets, glove box, seat backrest panel, trunk panel, sun visor, roof cover, car dashboard
Food Packaging	Hemp, Ramie, Jute, kenaf, Chitosan	TiO <sub>2</sub> , ZnO NPs, nano clay, Graphene	Packaging of Fruits,
Construction	Hemp, Oil palm, Jute, wood, coir, sisal	Graphene, nano clay	Roofs, windows, panels, Railing
Electrical and Electronics	Hemp, Rice Husk	Nanocellulose, Cu NP, MgO NP	Mobile cases, laptops cases,
Tissue Engineering	Chitosan, Silk, Feather	SeNPs, crystal nanocellulose	cardiac patches
Cosmetic industry	cotton	Nano clay	Cosmetic skin mask
Medical sectors	Wood, Bagasse, CNT	Graphene, nano clay, Cu NP, Se NP, SiO <sub>2</sub> NP	dental brackets, bone and tissues repair and reconstruction, and implant,
Sports Equipment	Flax	Graphene,	Paddle, golf, hockey stick, skeleton of tennis rackets, helmets, bicycle, Frames, Snowboards
Others	Coir, Ramie, Wood, Flax, Kenaf,	CuO,	helmets and post-boxes, mirror casing, paperweights, industrial sewing threads, fishing nets, canvas, Bricks, pipes, UV shielding equipment

## 9 Conclusion

Natural fiber could be the best alternative to synthetic fiber for manufacturing industrial goods considering the global environmental challenges [176]. Composites with fiber or particle reinforcements have achieved some incredible achievements in recent years. The research area on nanocomposites has been identified as being dynamic and competitive. Focusing on the fabrication processes of nanocomposites, this review article has examined the mechanical, thermal, and physical properties as well as applications.

Although natural fiber-reinforced composites are made for distinct applications with different materials, their characteristics depend on the matrix characteristic, and nature and compositions of the nanomaterials and fibers used. Therefore, a crucial stage in the creation of high-quality nanocomposite materials is the selection of an appropriate nanofiller, fiber, and matrix. Moreover, as the manufacturing process also has a great impact on productivity, composite quality, and the process's overall success, it is one of the most essential factors to consider and should be further researched. Additional research is needed to identify the various techniques of nano-reinforcement leading to large changes in material properties and their potential future. Most importantly, the harm of plastic use and other non-environment friendly materials and the benefits of natural fiber-based nanocomposites should be made more widely known. Furthermore, emphasis can be provided on the synthesis of nanocellulose and use as a nanofiller in the bio composites as reinforcement. Eventually, it can be said that there is plenty of scope of study to reveal the benefit of using nano filler in composite processing by modifying the technique, surface treatment and the quality of the raw materials.

## References

- [1] Gowthaman, N. S. K., Lim, H. N., Sreeraj, T. R., Amalraj, A., & Gopi, S. (2021). Advantages of biopolymers over synthetic polymers: Social, economic, and environmental aspects. In *Biopolymers and Their Industrial Applications* (pp. 351-372). Elsevier.
- [2] Mahir, F. I., Keya, K. N., Sarker, B., Nahian, K. M., & Khan, R. A. (2019). A brief review on natural fiber used as a replacement of synthetic fiber in polymer composites. *Materials Engineering Research*, 1(2), 88–99.
- [3] Li, M., Pu, Y., Thomas, V. M., Yoo, C. G., Ozcan, S., Deng, Y., Nelson, K., & Ragauskas, A. J. (2020). Recent advancements of plant-based natural fiber-reinforced composites and their applications. *Composites Part B: Engineering*, 200.
- [4] Zhou, Y., Fan, M., & Chen, L. (2016). Interface and bonding mechanisms of plant fibre composites: An overview. *Composites Part B: Engineering*, 101, 31-45.
- [5] Joshi, S. V. (2004). Are natural fiber composites environmentally superior to glass fiber reinforced composites? *Composites Part A: Applied Science and Manufacturing*, 35(3), 371–376.
- [6] Sgriccia, N., Hawley, M. C., & Misra, M. (2008). Characterization of natural fiber surfaces and natural fiber composites. *Composites Part A: Applied Science and Manufacturing*, 39(10), 1632–1637.
- [7] Arrakhiz, F. Z., Malha, M., Bouhfid, R., Benmoussa, K., & Quaiss, A. (2013). Tensile, flexural and torsional properties of chemically treated alfa, coir and bagasse reinforced polypropylene. *Composites Part B: Engineering*, 47, 35–41.
- [8] Hoyos, C. G., Alvarez, V. A., Rojo, P. G., & Vázquez, A. (2012). Figue fibers: Enhancement of the tensile strength of alkali treated fibers during tensile load application. *Fibers and Polymers*, 13(5), 632–640.
- [9] Atmakuri, A., Palevicius, A., Vilkauskas, A., & Janusas, G. (2020). Review of hybrid fiber based composites with nano particles—material properties and applications. *Polymers*, 12(9), 2088.
- [10] Schiffman, J. D., & Schauer, C. L. (2008). A review: Electrospinning of biopolymer nanofibers and their applications. *Polymer Reviews*, 48(2), 317–352.
- [11] Pickering, K. (2008). Properties and performance of natural-fibre composites. Elsevier.
- [12] Behnam Hosseini, S. (2020). Natural fiber polymer nanocomposites. *Fiber-Reinforced Nanocomposites: Fundamentals and Applications*, 279–299.
- [13] Choi, H. Y., Wu, H. Y. T., & Chang, fu K. (1991). A New Approach toward Understanding Damage Mechanisms and Mechanics of Laminated Composites Due to Low-Velocity Impact: Part II—Analysis. *Journal of Composite Materials*, 25(8), 1012–1038.
- [14] Roy, M. (2013b). Surface engineering for enhanced performance against wear. Springer.
- [15] Jawaid, M., Chee, S. S., Asim, M., Saba, N., & Kalia, S. (2022). Sustainable kenaf/bamboo fibers/clay hybrid nanocomposites: Properties, environmental aspects and applications. *Journal of Cleaner Production*, 330, 129938.
- [16] Gholampour, A., & Ozbakkaloglu, T. (2020). A review of natural fiber composites: Properties, modification and processing techniques, characterization, applications. *Journal of Materials Science*, 55(3), 829–892.
- [17] Amjad, A., Awais, H., Anjang Ab Rahman, A., & Abidin, M. S. Z. (2022b). Effect of nanofillers on mechanical and water absorption properties of alkaline treated flax/PLA fibre reinforced epoxy hybrid nanocomposites. *Advanced Composite Materials*, 31(4), 351–369.
- [18] Yang, J., Guo, Y., Yao, L., Ni, Q., & Qiu, Y. (2018). Effects of Kevlar volume fraction and fabric structures on the mechanical properties of 3D orthogonal woven ramie/Kevlar reinforced poly (lactic acid) composites. *Journal of Industrial Textiles*, 47(8), 2074–2091.
- [19] Amjad, A., Awais, H., Anjang Ab Rahman, A. and Abidin, M.S.Z., (2022b). Effect of nanofillers on mechanical and water absorption properties of alkaline treated flax/PLA fibre reinforced epoxy hybrid nanocomposites. *Advanced composite materials*, 31(4), pp.351-369.
- [20] Ramu, P., Jaya Kumar, C. V., & Palanikumar, K. (2019). Mechanical characteristics and terminological behavior study on natural fiber nano reinforced polymer composite - A review. *Materials Today: Proceedings*, 16, 1287–1296.
- [21] Godara, M. S. S. (2019). Effect of chemical modification of fiber surface on natural fiber composites: A review. *Materials Today: Proceedings*, 18, 3428–3434.
- [22] Bledzki, A. K., Mamun, A. A., Lucka-Gabor, M., & Gutowski, V. S. (2008). The effects of acetylation on properties of flax fibre and its polypropylene composites. *Express Polymer Letters*, 2(6), 413–422.
- [23] Ferreira, D. P., Cruz, J., & Figueiro, R. (2018). Surface modification of natural fibers in polymer composites. In *Green Composites for Automotive Applications*. Elsevier Ltd.
- [24] Vinayagamoorthy, R. (2019). Influence of fiber surface modifications on the mechanical behavior of Vetiveria zizanioides reinforced polymer composites. *Journal of Natural Fibers*, 16(2), 163–174.
- [25] Khan, J., & Mariatti, M. (2021). The Influence of Substrate Functionalization for Enhancing the Interfacial Bonding between Graphene Oxide and Nonwoven Polyester. *Fibers and Polymers*, 22(11), 3192–3202.
- [26] Silva, R., Haraguchi, S.K., Muniz, E.C. and Rubira, A.F., 2009. Applications of lignocellulosic fibers in polymer chemistry and in composites. *Química nova*, 32, pp.661-671.
- [27] Correia, C. A., & Valera, T. S. (2019). Cellulose Nanocrystals and Jute Fiber-reinforced Natural Rubber Composites: Cure characteristics and mechanical properties. *Materials Research*, 22, 1–9.
- [28] Amjad, A., Abidin, M. S. Z., Alshahrani, H., & Ab Rahman, A. A. (2021b). Effect of fibre surface treatment and nanofiller addition on the mechanical properties of flax/PLA fibre reinforced epoxy hybrid nanocomposite. *Polymers*, 13(21), 3842.
- [29] Ashok, K. G., & Kalaiichelvan, K. (2020). Mechanical, ballistic impact, and water absorption behavior of luffa/graphene reinforced epoxy composites. *Polymer Composites*, 41(11), 4716–4726.
- [30] Saba, N., Jawaid, M., Alothman, O. Y., Paridah, M. T., & Hassan, A. (2016). Recent advances in epoxy resin, natural fiber-reinforced epoxy composites and their applications. *Journal of Reinforced Plastics and Composites*, 35(6), 447–470.

- [31] Shokrieh, M. M., Kefayati, A. R., & Chitsazzadeh, M. (2012). Fabrication and mechanical properties of clay/epoxy nanocomposite and its polymer concrete. *Materials & Design*, 40, 443–452.
- [32] Calcagno, C. I. W., Mariani, C. M., Teixeira, S. R., & Mauler, R. S. (2008). The role of the MMT on the morphology and mechanical properties of the PP/PET blends. *Composites Science and Technology*, 68(10–11), 2193–2200.
- [33] Kordkheili, H. Y., Farsi, M., & Rezazadeh, Z. (2013). Physical, mechanical and morphological properties of polymer composites manufactured from carbon nanotubes and wood flour. *Composites Part B: Engineering*, 44(1), 750–755.
- [34] Amjad, A., Abidin, M. S. Z., Alshahrani, H., & Ab Rahman, A. A. (2021a). Effect of fibre surface treatment and nanofiller addition on the mechanical properties of flax/pla fibre reinforced epoxy hybrid nanocomposite. *Polymers*, 13(21).
- [35] Franco-Urquiza, E. A., & Rentería-Rodríguez, A. V. (2021). Effect of nanoparticles on the mechanical properties of kenaf fiber-reinforced bio-based epoxy resin. *Textile Research Journal*, 91(11–12), 1313–1325.
- [36] Chowdary, M. S., Raghavendra, G., Kumar, M. N., Ojha, S., & Boggarapu, V. (2022). Influence of nano-silica on enhancing the mechanical properties of sisal/kevlar fiber reinforced polyester hybrid composites. *Silicon*, 1-8.
- [37] Bazayr, B., & Samariha, A. (2017). Thermal, flammability, and morphological properties of nano-composite from fir wood flour and polypropylene. *BioResources*, 12(3), 6665–6678.
- [38] Islam, S., Atiqah, N., Hasbullah, B., Hasan, M., Abidin, Z., Jawaid, M., & Haafiz, M. K. M. (2015). Physical, mechanical and biodegradable properties of kenaf / coir hybrid fiber reinforced polymer nanocomposites. *Materials Today Communications*, 4, 69–76.
- [39] R Bhoopathi, M. R. (2020). Influence of Eggshell Nanoparticles and Effect of Alkalization on Characterization of Industrial Hemp Fibre Reinforced Epoxy Composites. *Journal of Polymers and the Environment*, 0123456789.
- [40] Lebaron, P. C., Wang, Z., & Pinnavaia, T. J. (1999). Polymer-layered silicate nanocomposites: An overview. *Applied Clay Science*, 15(1–2), 11–29.
- [41] Hasan, S. (2015). A review on nanoparticles: their synthesis and types. *Res. J. Recent Sci*, 2277, 2502.
- [42] Tamayo, L., Palza, H., Bejarano, J., & Zapata, P. A. (2018). Polymer Composites With Metal Nanoparticles: Synthesis, Properties, and Applications. Synthesis, Properties, and Applications. In *Polymer Composites with Functionalized Nanoparticles: Synthesis, Properties, and Applications* (Issue May 2019).
- [43] Haque, A., Shamsuzzoha, M., Hussain, F., & Dean, D. (2003). S2-glass/epoxy polymer nanocomposites: Manufacturing, structures, thermal and mechanical properties. *Journal of Composite Materials*, 37(20), 1821–1838.
- [44] Yong, V., & Hahn, H. T. (2004). Processing and properties of SiC/vinyl ester nanocomposites. *Nanotechnology*, 15(9), 1338–1343.
- [45] Crosby, A. J., & Lee, J. Y. (2007). Polymer nanocomposites: The “nano” effect on mechanical properties. *Polymer Reviews*, 47(2), 217–229.
- [46] Billah, S. M. R. (2019). Composites and nanocomposites. In *Functional Polymers*. Springer Nature Switzerland AG 2019.
- [47] Manjunath, M., Renukappa, N. M., & Suresha, B. (2016). Influence of micro and nanofillers on mechanical properties of pultruded unidirectional glass fiber reinforced epoxy composite systems. *Journal of Composite Materials*, 50(8), 1109–1121.
- [48] Amjad, A., Anjang Ab Rahman, A. and Abidin, M.S.Z., 2022. Effect of nanofillers on mechanical and water absorption properties of alkaline treated jute fiber reinforced epoxy bio nanocomposites. *Journal of Natural Fibers*, 19(16), pp.14592-14608.
- [49] Akpan, E. I., Shen, X., Wetzel, B., & Friedrich, K. (2019). Design and synthesis of polymer nanocomposites. In *Polymer composites with functionalized nanoparticles* (pp. 47–83). Elsevier.
- [50] Choo, K., Ching, Y. C., Chuah, C. H., Julai, S., & Liou, N. (2016). *Preparation and Characterization of Polyvinyl Alcohol-Chitosan Composite Films Reinforced with Cellulose Nanofiber*. 1–16.
- [51] Chun, S., Lee, S., Doh, G., Lee, S., & Hyeun, J. (2011). Journal of Industrial and Engineering Chemistry Preparation of Ultrastrong nanofibers using cellulose nanofibrils. *Journal of Industrial and Engineering Chemistry*, 17(3), 521–526.
- [52] Wong, J. C. H., Kaymak, H., Tingaut, P., Brunner, S., & Koebel, M. M. (2015). Mechanical and thermal properties of nanofibrillated cellulose reinforced silica aerogel composites. *Microporous and Mesoporous Materials*, 217, 150–158.
- [53] Zhang, Y., Liu, H., Li, Q., Fu, S., & others. (2016). Morphology, healing and mechanical performance of nanofibrillated cellulose reinforced poly ( $\epsilon$ -caprolactone)/epoxy composites. *Composites Science and Technology*, 125, 62–70.
- [54] Khalil, H. P. S. A., Davoudpour, Y., Islam, M. N., Mustapha, A., Sudesh, K., Dungani, R., & Jawaid, M. (2014). Production and modification of nanofibrillated cellulose using various mechanical processes: a review. *Carbohydrate Polymers*, 99, 649–665.
- [55] Nasir, M., Hashim, R., Sulaiman, O., & Asim, M. (2017). Nanocellulose: Preparation methods and applications. In *Cellulose-reinforced nanofibre composites* (pp. 261–276). Elsevier.
- [56] Mandal, A., & Chakrabarty, D. (2014). Studies on the mechanical, thermal, morphological and barrier properties of nanocomposites based on poly (vinyl alcohol) and nanocellulose from sugarcane bagasse. *Journal of Industrial and Engineering Chemistry*, 20(2), 462–473.
- [57] Rosamah, E., HPS, A. K., Yap, S. W., Saurabh, C. K., Tahir, P. M., Dungani, R., & Owolabi, A. F. (2018). The role of bamboo nanoparticles in kenaf fiber reinforced unsaturated polyester composites. *Journal of Renewable Materials*, 6(1), 75.
- [58] Mohammed, M., Rahman, R., Mohammed, A. M., Osman, A. F., Adam, T., Dahham, O. S., Hashim, U., Noriman, N. Z., & Betar, B. O. (2018). Fabrication and characterization of zinc oxide nanoparticle-treated kenaf polymer composites for weather resistance based on a solar UV radiation. *BioResources*, 13(3), 6480–6496.
- [59] Ibrahim, I. D., Jamiru, T., Sadiku, E. R., Kupolati, W. K., & Agwuncha, S. C. (2016a). Impact of surface modification and nanoparticle on sisal fiber reinforced polypropylene nanocomposites. *Journal of Nanotechnology*, 2016.
- [60] Mohan, T. P., & Kanny, K. (2011). Water barrier properties of nanoclay filled sisal fiber reinforced epoxy composites. *Composites Part A: Applied Science and Manufacturing*, 42(4), 385–393.
- [61] Vieira, L. M. G., Santos, J. C. dos, Panzera, T. H., Christoforo, A. L., Mano, V., Campos Rubio, J. C., & Scarpa, F. (2018). Hybrid composites based on sisal fibers and silica nanoparticles. *Polymer Composites*, 39(1), 146–156.
- [62] Yadav, S. M., & Yusoh, K. Bin. (2016). Preparation and characterization of wood plastic composite reinforced by organoclay. *Journal of the Indian Academy of Wood Science*, 13(2), 118–131. <https://doi.org/10.1007/s13196-016-0175-5>
- [63] Rabbi, M. S., Islam, T., & Islam, G. M. S. (2021). Injection-molded natural fiber-reinforced polymer composites – a review. *International Journal of Mechanical and Materials Engineering*, 1–21.
- [64] Yee, Y. Y., Chee Ching, Y., Rozali, S., Awanis Hashim, N., & Singh, R. (2016). PLA composite with OPEFB. *BioResources*, 11(1), 2269–2286.
- [65] Rana, S. S., & Gupta, M. K. (2021). Fabrication of bionanocomposites reinforced with hemp nanocellulose and evaluation of their mechanical, thermal and dynamic mechanical properties. *Proceedings of the Institution of Mechanical Engineers, Part L: Journal of Materials: Design and Applications*, 235(11), 2470–2481.
- [66] Chen, R. S., & Ahmad, S. (2017). Mechanical performance and flame retardancy of rice husk/organoclay-reinforced blend of recycled plastics. *Materials Chemistry and Physics*, 198, 57–65.
- [67] Hemath, M., Tengsuthiwat, J., Mavinkere Rangappa, S., Siengchin, S., Khan, A., Marwani, H. M., Dzudzevic-Cancar, H., & Asiri, A. M. (2021). Effect of TiC nanoparticles on accelerated weathering of coir fiber filler and basalt fabric reinforced bio/synthetic epoxy hybrid composites: Physicomechanical and thermal characteristics. *Polymer Composites*, 42(9), 4897–4910.
- [68] Patnaik, A., Satapathy, A., & Biswas, S. (2010). Investigations on three-body abrasive wear and mechanical properties of particulate filled glass epoxy composites. *Malaysian Polymer Journal*, 5(2), 37–48.
- [69] Salit, M. S., Jawaid, M., Yusoff, N. Bin, & Hoque, M. E. (2015). Manufacturing of natural fibre reinforced polymer composites. In *Manufacturing of Natural Fibre Reinforced Polymer Composites*.
- [70] Das, S., Das, B., & Imam, R. R. (2021). Characterization of Polymer Composite Reinforced With COCONUT COIR TREATED BY KOH. *International Conference on Mechanical Engineering and Renewable Energy*.

- [71] Nagavally, R. R. (2016). Composite Materials - History, Types, Fabrication Techniques, Advantages, and Applications. *International Journal of Mechanical And Production Engineering*, 2, 25–30.
- [72] Ho, M. P., Wang, H., Lee, J. H., Ho, C. K., Lau, K. T., Leng, J., & Hui, D. (2012). Critical factors on manufacturing processes of natural fibre composites. *Composites Part B: Engineering*, 43(8), 3549–3562.
- [73] Jaafar, J., Siregar, J. P., Tezara, C., Hamdan, M. H. M., & Rihayat, T. (2019). A review of important considerations in the compression molding process of short natural fiber composites. *The International Journal of Advanced Manufacturing Technology*, 105(7), 3437–3450.
- [74] Idicula, M., Boudenne, A., Umadevi, L., Ibos, L., Candau, Y., & Thomas, S. (2006). Thermophysical properties of natural fibre reinforced polyester composites. *Composites Science and Technology*, 66(15), 2719–2725.
- [75] Kumar, R., & Shelare, S. (2019). Different method of Fabrication of composite material-A review. *Journal of Emerging Technologies and Innovative Research*, 6(3), 530–538.
- [76] Xie, Y., Hill, C. A. S., Xiao, Z., Militz, H., & Mai, C. (2010). Silane coupling agents used for natural fiber/polymer composites: A review. *Composites Part A: Applied Science and Manufacturing*, 41(7), 806–819.
- [77] Pickering, K. L., Efendy, M. G. A., & Le, T. M. (2016). A review of recent developments in natural fibre composites and their mechanical performance. *Composites Part A: Applied Science and Manufacturing*, 83, 98–112.
- [78] Wen, L. E. I., LEI, W., & Chao, R. E. N. (2006). Effect of volume fraction of ramie cloth on physical and mechanical properties of ramie cloth/UP resin composite. *Transactions of Nonferrous Metals Society of China*, 16, s474–s477.
- [79] Kalia, S., Dufresne, A., Cherian, B. M., Kaith, B. S., Av, L., Njuguna, J., & Nassiopoulos, E. (2011). Cellulose-Based Bio- and Nanocomposites : A Review. *International Journal of Polymer Science*, 2011, 1–35.
- [80] Fang, X., Bi, C., Hong, Y., Cho, K. H., Park, M. S., Wang, Y., & Yao, D. (2016). Rapid vacuum infusion and curing of epoxy composites with a rubber-cushioned mold design. *Polymer-Plastics Technology and Engineering*, 55(10), 1030–1038.
- [81] Lotfi, A., Li, H., Dao, D. V., & Prusty, G. (2021a). Natural fiber-reinforced composites: A review on material, manufacturing, and machinability. *Journal of Thermoplastic Composite Materials*, 34(2), 238–284.
- [82] Agwa, M.A., Youssef, S.M., Ali-Eldin, S.S. and Megahed, M., (2020). Integrated vacuum assisted resin infusion and resin transfer molding technique for manufacturing of nano-filled glass fiber reinforced epoxy composite. *Journal of Industrial Textiles*, 51(3\_suppl), pp.5113S-5144S.
- [83] Xiang, H., Ling, H., Wang, J., Song, L., & Gu, Y. (2005). A novel high performance RTM resin based on benzoxazine. *Polymer Composites*, 26(5), 563–571.
- [84] Li, J., Zhang, C., Liang, R., & Wang, B. (2005). Statistical characterization and robust design of RTM processes. *Composites Part A: Applied Science and Manufacturing*, 36(5), 564–580.
- [85] Lee, C.-L., & Wei, K.-H. (2000). Effect of material and process variables on the performance of resin-transfer-molded epoxy fabric composites. *Journal of Applied Polymer Science*, 77(10), 2149–2155.
- [86] Njuguna, J., Wambua, P., Pielichowski, K., & Kayvantash, K. (2011). Natural fibre-reinforced polymer composites and nanocomposites for automotive applications. In *Cellulose fibers: bio-and nano-polymer composites* (pp. 661–700). Springer.
- [87] Francucci, G., Rodríguez, E.S. and Vázquez, A., 2012. Experimental study of the compaction response of jute fabrics in liquid composite molding processes. *Journal of Composite Materials*, 46(2), pp.155-167.
- [88] Kang, M. K., Jung, J. J., & Lee, W. II. (2000). Analysis of resin transfer moulding process with controlled multiple gates resin injection. *Composites Part A: Applied Science and Manufacturing*, 31(5), 407–422.
- [89] Ricciardi, M. R., Antonucci, V., Durante, M., Giordano, M., Nele, L., Starace, G., & Langella, A. (2014). A new cost-saving vacuum infusion process for fiber-reinforced composites: Pulsed infusion. *Journal of Composite Materials*, 48(11), 1365–1373.
- [90] Vila, J., González, C., & LLorca, J. (2017). Fabric compaction and infiltration during vacuum-assisted resin infusion with and without distribution medium. *Journal of Composite Materials*, 51(5), 687–703.
- [91] Saputra, A. H., & Ibrahim, R. H. (2018). The effect of woven roving fiberglass total layers on resin infusion time in vacuum infusion. *IOP Conference Series: Materials Science and Engineering*, 345(1), 12032.
- [92] Francucci, G., Palmer, S., & Hall, W. (2018). External compaction pressure over vacuum-bagged composite parts: effect on the quality of flax fiber/epoxy laminates. *Journal of Composite Materials*, 52(1), 3–15.
- [93] Bender, D., Schuster, J., & Heider, D. (2006). Flow rate control during vacuum-assisted resin transfer molding (VARTM) processing. *Composites Science and Technology*, 66(13), 2265–2271.
- [94] Lee, J.-M., Kim, B.-M., & Ko, D.-C. (2019). Development of vacuum-assisted prepreg compression molding for production of automotive roof panels. *Composite Structures*, 213, 144–152.
- [95] Yenilmez, B., Senan, M., & Sozer, E. M. (2009). Variation of part thickness and compaction pressure in vacuum infusion process. *Composites Science and Technology*, 69(11–12), 1710–1719.
- [96] CRIPPS, D., SEARLE, T. J., & SUMMERSCALES, J. (2000). Open Mold Techniques for Thermoset Composites. *Comprehensive Composite Materials*, 737–761.
- [97] Joshi, S. C. (2012). The pultrusion process for polymer matrix composites. In *Manufacturing Techniques for Polymer Matrix Composites (PMCs)*. Woodhead Publishing Limited.
- [98] Sharma, D., McCarty, T. A., Roux, J. A., & Vaughan, J. G. (1998). Investigation of dynamic pressure behavior in a pultrusion die. *Journal of Composite Materials*, 32(10), 929–950.
- [99] Alshgari, R. A., Sargunan, K., Kumar, C. S. R., Vinayagam, M. V., Madhusudhanan, J., Sivakumar, S., ... & Ramasubramanian, G. (2022). Effect of Fiber Mixing and Nanoclay on the Mechanical Properties of Biodegradable Natural Fiber-Based Nanocomposites. *Journal of Nanomaterials*, 2022.
- [100] Balasubramanian, K., Sultan, M. T. H., & Rajeswari, N. (2018). Manufacturing techniques of composites for aerospace applications. *Sustainable Composites for Aerospace Applications*, 55–67.
- [101] WD Callister Jr, D. R. (2020). Callister's Materials Science and Engineering.
- [102] White, J. R. (1985). On the layer removal analysis of residual stress - Part 1 Polymer mouldings with depth-varying Young's modulus. *Journal of Materials Science*, 20(7), 2377–2387.
- [103] Zhao, N., Lian, J., Wang, P., & Xu, Z. (2022). Recent progress in minimizing the warpage and shrinkage deformations by the optimization of process parameters in plastic injection molding: A review. *The International Journal of Advanced Manufacturing Technology*, 1–17.
- [104] Kim, S.-K., Lee, S.-W., & Youn, J.-R. (2002). Measurement of residual stresses in injection molded short fiber composites considering anisotropy and modulus variation. *Korea-Australia Rheology Journal*, 14(3), 107–114.
- [105] Azeem, M., Ya, H. H., Kumar, M., Stabla Pawel and Smolnicki, M. G. L., Khan, R., Ahmed, T., Ma, Q., Sadique, M. R., & others. (2022). Application of filament winding technology in composite pressure vessels and challenges: a review. *Journal of Energy Storage*, 49, 103468.
- [106] Vargas-Rojas, E. (2022). Prescriptive comprehensive approach for the engineering of products made with composites centered on the manufacturing process and structured design methods: Review study performed on filament winding. *Composites Part B: Engineering*, 110093.
- [107] Sun, G., Wang, Z., Hong, J., Song, K., & Li, Q. (2018). Experimental investigation of the quasi-static axial crushing behavior of filament-wound CFRP and aluminum/CFRP hybrid tubes. *Composite Structures*, 194, 208–225.
- [108] Zhang, Q., Wu, J., Gao, L., Liu, T., Zhong, W., Sui, G., & Yang, X. (2016). Influence of a liquid-like MWCNT reinforcement on interfacial and mechanical properties of carbon fiber filament winding composites. *Polymer*, 90, 193–203.
- [109] Billah, M. M., Rabbi, M. S., & Hasan, A. (2021). A review on developments in manufacturing process and mechanical properties of natural fiber composites. *Journal of Engineering Advancements*, 2(01), 13-23.

- [110] Rajeshkumar, G., Seshadri, S. A., Ramakrishnan, S., Sanjay, M. R., Siengchin, S., & Nagaraja, K. C. (2021). A comprehensive review on natural fiber/nano-clay reinforced hybrid polymeric composites: Materials and technologies. *Polymer Composites*, 42(8), 3687–3701.
- [111] Guo, F., Aryana, S., Han, Y., & Jiao, Y. (2018). A review of the synthesis and applications of polymer–nanoclay composites. *Applied Sciences*, 8(9), 1696.
- [112] Kenned, J. J., Sankaranarayanan, K., & Kumar, C. S. (2021). Chemical, biological, and nanoclay treatments for natural plant fiber-reinforced polymer composites: A review. *Polymers and Polymer Composites*, 29(7), 1011–1038.
- [113] Hosseini, S. B., Hedjazi, S., Jamalirad, L., & Sukhtesaraie, A. (2014). Effect of nano-SiO<sub>2</sub> on physical and mechanical properties of fiber reinforced composites (FRCs). *Journal of the Indian Academy of Wood Science*, 11(2), 116–121.
- [114] Mohammed, M., Betar, B. O., Rahman, R., Mohammed, A. M., Osman, A. F., Jaafar, M., Adam, T., Dahham, O. S., Hashim, U., & Noriman, N. Z. (2019). Zinc oxide nano particles integrated kenaf/unsaturated polyester biocomposite. *Journal of Renewable Materials*, 7(10), 967–982.
- [115] Ramakrishnan, S., Krishnamurthy, K., Rajasekar, R., & Rajeshkumar, G. (2019). An experimental study on the effect of nano-clay addition on mechanical and water absorption behaviour of jute fibre reinforced epoxy composites. *Journal of Industrial Textiles*, 49(5), 597–620.
- [116] Nayak, S., Nayak, R. K., & Panigrahi, I. (2021). Effect of nano-fillers on low-velocity impact properties of synthetic and natural fibre reinforced polymer composites- a review. *Advances in Materials and Processing Technologies*, 00(00), 1–24.
- [117] Patel, K., Patel, J., Gohil, P., & Chaudhary, V. (2018). Effect of nano clay on mechanical behavior of bamboo fiber reinforced polyester composites. *Applied Mechanics and Materials*, 877, 294–298.
- [118] Majid, M.A., Ridzuan, M.J.M. and Lim, K.H., 2020. Effect of nanoclay filler on mechanical and morphological properties of napier/epoxy composites. In *Interfaces in Particle and Fibre Reinforced Composites* (pp. 137-162). Woodhead Publishing.
- [119] Wang, A., Xian, G., & Li, H. (2019). Effects of fiber surface grafting with nano-clay on the hydrothermal ageing behaviors of flax fiber/epoxy composite plates. *Polymers*, 11(8), 1278.
- [120] Haq, M., Burgueño, R., Mohanty, A. K., & Misra, M. (2008). Hybrid bio-based composites from blends of unsaturated polyester and soybean oil reinforced with nanoclay and natural fibers. *Composites Science and Technology*, 68(15–16), 3344–3351.
- [121] del Pino, G., Kieling, A. C., Bezazi, A., Boumediri, H., de Souza, J. F., Valenzuela D'Almeida, F., Valin Rivera, J. L., Dehaini, J., & Panzera, T. H. (2020). Hybrid polyester composites reinforced with curauá fibres and nanoclays. *Fibers and Polymers*, 21(2), 399–406.
- [122] Yang, Z., Peng, H., Wang, W., & Liu, T. (2010). Crystallization behavior of poly( $\epsilon$ -caprolactone)/layered double hydroxide nanocomposites. *Journal of Applied Polymer Science*, 116(5), 2658–2667.
- [123] Das, P. P., Chaudhary, V., Ahmad, F., & Manral, A. (2021). Effect of nanotoxicity and enhancement in performance of polymer composites using nanofillers: A state-of-the-art review. *Polymer Composites*, 42(5), 2152–2170.
- [124] Kord, B. (2012). Effect of nanoparticles loading on properties of polymeric composite based on hemp fiber/polypropylene. *Journal of Thermoplastic Composite Materials*, 25(7), 793–806.
- [125] Singh, T., Gangil, B., Ranakoti, L., & Joshi, A. (2021). Effect of silica nanoparticles on physical, mechanical, and wear properties of natural fiber reinforced polymer composites. *Polymer Composites*, 42(5), 2396–2407.
- [126] Zhou, S., Li, J., Kang, S., & Zhang, D. (2022). Effect of carbonized ramossissima nanoparticles on mechanical properties of bamboo fiber/epoxy composites. *Journal of Natural Fibers*, 19(4), 1239–1248.
- [127] Ghalehno, M. D., Kord, B., & Sheshkal, B. N. (2020). MECHANICAL AND PHYSICAL PROPERTIES OF WOOD/POLYETHYLENE COMPOSITE REINFORCED WITH TiO<sub>2</sub> NANOPARTICLES. *Cerme*, 26, 474–481
- [128] Sumesh, K. R., & Kanthavel, K. (2019). Green Synthesis of Aluminium Oxide Nanoparticles and its Applications in Mechanical and Thermal Stability of Hybrid Natural Composites. *Journal of Polymers and the Environment*, 27(10), 2189–2200.
- [129] Torres, M., Rodriguez, V. R., Alcantara, P. I., & Franco-Urquiza, E. (2022). Mechanical properties and fracture behaviour of agave fibers bio-based epoxy laminates reinforced with zinc oxide. *Journal of Industrial Textiles*, 51(4), 5847S-5868S.
- [130] Mylsamy, B., Palaniappan, S. K., Subramani, S. P., Pal, S. K., & Aruchamy, K. (2019). Impact of nanoclay on mechanical and structural properties of treated *Coccinia indica* fibre reinforced epoxy composites. *Journal of Materials Research and Technology*, 8(6), 6021–6028.
- [131] Fahrina, A., Yusuf, M., Muchtar, S., Fitriani, F., Mulyati, S., Aprilia, S., Rosnelly, C. M., Bilad, M. R., Ismail, A. F., Takagi, R., Matsuyama, H., & Arahman, N. (2021). Development of anti-microbial polyvinylidene fluoride (PVDF) membrane using bio-based ginger extract-silica nanoparticles (GE-SiNPs) for bovine serum albumin (BSA) filtration. *Journal of the Taiwan Institute of Chemical Engineers*, 125, 323–331.
- [132] Ganesan, K., Kailasanathan, C., Rajini, N., Kalirasu, S., Ismail, S. O., Siengchin, S., & Ayrilmis, N. (n.d.). Assessment on jute/coir fibers reinforced polyester hybrid composites with hybrid fillers under different environmental conditions.
- [133] Bahari-Sambran, F., Eslami-Farsani, R., & Arbab Chirani, S. (2020). The flexural and impact behavior of the laminated aluminum-epoxy/basalt fibers composites containing nanoclay: an experimental investigation. *Journal of Sandwich Structures & Materials*, 22(6), 1931–1951.
- [134] Shahroze, R. M., Ishak, M. R., Salit, M. S., Leman, Z., Asim, M., & Chandrasekar, M. (2018). Effect of organo-modified nanoclay on the mechanical properties of sugar palm fiber-reinforced polyester composites. *BioResources*, 13(4), 7430–7444.
- [135] Correia, C. A., & Valera, T. S. (2019). Cellulose nanocrystals and jute fiber-reinforced natural rubber composites: cure characteristics and mechanical properties. *Materials Research*, 22.
- [136] Govindhasamy, K., & Arulmurugan, S. (2016). Mechanical characterization of jute fibre nanocomposites. *Int J Emerg Technol Comput Sci Electron*, 21, 521–524.
- [137] Abdel-Rahman, H.A., Awad, E.H. and Fathy, R.M., 2020. Effect of modified nano zinc oxide on physico-chemical and antimicrobial properties of gamma-irradiated sawdust/epoxy composites. *Journal of Composite Materials*, 54(3), pp.331-343.
- [138] Chaharmahali, M., Hamzeh, Y., Ebrahimi, G., Ashori, A., & Ghasemi, I. (2014). Effects of nano-graphene on the physico-mechanical properties of bagasse/polypropylene composites. *Polymer Bulletin*, 71(2), 337–349.
- [139] Ashori, A. (2013). Effects of nanoparticles on the mechanical properties of rice straw/polypropylene composites. *Journal of Composite Materials*, 47(2), 149–154.
- [140] Islam, M. S., Ahmad, M. B., Hasan, M., Aziz, S. A., Jawaid, M., Haafiz, M. M., & Zakaria, S. A. (2015). Natural fiber-reinforced hybrid polymer nanocomposites: effect of fiber mixing and nanoclay on physical, mechanical, and biodegradable properties. *BioResources*, 10(1), 1394–1407.
- [141] Karthik Babu, N. B., Muthukumar, S., Ramesh, T., & Arokiasamy, S. (2021). Effect of Agro-waste Microcoir Pith and Nano-alumina Reinforcement on Thermal Degradation and Dynamic Mechanical Behavior of Polyester Composites. *Journal of Natural Fibers*, 18(4), 581–593.
- [142] Hallad, S. A., Banapurmath, N. R., Patil, V., Ajarekar, V. S., Patil, A., Godi, M. T., & Shettar, A. S. (2018). Graphene Reinforced Natural Fiber Nanocomposites for Structural Applications. *IOP Conference Series: Materials Science and Engineering*, 376(1).
- [143] Prasad, A. V. R., Rao, K. B., Rao, K. M., Ramanaiah, K., & Gudapati, S. P. K. (2015). Influence of nanoclay on the mechanical performance of wild cane grass fiber-reinforced polyester nanocomposites. *International Journal of Polymer Analysis and Characterization*, 20(6), 541–556.
- [144] Venkatram, B., Kailasanathan, C., Seenikannan, P., & Paramasamy, S. (2016). Study on the evaluation of mechanical and thermal properties of natural sisal fiber/general polymer composites reinforced with nanoclay. *International Journal of Polymer Analysis and Characterization*, 21(7), 647–656.
- [145] Deepak, K., Vattikuti, S. V. P., & Venkatesh, B. (2015). Experimental Investigation of Jute Fiber Reinforced Nano Clay Composite. *Procedia Materials Science*, 10, 238–242.
- [146] Bay, M. A., Khademieslam, H., Bazayr, B., & Najafi, A. (2021). Mechanical and Thermal Properties of Nanocomposite Films Made of

- Polyvinyl Alcohol / Nanofiber Cellulose and Nanosilicon Dioxide using Ultrasonic Method. *17*(2), 65–76.
- [147] Rosamah, E., Hossain, M. S., Abdul Khalil, H. P. S., Wan Nadirah, W. O., Dungani, R., Nur Amiranajwa, A. S., Suraya, N. L. M., Fizree, H. M., & Mohd Omar, A. K. (2017). Properties enhancement using oil palm shell nanoparticles of fibers reinforced polyester hybrid composites. *Advanced Composite Materials*, *26*(3), 259–272.
- [148] Atchudan, R., Pandurangan, A., & Joo, J. (2015). Effects of nanofillers on the thermo-mechanical properties and chemical resistivity of epoxy nanocomposites. *Journal of Nanoscience and Nanotechnology*, *15*(6), 4255–4267.
- [149] Calabi Floody, M., Theng, B. K. G., Reyes, P., & Mora, M. L. (2009). Natural nanoclays: applications and future trends – a Chilean perspective. *Clay Minerals*, *44*(2), 161–176.
- [150] Ibrahim, I. D., Jamiru, T., Sadiku, E. R., Kupolati, W. K., & Agwuncha, S. C. (2016b). Impact of Surface Modification and Nanoparticle on Sisal Fiber Reinforced Polypropylene Nanocomposites. *Journal of Nanotechnology*, *2016*, 9–11.
- [151] Hasan, M. H., Mollik, M. S., & Rashid, M. M. (2018). Effect of nanoclay on thermal behavior of jute reinforced composite. *International Journal of Advanced Manufacturing Technology*, *94*(5–8), 1863–1871.
- [152] Kord, B. (2011). Nanofiller reinforcement effects on the thermal, dynamic mechanical, and morphological behavior of HDPE/rice husk flour composites. *BioResources*, *6*(2), 1351–1358.
- [153] Sumesh, K. R., Kanthavel, K., Ajithram, A., & Nandhini, P. (2019). Bioalumina Nano Powder Extraction and its Applications for Sisal, Coir and Banana Hybrid Fiber Composites: Mechanical and Thermal Properties. *Journal of Polymers and the Environment*, *27*(9), 2068–2077.
- [154] Islam, M. S., Talib, Z. A., Hasan, M., Ramli, I., Haafiz, M. K. M., Jawaid, M., Islam, A., & Inuwa, I. M. (2017). Evaluation of mechanical, morphological, and biodegradable properties of hybrid natural fiber polymer nanocomposites. *Polymer Composites*, *38*(3), 583–587.
- [155] Alhuthali, A., Low, I. M., & Dong, C. (2012). Characterisation of the water absorption, mechanical and thermal properties of recycled cellulose fibre reinforced vinyl-ester eco-nanocomposites. *Composites Part B: Engineering*, *43*(7), 2772–2781.
- [156] Amjad, A., Abidin, M. S. Z., Alshahrani, H., & Ab Rahman, A. A. (2021). Effect of fibre surface treatment and nanofiller addition on the mechanical properties of flax/PLA fibre reinforced epoxy hybrid nanocomposite. *Polymers*, *13*(21), 3842.
- [157] Amjad, A., Anjang Ab Rahman, A., & Abidin, M. S. Z. (2022). Effect of nanofillers on mechanical and water absorption properties of alkaline treated jute fiber reinforced epoxy bio nanocomposites. *Journal of Natural Fibers*, *19*(16), 14592–14608.
- [158] Islam, Md Saiful, Hasbullah, N. A. B., Hasan, M., Talib, Z. A., Jawaid, M., & Haafiz, M. K. M. (2015). Physical, mechanical and biodegradable properties of kenaf/coir hybrid fiber reinforced polymer nanocomposites. *Materials Today Communications*, *4*, 69–76.
- [159] Xia, C., Shi, S. Q., & Cai, L. (2015). Vacuum-assisted resin infusion (VARI) and hot pressing for CaCO<sub>3</sub> nanoparticle treated kenaf fiber reinforced composites. *Composites Part B: Engineering*, *78*, 138–143.
- [160] Dahmardeh Ghalehno, M., & Kord, B. (2021). Preparation, characterization and performance evaluation of wood flour/HDPE foamed composites reinforced with graphene nanoplatelets. *Journal of Composite Materials*, *55*(4), 531–540.
- [161] Farsheh, A. T., Talaiepour, M., Hemmasi, A. H., Khademieslam, H., & Ghasemi, I. (2011). Investigation on the mechanical and morphological properties of foamed nanocomposites based on wood flour/PVC/multi-walled carbon nanotube. *BioResources*, *6*(1), 841–852.
- [162] Babaei, I., Madanipour, M., Farsi, M., & Farajpoor, A. (2014). Physical and mechanical properties of foamed HDPE/wheat straw flour/nanoclay hybrid composite. *Composites Part B: Engineering*, *56*, 163–170.
- [163] Dahmardeh Ghalehno, M., & Arabi, M. (2021). A study on the effect of nano-ZnO on hygroscopic characteristics of PP/Wood flour composites. *Plastics, Rubber and Composites*, *50*(10), 516–523.
- [164] Sumesh, K. R., & Kanthavel, K. (2020). Effect of TiO<sub>2</sub> nano-filler in mechanical and free vibration damping behavior of hybrid natural fiber composites. *Journal of the Brazilian Society of Mechanical Sciences and Engineering*, *42*(4).
- [165] Chowdary, M. S., Raghavendra, G., Kumar, M. S. R. N., Ojha, S., & Boggarapu, V. (2022). Influence of Nano-Silica on Enhancing the Mechanical Properties of Sisal/Kevlar Fiber Reinforced Polyester Hybrid Composites. *Silicon*, *14*(2), 539–546.
- [166] Bensadoun, F., Verpoest, I., & Van Vuure, A. W. (2017). Interlaminar fracture toughness of flax-epoxy composites. *Journal of Reinforced Plastics and Composites*, *36*(2), 121–136.
- [167] Saidane, E. H., Scida, D., Pac, M. J., & Ayad, R. (2019). Mode-I interlaminar fracture toughness of flax, glass and hybrid flax-glass fibre woven composites: Failure mechanism evaluation using acoustic emission analysis. *Polymer Testing*, *75*, 246–253.
- [168] Almansour, F. A., Dhakal, H. N., & Zhang, Z. Y. (2018). Investigation into Mode II interlaminar fracture toughness characteristics of flax/basalt reinforced vinyl ester hybrid composites. *Composites Science and Technology*, *154*, 117–127.
- [169] Prasad, V., Sekar, K., Varghese, S., & Joseph, M. A. (2019). Enhancing Mode I and Mode II interlaminar fracture toughness of flax fibre reinforced epoxy composites with nano TiO<sub>2</sub>. *Composites Part A: Applied Science and Manufacturing*, *124*, 105505.
- [170] Shinoj, S., Visvanathan, R., Panigrahi, S., & Kochubabu, M. (2011). Oil palm fiber (OPF) and its composites: A review. *Industrial Crops and Products*, *33*(1), 7–22.
- [171] Lotfi, A., Li, H., Dao, D. V., & Prusty, G. (2021b). Natural fiber-reinforced composites: A review on material, manufacturing, and machinability. *Journal of Thermoplastic Composite Materials*, *34*(2), 238–284.
- [172] Miao, M., & Finn, N. (2008). Conversion of natural fibres into structural composites. *Journal of Textile Engineering*, *54*(6), 165–177.
- [173] Hasan, K. M. F., Horváth, P. G., & Alpar, T. (2020). Potential natural fiber polymeric nanobiocomposites: A review. *Polymers*, *12*(5).
- [174] Kalishwaralal, K., Jeyabharathi, S., Sundar, K., Selvamani, S., Prasanna, M., & Muthukumar, A. (2018). A novel biocompatible chitosan--Selenium nanoparticles (SeNPs) film with electrical conductivity for cardiac tissue engineering application. *Materials Science and Engineering: C*, *92*, 151–160.
- [175] Youssef, A. M., El-Sayed, S. M., Salama, H. H., El-Sayed, H. S., & Dufresne, A. (2015). Evaluation of bionanocomposites as packaging material on properties of soft white cheese during storage period. *Carbohydrate Polymers*, *132*, 274–285.
- [176] Dayo, A. Q., Gao, B. chang, Wang, J., Liu, W. bin, Derradji, M., Shah, A. H., & Babar, A. A. (2017). Natural hemp fiber reinforced polybenzoxazine composites: Curing behavior, mechanical and thermal properties. *Composites Science and Technology*, *144*, 114–124.

# Optimal Tuning of a LQR Controlled Active Quarter Car System Using Global Best Inertia Weight Modified Particle Swarm Optimization Algorithm

*Oghenenyoreme Emakpo Agbroko, Erastus Olarewaju Ogunti*

Department of Electrical and Electronics Engineering, Federal University of Technology, Akure,  
Ondo State, Nigeria

Received: April 10, 2023, Revised: October 28, 2023, Accepted: October 28, 2023, Available Online: November 22, 2023

## ABSTRACT

A key factor in the design of a car is the comfort and safety of its passengers. The quarter-car suspension system is a feature of the car that ensures load-carrying capacity as well as comfort and safety. It comprises links, springs, and shock absorbers (dampers). Due to its significance, several research has been conducted, to increase its road handling and holding capability while trying to keep its cost moderate. To enhance customer comfort and load carrying, the road holding capacity of an active quarter car suspension was improved/controlled in this study, using the Global Best Inertia Weight Modified Particle Swarm Optimization Algorithm. The observation of the closed loop and open loop systems after designing and simulating on MATLAB reveals a significant improvement in the closed loop system's road holding ability compared to the open loop, in that, when the system was subjected to pothole, the deflection of sprung mass reached steady state in 37.37 seconds as opposed to 7000 seconds for the open loop.

Keywords: Quarter Car, Linear Quadratic Regulator (LQR), Road profile, Global Best Inertia Weight Modified Particle Swarm Optimization (GBbest-IWM-PSO) Algorithm



Copyright @ All authors

This work is licensed under a [Creative Commons Attribution-Non Commercial 4.0 International License](https://creativecommons.org/licenses/by-nc/4.0/).

## 1 Introduction

A mechanism that physically separates a vehicle's body from its wheels is known as a quarter car system or automobile suspension system. By eliminating body vibration, roll, and heave of the body through an appropriate road contact for the tires [1], it significantly contributes to the safety and comfort of the vehicle's occupants by operating as a low pass filter (LPF). Basically, it consists of (a) an elastic component, usually a coil spring, that transmits a force proportional to and in the opposite direction of the elongation of the suspension and supports the entire static load. (b) a damping component (typically a hydraulic shock absorber), which delivers a dissipative force opposite to the elongation speed and proportional to it; this component [2], [3] delivers a negligible force at steady-state but is essential to the dynamic behavior of the suspension; and (c) a set of mechanical components that connect the suspended (sprung) body to the un-sprung (tires and wheels) mass [4].

Linear quadratic regulator (LQR) is an optimal control technique that uses a state space representation model as its foundation. It is designed by utilizing linear optimization methods. LQR controllers are designed for multi-variable and dynamic systems that are both linear and sometimes non-linear [5]. It has applications in a variety of fields, including aerospace systems [6], high-performance motion control applications for direct current (DC) motors [7], unmanned aerodynamic vehicles (UAV) [8], control of radar antenna systems [2], and autopilots for racing yachts [9]. The state weighting matrix  $Q$  and the control weighting matrix 'R' are two factors that determine its performance. Tuning LQR to attain optimality, is laborious and time-consuming when using traditional control methods [6]. Hence, to find the best values for  $Q$  and  $R$ , researchers have used a variety of evolutionary optimization techniques, including the Bees Algorithm (BA), Genetic Algorithm (GA), and Particle

Swarm Optimization (PSO) Algorithm, among others, to identify the best weighting matrices for LQR controllers [10], [5], and [11]. PSO has surpassed other computational techniques like GA and BA [12]-[14]. This is primarily because it is easy to implement, converges quickly, is robust to control parameters, and is computationally efficient [15]. However, it has the drawback of having its particles imprisoned in a local minimum as opposed to a global minimum, making the local minimum to be the outcome. As a result, the Global Best Inertia Weight Modified PSO (Gbest-IWM-PSO) algorithm, among other variants of PSO, was implemented [16].

Gbest-IWM-PSO was utilized in this study to optimize the tuning of an LQR-controlled quarter-car system. The resultant system was then exposed to various road conditions to examine its road-holding performance for providing comfort for its occupants and the safety of cargo.

## 2 Concept and Review of Related Works

To ensure the safety of goods/loads within the car and the comfort of the human occupants, a quarter-car suspension system functions as an LPF. When a disturbance of any kind occurs, the goal is to maximize the LPF characteristics of the suspension system using an LQR and then optimize the LQR performance using Gbest-IWM-PSO. This ensures that the system recovers its stability as quickly as possible. Quarter car suspension systems are of three types: active, semi-active, and passive. The spring, damper (shock absorber), and linkages [17]-[20] make up the passive suspension. By selecting an appropriate spring stiffness and damping coefficient—a measure of the shock absorber characteristics—a suitable system response can be achieved [21]. Passive systems feature set specifications that need to be selected to provide a balance between load-carrying capacity, road handling, and ride comfort. A "soft" suspension is used to maintain contact between the vehicle body and the tires to

produce ride comfort. Road disturbances are readily absorbed by the "soft" suspension. Because of this, "soft" suspensions are used in most luxury vehicles to give a smooth ride. The road handling of a vehicle is its second performance attribute. This describes a vehicle's capacity to keep its tires in contact with the ground during turns and other dynamic maneuvers. This is possible with "stiff" suspension like those seen in sports vehicles. Finding the ideal compromise between the two vehicle performance characteristics that will best serve the intended customer, is the task of a passive suspension system designer [1]. See Fig. 1. As demonstrated in Fig. 2, active suspension is an intelligent system that incorporates sensors, actuators, microcontrollers, and other components, as opposed to passive systems. As a result, it can adjust its stiffness and damping coefficient to suit the state of the road. Additionally, it has the capacity to add or take away energy from the system. Its drawbacks include the necessity for a significant amount of external energy to create the required control force [22], high cost, complex design, and propensity for oscillation (instability).

With just a fraction of the power usage of active suspension systems, semi-active suspension systems can give the same versatility, adaptability, and improved performance while maintaining the reliability of their passive counterparts. The damping or spring coefficients of a semi-active suspension can typically be adjusted in real-time as depicted in Fig. 3. The semi-active control devices do not lose stability, unlike active suspension systems, because they cannot input mechanical energy into the control system. These devices include hydro-pneumatic, hydro-elastic, and hydra gas suspensions as well as air springs, switchable shock absorbers, dampers with controllable fluids (such as electrorheological and magnetorheological fluids), various self-leveling solutions, and dampers with controllable fluids [22].

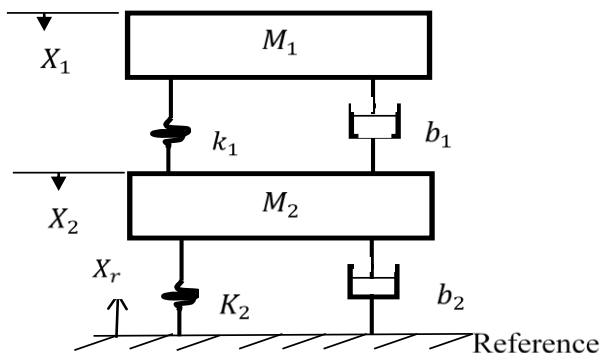


Fig. 1 Passive Suspension System

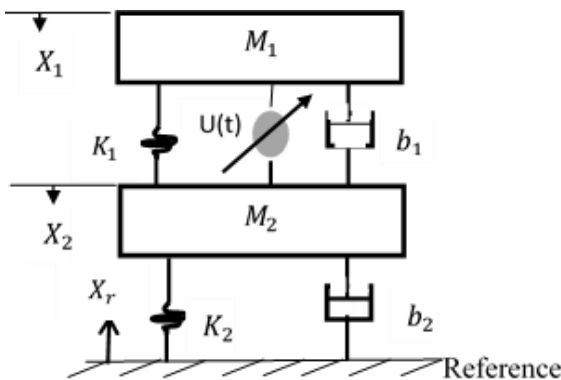


Fig. 2 Active Suspension System

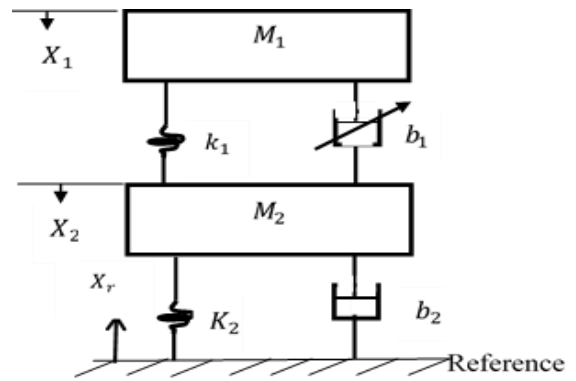


Fig. 3 Semi-Active Suspension System

Numerous control strategies have been used to enhance the damping and spring coefficient of both active and semi-active systems. These include the optimization of sliding mode control of Quarter vehicle using fuzzy logic [23], utilization of a fuzzy controller that is tuned by PSO to optimize an active suspension model [20], using fuzzy PID and LQR to optimize a Quarter car system [18], and Adaptive Fuzzy Logic control for a semi-active suspension model [24].

Eberhart and Kennedy's 1995 study yielded Particle Swarm Optimization [25]. Craig Reynolds first came up with the concept in 1987 and proposed three flocking rules to perform the mimicked bird behavior [26]. PSO computation consists of five fundamental stages. They are (i) problem definition (ii) parameter setup (iii) position and velocity initialization (iv) PSO main loop and (v) results presentation. There are four steps in PSO main loop: (a) Function evaluation (b) Personal best and global best computation (c) updating position and velocity, and (d) storing the best values (Fig. 4).

The equation for updating the velocity of Gbest-IWM-PSO, as proposed by Arumugan and Rao [16] is,

$$V_i^{t+1} = \left(1.1 - \frac{Gbest}{Pbest}\right) \times V_i^t + C_1 \times rand_1 \times (Pbest - V_i^t) + C_2 \times rand_2 \times (Gbest - V_i^t) \quad (1)$$

And Eq. (2) is for updating particle position [25],

$$X_i^{t+1} = X_i^t + V_i^{t+1} \quad (2)$$

Where  $V_i^{t+1}$  is the present particle velocity,  $X_i^{t+1}$  is the present particle position, Gbest is the global best position, Pbest is the personal best position,  $V_i^t$  is the previous particle velocity,  $X_i^t$  is the previous particle position,  $C_1$  and  $C_2$  are the personal and social acceleration coefficients,  $rand_1$  and  $rand_2$  are random variables between one and four.

### 3 Research Method

With respect to the block diagram of an active Quarter car system in Fig. 2 and applying Newton's law of motion which is,

$$F = ma \quad (3)$$

where F is force (Newton), m is mass (g) and a is acceleration (m/s<sup>2</sup>).

$$U(t) = M_1 \ddot{X}_1 + b_1(\dot{X}_1 - \dot{X}_2) + k_1(X_1 - X_2) \quad (4)$$

$$-U(t) = M_2 \ddot{X}_2 + b_2(\dot{X}_2 - \dot{X}_r) + b_1(\dot{X}_2 - \dot{X}_1) + k_2(X_2 - X_r) + k_1(X_2 - X_1) \quad (5)$$

where  $M_1$  is the sprung mass, which is a quarter of the mass of the vehicle. The mass of tire and wheel is  $M_2$ , also referred to as the un-sprung mass.  $k_1$  and  $k_2$  are the spring coefficient of the sprung and un-sprung mass respectively while  $b_1$  and  $b_2$  represent the damping coefficient of the sprung and un-sprung mass. From Eqs. (4), (5),  $\dot{X}_1 - \dot{X}_2$  represent the deflection of the sprung mass,  $\dot{X}_1$  is the speed of the car body,  $\ddot{X}_1$  represents the acceleration of the car body,  $X_2 - X_1$  is the deflection of the tire,  $\dot{X}_2$  is the tire velocity and  $U(t)$  is the actuating signal. Values of quarter car parameters are shown in Table 1.

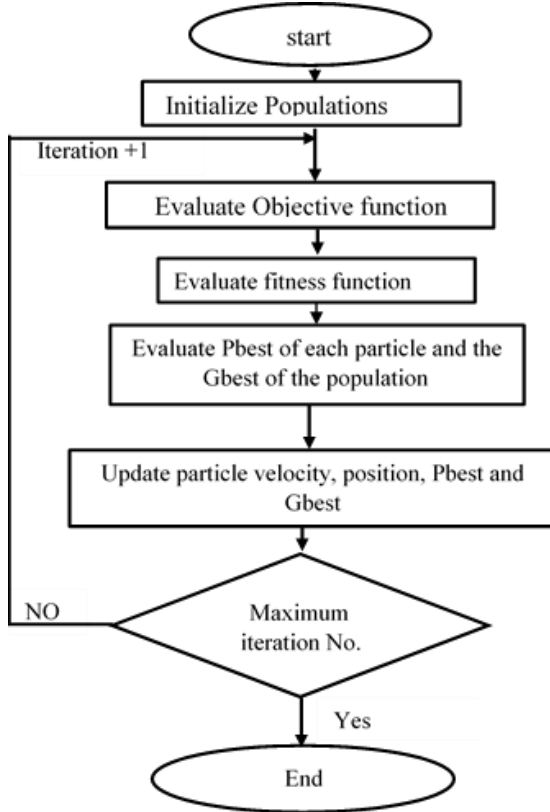


Fig. 4 Flow Chart of Basic PSO Algorithm (Adapted from [6])

Table 1 Quarter Car suspension parameters (Source: [18])

Symbol	Parameter	Value/unit
$M_1$	A quarter of Bus body Mass	300kg
$M_2$	Un-sprung Mass (Tire and Wheel)	59kg
$k_1$	Spring coefficient of the suspension system	17,000 N/m
$k_2$	Spring coefficient of wheel and tire	180,000 N/m
$b_1$	The damping coefficient of the suspension system	500 N.s/m
$b_2$	Damping coefficient of tire and wheel	1050 N.s/m

Consider an LTI (Linear Time Invariant) system whose block diagram is shown in Fig. 5,

$$\dot{x} = Ax + Bu \tag{6}$$

$$y = Cx + Du \tag{7}$$

Where  $A$  is the  $n \times n$  state matrix,  $B$  is the  $n \times r$  input matrix,  $C$  is the  $m \times n$  output matrix,  $D$  is  $m \times r$  direct transmission matrix,  $x$  is the  $n \times 1$  state vector,  $\dot{x}$  is the  $n \times 1$  derivative of the state vector,  $y$  is the  $m \times 1$  output vector and  $u$  is the  $r \times 1$  input vector.

An objective of this research is to determine an OPTIMAL value of  $K$  that will minimize the cost function ( $J$ ) of an LQR controller.

$$J = \frac{1}{2} \int_{t_0}^{t_f} (x^T Qx + u^T Ru) dt \tag{8}$$

Where  $t_f$  is the final time,  $t_0$  is the initial time,  $Q$  is the State weighting matrix which is a positive semi-definite  $n \times n$  matrix and  $R$  is the control weighting matrix which is a positive definite matrix.

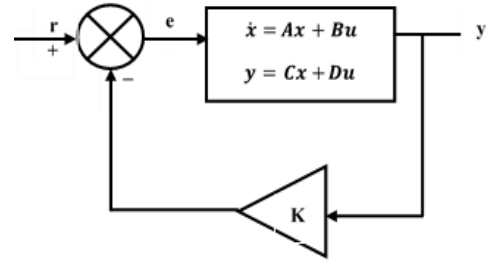


Fig. 5 Block diagram of an LTI system

At optimal state,

$$u^* = -Kx \tag{9}$$

and

$$K = R^{-1}B^T P \tag{10}$$

where  $u^*$  is the system input that minimizes the objective function,  $K$  is the optimal control feedback matrix and  $P$  is the solution of the Algebraic Riccati Equation (ARE) shown in Eq. (11).

$$PA + A^T P + Q - PBR^{-1}B^T P = 0 \tag{11}$$

The performance index that was used as the objective function of Gbest-IWM-PSO to achieve the minimization of the cost function ( $J$ ) was Integral Time Square Error (ITSE) i.e.

$$ITSE = \int t(e^2) dt \tag{12}$$

where  $e$  is the error signal (Fig. 5) which is,

$$e = r - ky \tag{13}$$

where  $r$  is the reference input and  $y$  is the system output.

Fig. 6 shows a block diagram of a full-state feedback controller with variable Gain ( $K$ ). Gbest-IWM-PSO was used to vary the value of  $K$  for each iteration (ie for each iteration, the Global best particle position is equal to  $K$ ). After the final iteration, the overall Global best particle position which is the position that best optimizes the objective function, was equated to  $K$ . Finally, with the aid of Eqs. (10), (11), the values of  $Q$  and  $R$  were determined.

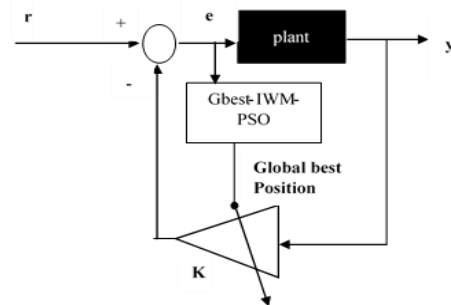


Fig. 6 Full State Feedback Controller

The Quarter car model was designed on MATLAB Simulink while the Gbest-IWM-PSO was computed using MATLAB EDITOR. With the aid of the “TO WORKSPACE” block, MATLAB “sim” command, and “logout” command, the Simulink model and EDITOR were made to interact. Twenty runs with fifty iterations per run were used to simulate the system on the MATLAB 2020b version. Table 2 shows the Gbest-IWM-PSO parameters used for the simulation.

Table 2 Gbest-IWM-PSO parameters

s/n	Item	Value	Unit
1	$C_1$	2	constant
2	$C_2$	2	constant
3	n	4	number
4	vsize	[1 n]	1xn matrix
5	pop	20	number

In Table 2 n is the number of decision variables, vsize is the matrix size of the decision variable, pop is the particle population, the lower bound (LB) of the search space is [-1000 -1000 -1000 -1000], while the upper bound is [100000 100000 100 100].

ROAD PROFILE: Three road conditions were used as a test signal for this research and they are Pot Hole Signal. This is represented with a step signal, with its step time set at 50 seconds. It will be better understood by assuming an automobile tire coming out of a pot hole Fig. 7.

Speed Breaker-The design layout as shown in Fig. 8, is a combination of the sine wave, step signal, and a product block to form a bump input as depicted in Fig. 9 [18].

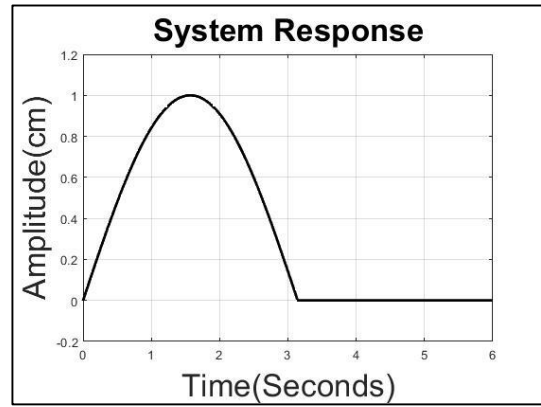


Fig. 9 Speed Breaker

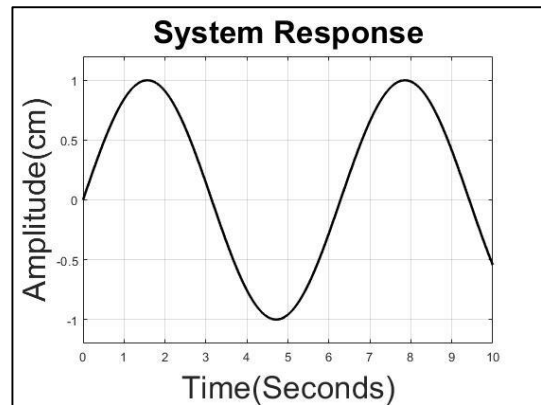


Fig. 10 Rough Road

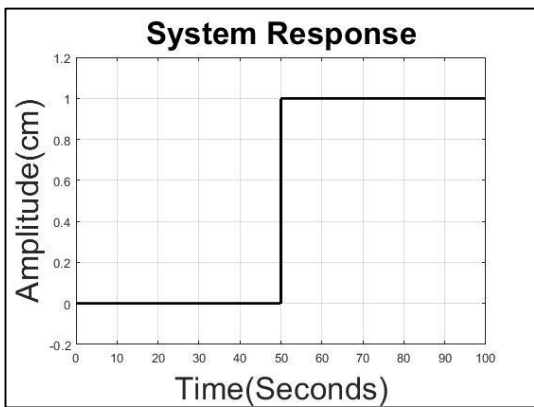


Fig. 7 Pot Hole

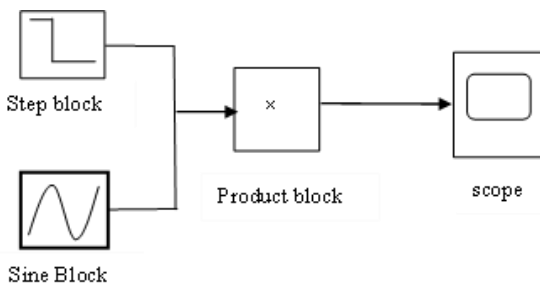


Fig. 8 Block diagram of speed breaker design

Rough Road- A sine wave signal was used to represent rough road (uneven pavement) Fig. 10. For the rough road, there was disturbance throughout the simulation time, unlike the other two road conditions where the disturbance to the system occurred at an instant of time within the simulation period.

#### 4 Results and Discussion

Results from the simulation include:

$G_{best}$  is [66361 43157 -477 -195],

$$R \text{ is } \frac{1}{122.1343} \times 10^{-6}, Q \text{ is } \begin{bmatrix} 1 & 0 & 0 & 0 \\ 0 & 22 & 0 & 0 \\ 0 & 0 & 1 & 0 \\ 0 & 0 & 0 & 7 \end{bmatrix},$$

$$P \text{ is } \begin{bmatrix} 14.2359 & 9.0649 & -39.1704 & 0.241 \\ 9.0649 & 170.4281 & -3.8804 & -8.5679 \\ -39.1704 & -3.8804 & 447.5057 & 0.0808 \\ 0.241 & -8.5679 & 0.0808 & 133.863 \end{bmatrix}$$

With respect to Abdussalam [18]:

R was 0.0001, K was  $[0.0295 \ 0.3072 \ -2.5105 \ -0.2029] \times 10^4$  and

$$Q \text{ was } \begin{bmatrix} 1000 & 0 & 0 & 0 \\ 0 & 1000 & 0 & 0 \\ 0 & 0 & 1000 & 0 \\ 0 & 0 & 0 & 1000 \end{bmatrix},$$

Furthermore, Abdussalam [18], made a graphical comparison between the speed breaker responses of a fuzzy PID-controlled system, an LQR controlled system, and a system without control (No numerical was analysis given). Careful observation of the graphs reveals that his LQR controlled system contains more oscillation during the transient period, with very much higher peak and trough overshoot. It however had a smaller settling time, peak time, and trough time when compared to the Gbest-IWM-PSO tuned LQR controlled Quarter car system in this research work.

DofSM is the deflection of sprung mass, VofSM is the velocity of sprung mass, DofUM is the deflection of un-sprung mass and VofUM is the velocity of un-sprung mass Table 3-Table 8. With regards to the open loop response to pothole and

considering the deflection of sprung mass, the system attained a maximum peak value of  $1.28113 \times 10^{-4}$ cm at a time of 13.714 secs, a maximum trough of  $1.24436 \times 10^{-6}$ cm at a time of 27.633secs, with a settling time of 7000secs, rise time of 6.835 secs and a steady state value of  $6.428 \times 10^{-4}$ cm. As regards the velocity of sprung mass, the maximum peak to trough was  $1.45569 \times 10^{-5}$  cm/s to  $-1.44231 \times 10^{-5}$ cm/s, at a time of 6.736 and 20.636 secs respectively. Steady state value of 0 with settling time of 6666.67secs. For the deflection of un-sprung mass, the maximum peak was  $1.09772 \times 10^{-5}$ cm at a time of 14.785secs, a maximum trough of  $8.67906 \times 10^{-8}$ cm at a time of 28.225secs, a rise time of 6.553secs, and a steady state value of  $5.257 \times 10^{-6}$ cm. Whereas, for the velocity of un-sprung mass, the maximum peak was  $1.11 \times 10^{-6}$ cm/s at a time of 7.977secs, the maximum trough was  $-1.368 \times 10^{-6}$ cm/s at a time of 21.368secs, settling time of 4509.3seconds with a steady state value of 0. Fig. 11 and Table 3.

As regards the open loop response to the speed breaker, considering the deflection of sprung mass, the maximum peak of the system was  $2.8643 \times 10^{-5}$ cm at a time of 8.07 secs, maximum trough of  $-2.84808 \times 10^{-5}$  at a time of 22.28secs, and settling time of 7649.15secs. While for the velocity of sprung mass, the maximum peak to trough value was  $6.1656 \times 10^{-6}$ cm/s to  $-6.50222 \times 10^{-6}$ cm/s at a time of 2.897secs and 15.253secs respectively, with a settling time of 7000secs. For the deflection of un-sprung mass, the maximum peak was  $2.60477 \times 10^{-6}$ cm, the maximum trough was  $-2.55277 \times 10^{-6}$ cm, the peak time was 7.783secs, trough time of 22.535secs and the settling time of 5000secs. While for the velocity of un-sprung mass, the maximum peak was  $7.65148 \times 10^{-7}$ cm/s, maximum trough of  $-7.71073 \times 10^{-7}$ cm/s, peak time of 3.118secs, trough time of 15.295secs and settling time of 4000secs. Table 4 and Fig. 12.

As regards the open loop response of the system to rough road and considering the deflection of sprung mass, the peak time, trough time, and settling time were 5.33secs, 20.26secs, and 5452.23secs respectively.

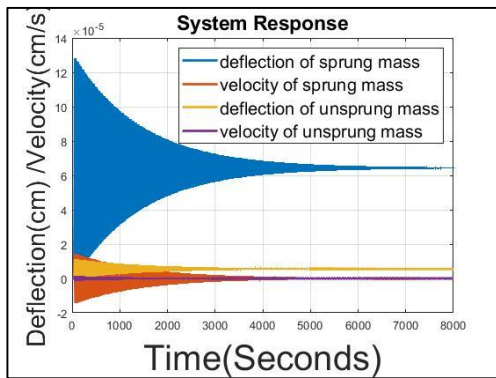


Fig. 11 Open loop pot-hole response

Table 3 Measurements from Open loop pot-hole response

Response	Peak time	Settling time	Rise time	Trough h time	Peak	Trough	Steady state value
DofSM	13.714	7000	6.835	27.633	$1.2811 \times 10^{-4}$	$1.2443 \times 10^{-6}$	$6.428 \times 10^{-4}$
VofSM	6.736	6666.67	-	20.636	$1.4556 \times 10^{-5}$	$-1.4423 \times 10^{-5}$	0
DofUM	14.785	4110.48	6.553	28.225	$1.0977 \times 10^{-5}$	$8.6790 \times 10^{-8}$	$5.257 \times 10^{-6}$
VofUM	7.977	4509.3	-	21.368	$1.11 \times 10^{-6}$	$-1.368 \times 10^{-6}$	0

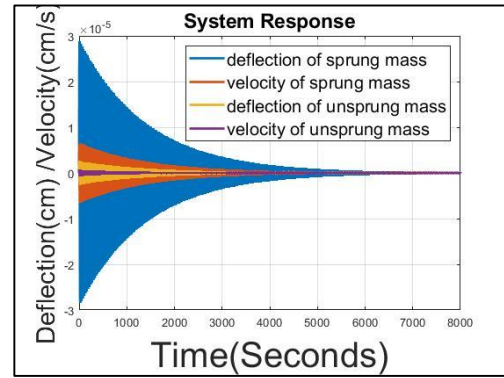


Fig. 12 Open loop speed breaker response

Table 4 Measurements from Open loop speed breaker response

Response	Peak time	Settling time	Trough time	Peak	Trough
DofSM	8.07	7649.15	22.28	$2.8643 \times 10^{-5}$	$-2.84808 \times 10^{-5}$
VofSM	2.897	7000	15.253	$6.1656 \times 10^{-6}$	$-6.50222 \times 10^{-6}$
DofUM	7.783	5000	22.535	$2.60477 \times 10^{-6}$	$-2.55277 \times 10^{-6}$
VofUM	3.118	4000	15.295	$7.65148 \times 10^{-7}$	$-7.71073 \times 10^{-7}$

During the transient period, the maximum peak was  $1.726 \times 10^{-5}$ cm while the maximum trough value was  $1.85952 \times 10^{-5}$ cm. The system finally settled with a steady peak to trough value of  $3.81717 \times 10^{-6}$ cm and  $-3.93 \times 10^{-6}$ cm. For the velocity of sprung mass, during its transient state, the maximum peak value was  $6.115 \times 10^{-6}$ cm/s at a time 2.8secs, the maximum trough was  $-6.85539 \times 10^{-6}$ cm/s at a time of 12.63secs while at steady state, the peak value was  $3.64242 \times 10^{-6}$ cm/s the trough value was  $-3.644 \times 10^{-6}$ cm/s and the settling time was 4615secs. With respect to the Deflection of un-sprung mass, the maximum peak was  $1.663 \times 10^{-6}$ cm at a time of 4.68secs, the maximum trough was  $-1.78517 \times 10^{-6}$ cm at a time of 20.23secs, attained its steady state with a peak to trough of  $4.34159 \times 10^{-7}$ cm and  $-4.344 \times 10^{-7}$ cm respectively, with a settling time of 5037.52secs. For the velocity of un-sprung mass, the maximum peak was  $7.618 \times 10^{-7}$ cm/s, the maximum trough was  $-7.96102 \times 10^{-7}$ cm/s, the peak time of 3.33secs, the trough time of 12.25secs, settling time of 4030.65secs with final peak of  $4.41081 \times 10^{-7}$ cm/s and trough value of  $-4.42 \times 10^{-7}$ cm/s. Fig. 13 and Table 5.

Concerning the closed loop response to pot-hole, considering the deflection of sprung mass, the system maximum peak was 1.19805cm at a time of 14.15secs, maximum trough value of 0.961823cm at a time of 28.46secs, the rise time of 9.14secs, the system finally settles to a steady state value of 1 at 37.38secs with a steady state error of 0. For the velocity of sprung mass, the maximum peak was 0.14246cm/s, maximum trough value was  $-0.0279637$ cm/s, peak time was 5.32secs, trough time was 19.58secs and settling time of 28.14secs. Considering the deflection of un-sprung mass, the maximum peak was 0.105052cm, maximum trough was 0.0820422cm, peak time of 13.76secs, trough time was 28.82secs, rise time of 9.06secs, and settling time of 38.28secs. While for the velocity of un-sprung mass, the maximum peak to trough value was 0.014664cm/sec to  $-0.00478997$ cm/s, there was a peak time of 6.09secs, trough time of 17.98secs and settling time of 27.06secs. Fig. 14 and Table 6.

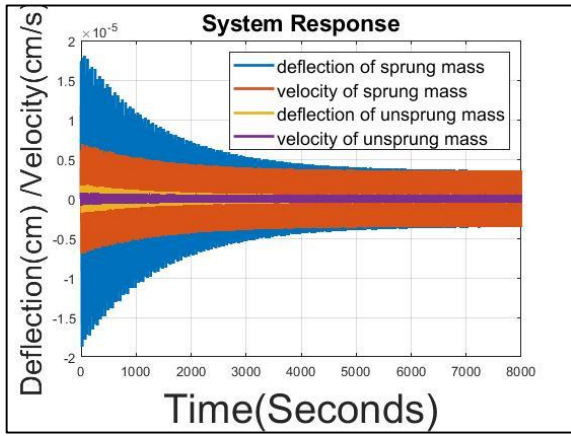


Fig. 13 Open loop rough road response

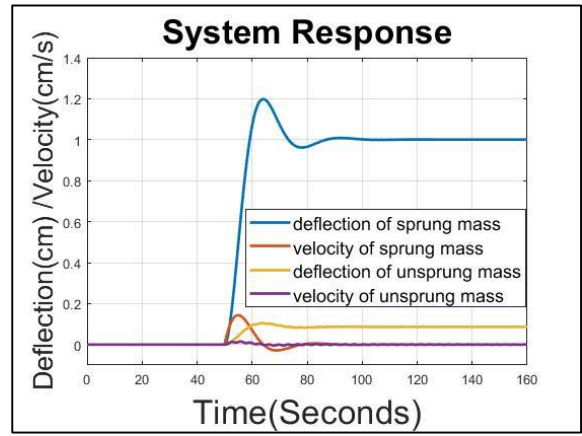


Fig. 14 Closed loop pot-hole response

Table 5 Measurements from Open loop Rough road response

Response	TRANSIENT STATE				STEADY STATE		
	Peak	Trough	Peak time	Trough time	Settling time	Peak	Trough
DofSM	$1.726 \times 10^{-5}$	$1.85952 \times 10^{-5}$	5.33	20.26	5452.23	$3.81717 \times 10^{-6}$	$-3.93 \times 10^{-6}$
VofSM	$6.115 \times 10^{-6}$	$-6.85539 \times 10^{-6}$	2.8	12.63	4615	$3.64242 \times 10^{-6}$	$-3.644 \times 10^{-6}$
DofUM	$1.663 \times 10^{-6}$	$-1.78517 \times 10^{-6}$	4.68	20.23	5037.52	$4.34159 \times 10^{-7}$	$-4.344 \times 10^{-7}$
VofUM	$7.618 \times 10^{-7}$	$-7.96102 \times 10^{-7}$	3.33	12.25	4030.65	$4.41081 \times 10^{-7}$	$-4.42 \times 10^{-7}$

Table 6 Measurements from closed loop pot-hole response

Response	Peak time	Settling time	Rise time	Trough time	Maximum peak	Maximum trough	Steady state value
DofSM	14.15	37.38	9.14	28.46	1.19805	0.961823	1
VofSM	5.32	28.14	-	19.58	0.14246	-0.0279637	0
DofUM	13.76	38.28	9.06	28.82	0.105052	0.0820422	0.0861087
VofUM	6.09	27.06	--	17.98	0.014664	-0.00478997	0

With respect to the closed loop response of the system to the speed breaker and considering the deflection of the sprung mass, the maximum peak was  $1.47711 \times 10^{-5}$ cm, the maximum trough was  $-2.90677 \times 10^{-6}$ cm, peak time was 6.4secs, trough time was 20.2secs, and a settling time of 48.5secs. As regards the velocity of sprung mass, the maximum trough was  $-2.10989 \times 10^{-6}$ cm/s, the maximum peak was  $4.51939 \times 10^{-6}$ cm/s, the peak time was 2.5secs, the trough time was 11.6secs and the settling time was 46.3secs. Considering the deflection of unsprung mass, the maximum trough was  $-3.48323 \times 10^{-7}$  cm, maximum peak  $1.38185 \times 10^{-6}$ cm, peak time of 7.4secs, trough time of 19.7secs, and settling time of 40.9secs. Furthermore, for the velocity of un-sprung mass, the maximum peak was  $3.81637 \times 10^{-7}$ cm/s, the maximum trough was  $5.98633 \times 10^{-7}$ cm/s, the peak time of 3secs, the trough time was 11.6secs and the settling time of 22.6secs. Fig. 15 and Table 7.

Finally, with respect to the closed loop system response to rough road and considering the deflection of sprung mass, the maximum peak was  $1.1434 \times 10^{-5}$ cm, at a time of 4.44secs, maximum trough was  $-4.92813 \times 10^{-6}$ cm at a time of 20.12secs. It attained a steady state at 29.56secs with a peak to trough value of  $3.4257 \times 10^{-6}$ cm to  $-3.44318 \times 10^{-6}$ cm. For the velocity of sprung mass, maximum peak was  $4.5348 \times 10^{-6}$ cm/s, maximum trough was  $-4.36965 \times 10^{-6}$ cm/s, peak time was 2.53secs, trough time was 12.24secs and it reached steady state at 18.78secs, with a peak of  $3.37789 \times 10^{-6}$ cm/s,

trough value of  $-3.38388 \times 10^{-6}$ cm/s. For the deflection of unsprung mass, the maximum peak was  $1.18334 \times 10^{-6}$ cm at a time of 4.5secs, the maximum trough was  $-5.77131 \times 10^{-7}$ cm at a time of 20.25secs and the system settling time was 29.2secs with a peak value of  $4.47008 \times 10^{-7}$ cm and trough value of  $-4.40555 \times 10^{-7}$ cm. Finally, when considering the velocity of un-sprung mass, the maximum peak was  $5.96112 \times 10^{-7}$ cm, and the maximum trough was  $-5.84252 \times 10^{-7}$ cm at a time of 2.94 and 12.33secs respectively. It settled at a time of 21.53secs with peak to trough values of  $4.96596 \times 10^{-7}$ cm and  $-4.81141 \times 10^{-7}$ cm respectively. Fig. 16 and Table 8.

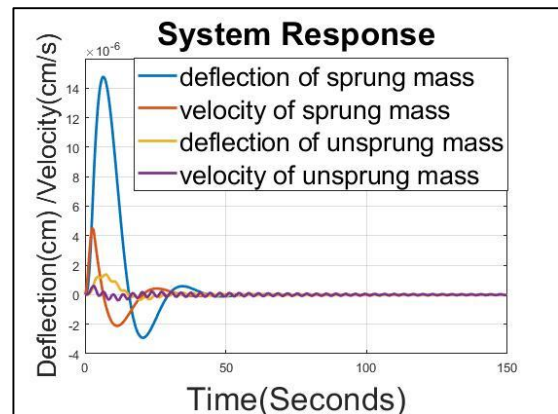


Fig. 15 Closed loop speed breaker response

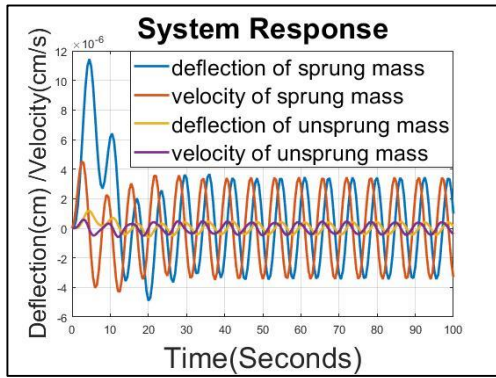


Fig. 16 Closed loop response to rough road

As shown in Fig. 17, the system poles are located at  $-0.0133 \pm j1.8286$  and  $-0.0007 \pm j0.2274$ . Careful observation reveals that the system's dominant poles are the ones located at  $-0.0007 \pm j0.2274$ . It determines the characteristics of the system; it is located very close to the origin of the s-plane hence resulting in the system oscillating for a long period. Comparing the closed loop pole location (Fig. 18) to that of the open loop shows that the dominant (significant) pole was relocated to  $-0.1157 \pm j0.2239$  whereas there was only a slight effect on the insignificant pole i.e., from  $-0.0133 \pm j1.8286$  to  $-0.014 \pm j1.8286$ . The relocation of the dominant poles far away from the origin of the s-plane resulted in a reduced oscillation time and better system stability and hence better LPF characteristics.

Table 7 Measurements from closed loop response to speed breaker

Response	Peak time	Settling time	Trough time	Peak	Trough
DofSM	6.4	48.5	20.2	$1.47711 \times 10^{-5}$	$-2.90677 \times 10^{-6}$
VofSM	2.5	46.3	11.6	$4.51939 \times 10^{-6}$	$-2.10989 \times 10^{-6}$
DofUM	7.4	40.9	19.7	$1.38185 \times 10^{-6}$	$-3.48323 \times 10^{-7}$
VofUM	3	22.9	11.6	$5.98633 \times 10^{-7}$	$-3.81637 \times 10^{-7}$

Table 8 Measurements from closed loop Rough road response

Response	Transient State				Steady state		
	Maximum peak	Maximum trough	Peak time	Trough time	Settling time	Peak	Trough
DofSM	$1.1434 \times 10^{-5}$	$-4.92813 \times 10^{-6}$	4.44	20.12	29.56	$3.4257 \times 10^{-6}$	$-3.44318 \times 10^{-6}$
VofSM	$4.5348 \times 10^{-6}$	$-4.36965 \times 10^{-6}$	2.53	12.24	18.78	$3.37789 \times 10^{-6}$	$-3.38388 \times 10^{-6}$
DofUM	$1.18334 \times 10^{-6}$	$-5.77131 \times 10^{-7}$	4.5	20.25	29.2	$4.47008 \times 10^{-7}$	$-4.40555 \times 10^{-7}$
VofUM	$5.96112 \times 10^{-7}$	$-5.84252 \times 10^{-7}$	2.94	12.33	21.53	$4.96536 \times 10^{-7}$	$-4.81141 \times 10^{-7}$

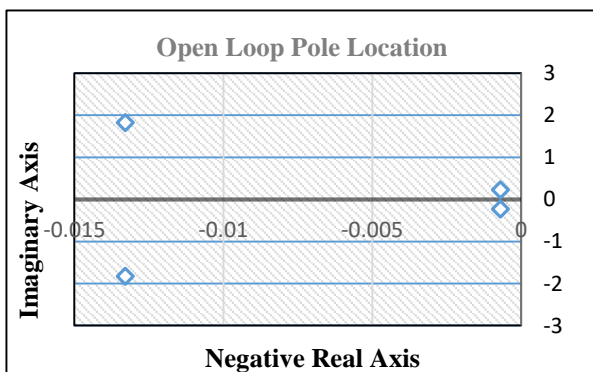


Fig. 17 Open loop pole location

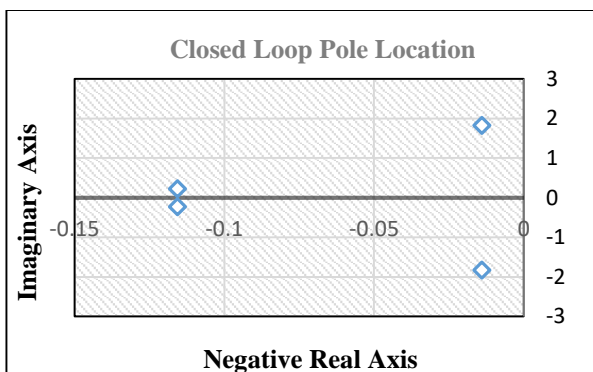


Fig. 18 Closed loop pole location

### 5 Conclusion

The goal of this research was to maximize the LPF characteristic of an active Quarter car suspension system using Gbest-IWM-PSO optimized LQR. Simulation of the system revealed a relocation of the system dominant (significant) poles from  $-0.0007 \pm j0.2274$  to  $-0.1157 \pm j0.2239$  resulting in improved transient response of the system, reduced number of oscillations, shorter settling time hence better road holding capacity for passenger comfort and better load carriage. Also noteworthy is the fact that there was a reduction in the amplitude of the maximum peak and trough when considering the system response to speed breaker and rough road. For example, the maximum peak to trough for Deflection of Sprung Mass when considering the speed breaker, for open loop was  $0.000028643$  to  $-2.84808 \times 10^{-5}$  (Fig. 12 and Table 4) while that for closed loop was  $1.47711 \times 10^{-5}$  to  $-2.90677 \times 10^{-6}$  (Fig. 15 and Table 7). Furthermore, for the pot hole and considering the deflection of sprung mass, it was observed that the steady state error dropped from  $0.9993572\text{cm}$  (i.e.  $1 - 0.0006428$ ) to  $0\text{cm}$  (Table 3 and Table 6).

### References

- [1] Kashem, S., Nagarajah, R. and Ektesabi, M., 2018. Vehicle suspension systems and electromagnetic dampers. 1st ed. Singapore: Springer Nature, ISBN 9789811054785, pp. 1-175.
- [2] Anderson, B. and Moore, J., 1989. Optimal control: linear quadratic methods, Sydney: Prentice-Hall, ISBN 0136386512, pp. 1-374.

- [3] Alias, N.A., 2013. Linear Quadratic Regulator (LQR) controller design for Inverted Pendulum (Doctoral dissertation, Universiti Tun Hussein Malaysia). pp. 1-90.
- [4] Savaresi, S.M., Poussot-Vassal, C., Spelta, C., Seneme, O. and Dugard, L., 2010. Semi-active suspension control design for vehicles. Elsevier, pp. 1-192.
- [5] Önen, Ü., Çakan, A. and İlhan, İ., 2017. Particle swarm optimization based lqr control of an inverted pendulum. *Engineering and Technology Journal*, 2(5), pp.168-174.
- [6] Al-Mahturi, A. and Wahid, H., 2017. Optimal tuning of linear quadratic regulator controller using a particle swarm optimization for a two-rotor aerodynamical system. *International Journal of Electronics and Communication Engineering*, 11(2), pp.196-202.
- [7] Ruderman, M., Krettek, J., Hoffmann, F. and Bertram, T., 2008. Optimal state space control of DC motor. *IFAC Proceedings Volumes*, 41(2), pp.5796-5801.
- [8] Szabolcsi, R., 2018. Design and development of the LQR optimal controller for the unmanned aerial vehicle. *Review of the Air Force Academy*, (1), pp.45-54.
- [9] Burns, R., 2001. *Advanced control Engineering*. Oxford: Butterworth Heinemann, Jordan Hill, ISBN 0750651008, pp. 272-299.
- [10] Hassani, K. and Lee, W.S., 2014, May. Optimal tuning of linear quadratic regulators using quantum particle swarm optimization. In *Proceedings of the International Conference on Control, Dynamic Systems, and Robotics (CDSR'14)* (Vol. 14, p. 15).
- [11] Sen, M.A. and Kalyoncu, M., 2016. Optimal tuning of a LQR controller for an inverted pendulum using the Bees algorithm. *J Autom Control Eng*, 4(5), pp. 384-387
- [12] Hao, Z.F., Guo, G.H. and Huang, H., 2007, August. A particle swarm optimization algorithm with differential evolution. In *2007 international conference on machine learning and cybernetics* (Vol. 2, pp. 1031-1035). IEEE.
- [13] Zhu, H., Wang, Y., Wang, K. and Chen, Y., 2011. Particle Swarm Optimization (PSO) for the constrained portfolio optimization problem. *Expert Systems with Applications*, 38(8), pp.10161-10169.
- [14] Fourie, P.C. and Groenwold, A.A., 2002. The particle swarm optimization algorithm in size and shape optimization. *Structural and Multidisciplinary Optimization*, 23, pp.259-267.
- [15] Ahmed, H. and Glasgow, J., 2012. *Swarm intelligence: concepts, models, and applications*. School Of Computing, Queens University Technical Report, pp. 1-38.
- [16] Arumugam, M.S. and Rao, M.V.C., 2006. On the performance of the particle swarm optimization algorithm with various inertia weight variants for computing optimal control of a class of hybrid systems. *Discrete Dynamics in Nature and Society*, 2006(79295), pp. 1-17.
- [17] Agharkakli, A., Sabet, G.S. and Barouz, A., 2012. Simulation and analysis of passive and active suspension systems using quarter car model for different road profiles. *International Journal of Engineering Trends and Technology*, 3(5), pp.636-644.
- [18] Ahmed, A.A., 2021. Quarter car model optimization of active suspension system using fuzzy PID and linear quadratic regulator controllers. *Global Journal of Engineering and Technology Advances*, 6(3), pp.088-097.
- [19] Ahmed, M.I., Hazlina, M.Y. and Rashid, M.M., 2016. Mathematical modeling and control of active suspension system for a quarter car railway vehicle. *Malaysian Journal of Mathematical Sciences*, 10(5), pp.227-241.
- [20] Al-Mutar, W.H. and Abdalla, T.Y., 2015. Quarter car active suspension system control using fuzzy controller tuned by PSO. *International journal of computer applications*, 127(2), pp.38-43.
- [21] Jiregna, I. and Sirata, G., 2020. A review of the vehicle suspension system. *Journal of Mechanical and Energy Engineering*, 4(2), pp. 109-114.
- [22] Liu, H., Gao, H. and Li, P., 2013. *Handbook of vehicle suspension control systems*. Institution of Engineering and Technology, pp. 1-397.
- [23] Gupta, A., Nitesh, K. D. & Deepak, A., 2022. Optimization in sliding mode control mechanism for reducing vibrations in the Quarter vehicle using Fuzzy Logic. *International Journal of Food and Nutritional Sciences*, Vol. 11, No. 1, pp. 3390-3401.
- [24] Yang, J., Li, J. and Du, Y., 2006. Adaptive fuzzy control of lateral semi-active suspension for high-speed railway vehicle. In *Computational Intelligence: International Conference on Intelligent Computing, ICIC 2006 Kunming, China, August 16-19, 2006 Proceedings, Part II 2* (pp. 1104-1115). Springer Berlin Heidelberg.
- [25] Eberhart, R. and Kennedy, J., 1995, October. A new optimizer using particle swarm theory. In *MHS'95. Proceedings of the sixth International Symposium on micro machine and human science* (pp. 39-43). Ieee.
- [26] Reynolds, C.W., 1987, August. Flocks, herds and schools: A distributed behavioral model. In *Proceedings of the 14th annual conference on Computer graphics and interactive techniques* (pp. 25-34)

# Development of a Weighted Productivity Model for a Food Processing Industry

B. Kareem<sup>1\*</sup>, A. S. Ilori<sup>1</sup>, and A. S. Lawal<sup>2</sup>

<sup>1</sup>Department of Industrial and Production Engineering, Federal University of Technology, Akure, Ondo state, Nigeria

<sup>2</sup>Department of Mechanical Engineering, Ekiti State University, Ado Ekiti, Nigeria

Received: June 13, 2023, Revised: November 10, 2023, Accepted: November 10, 2023, Available Online: December 12, 2023

## ABSTRACT

In this paper, the data collected from a food processing industry was used to calculate the total productivity. It presents a comprehensive model and methodology for defining and measuring productivity attributes in the food processing industry. The proposed productivity model encompasses seven key factor groups, namely labor, capital, material, energy, machines, facility maintenance, and worker stress levels. Each group is further disaggregated into individual factors, which are assigned specific weights. The mathematical expression of the productivity index model involves summing the weighted individual factors and dividing the result by the total number of group factors. In the case study conducted at a Nigerian food processing company, the developed model was applied to measure the productivity levels. The findings revealed that the current productivity of the company stands at approximately 90%. By utilizing the model, the parameters of productivity were measured, and the results were set as baseline values for future assessments. The study outcomes shed light on the perceived importance and weight values of factors within each group, highlighting their significance in influencing productivity within a technologically advanced food processing corporation. This research contributes valuable insights into the measurement and enhancement of productivity in the food processing industry, offering a structured framework for evaluating process outcomes and optimizing operations to enhance competitiveness. Incorporating the current productivity level of 90% and setting it as the baseline value provides a reference point by allowing comparisons and analysis of productivity improvements over time.

Keywords: Productivity Attributes, Food Processing Industry, Weighted Model, Competitiveness



Copyright @ All authors

This work is licensed under a [Creative Commons Attribution-Non Commercial 4.0 International License](https://creativecommons.org/licenses/by-nc/4.0/).

## 1 Introduction

Productivity is a fundamental concept used to assess resource utilization in companies. The field of productivity has been predominantly studied in economics, industrial engineering, and administration. Despite the various perspectives, productivity is commonly defined as the ratio of output to input. Enhancing productivity aims to develop a feasible model that improves efficiency and resource utilization. Achieving this requires companies to initiate improvement efforts and effectively utilize production factors to align with their goals. Measuring and analyzing the production system is essential for controlling and making informed decisions. This project focuses on developing a productivity improvement model for a food processing industry, addressing existing production process problems, and proposing solutions.

A manufacturing system involves the combination and transformation of resources, including machines, transportation elements, computers, and people, to produce goods [1]. Productivity, defined as the quantitative relationship between output and input, is crucial for organizational performance and is a major component of competitiveness [2]. Managing productivity plays a vital role in achieving organizational goals and supporting continuous improvement efforts. However, the definition of productivity is complex and varies across disciplines and perspectives. Various approaches, such as total factor productivity (TFP) and partial productivity measures, have been employed for measuring productivity [3].

There is a lack of consensus on the definition of productivity, even within the same discipline. The terms "efficiency" and "effectiveness" are frequently used but often

confused with each other [4]. Productivity is perceived differently by different individuals and institutions, ranging from efficiency and output measures to intangible factors like morale and job satisfaction [5]. Despite the disagreements, productivity remains a matter of concern for various stakeholders due to its direct relationship with the standard of living [6].

Productivity measurement aims to assess technology, efficiency, cost savings, benchmarking, and the standard of living [4]. Various definitions of productivity exist, including the technological concept (output-input ratios), the engineering concept (actual vs. potential output), and the economist concept (resource allocation efficiency) [7]. Within the overall performance criteria of a company, productivity is a key success factor [8]. Total productivity, measured as the ratio of total output to all inputs, is ideal but challenging to calculate in practice. Partial productivity measures, such as labor productivity, are commonly used as practical alternatives [9].

The Kendrick and Creamer [10] model focuses on personnel, equipment, material productivity, project scheduling, and cost control to examine and increase productivity in the construction sector. Another model developed is the Craig-Harris approach, which emphasizes customer happiness, employee involvement, service quality, process efficiency, and continuous learning and growth to increase productivity in service-oriented firms [11]. A well-known model is the Taylor-Davis approach, often known as scientific management, which seeks to boost productivity by optimizing work processes via division of labor, standardization, time and motion studies, incentives and rewards, and scientific management concepts [12]. It is important to also recognize the American Productivity

Center Model, which strives to increase productivity by building a productivity culture, using effective leadership and management techniques, encouraging employee involvement, utilizing technology and innovation, and monitoring performance [13],[14]. Lastly, the Productivity Accounting Model, according to Taylor-Davis [12], is designed to measure and evaluate productivity by measuring inputs and outputs, doing efficiency analysis, benchmarking against industry standards, and analyzing expenses to discover areas for improvement.

There is no current standard or preferred method or model for calculating productivity at the firm or process level. Modern productivity theorists and experts do not agree on how to categorize the types of models and theories or provide recommendations for their uses and applications. The user must select the type of model most appropriate to the inputs and outputs available, objectives, and which model will provide the best results [13]. For this research, a slightly more modern method, the Koss and Lewis model [15] has been selected for its flexibility in accounting for some qualitative inputs and outputs and the ability to weight factors to achieve model balance. Most productivity models measure productivity by using tangible factors. Koss and Lewis show that intangible factors can also affect productivity. Koss and Lewis proposed a productivity index as shown in Eqs. (1) and (2) of these articles. The Koss and Lewis model was re-modified by the addition of some factors found to enhance the efficient measurement and assessment of productivity in a food processing industry as shown in Eqs. (3) to (10).

The food processing business contributes significantly to the world economy, accounting for more than 10% of global GDP. However, the business confronts a variety of issues, including growing costs, increased competition, and worries about sustainability. Improving productivity is critical for the food processing industry's competitiveness and sustainability. Despite the importance of productivity, researches on productivity improvement models for the food processing industry are meager. Existing productivity models are frequently broad and do not sufficiently address the industry's unique difficulties. Existing models, for example, failed to account for the perishable nature of food goods, the complicated manufacturing processes involved and their weighted value, which are categorized as tangible and intangible factors.

This research intends to fill a gap in the literature by establishing a productivity improvement model tailored to the food processing industry. The study will integrate into the model observable (tangible) and hiding (intangible) productivity aspects such as process efficiency, staff engagement, and sustainability practice. The outcomes of the research will provide useful insights into how food processing companies might increase their productivity by considering holistically both tangible and intangible factors of production and their weights simultaneously. The proposed model is a good replacement of the existing productivity improvement models that partially measured productivity mainly based on tangible factors, especially in the food processing industries.

## 2 Methodology

### 2.1 Model Development

The complete productivity index model is expressed as follows [15]:

$$PI = \frac{f(X_1) + f(X_2) + f(X_3) + \dots + f(X_n)}{n} \quad (1)$$

Where each  $f(X_i)$  represents an individual or group productivity factor, and  $n$  is the total number of group factors.

A group productivity factor  $f(X_i)$  is broken down and expressed in the form of:

$$f(X_i) = \frac{W_a X_{ia} + W_b X_{ib} + W_c X_{ic} + \dots + W_z X_{iz}}{(W_a + W_b + W_c + W_z)z} \quad (2)$$

Each  $X_{ij}$ ,  $j = a \dots y$ ,  $X$  is then calculated as  $X_{ij}(t) / X_{ij}(t-1)$  in cases where an increase in the measure indicates a positive effect on productivity, or  $X_{ij}(t-1) / X_{ij}(t)$  where a decrease in the value signifies a positive effect on productivity.  $X_{ij}(t)$  would be the measured value of the current period, while  $X_{ij}(t-1)$  is the value of the previous period.

$W_a, W_b, W_c, \dots,$  and  $W_z$  represent the weights assigned to each productivity factor, indicating their relative importance or contribution to the overall group productivity factor.

$z$  represents the total number of weights assigned to each group productivity factor.

Based on the Koss and Lewis model, a list of quantitative and qualitative parameters that contribute to an organization's productivity and organizational smoothness of production operations was produced. Seven important productivity factor groups are developed for measuring productivity in the food processing industry: L-labor, C-capital, M-material, E-energy, Mc-machines, F-facility maintenance, and S-stress level of workers.

$$f(L) = \frac{W_1 L_1 + W_2 L_2 + W_3 L_3 + W_4 L_4 + W_5 L_5 + W_6 L_6 + W_7 L_7 + W_8 L_8 + W_9 L_9}{(W_1 + W_2 + W_3 + W_4 + W_5 + W_6 + W_7 + W_8 + W_9)^9} \quad (3)$$

Eq. (3) represents the labor group productivity factor; the equation calculates the overall productivity factors by considering the individual factors and their respective weights.

$L_1, L_2, L_3, \dots,$  and  $L_9$  represent the values or levels of the individual productivity factors, e.g., level of motivation, work hours, workforce size, skills and knowledge levels of workers, time management, teamwork, workload, health, and job satisfaction.

$$f(C) = \frac{W_1 C_1 + W_2 C_2 + W_3 C_3 + W_4 C_4 + W_5 C_5 + W_6 C_6 + W_7 C_7}{(W_1 + W_2 + W_3 + W_4 + W_5 + W_6 + W_7)^7} \quad (4)$$

Eq. (4) represents the calculation of the capital group productivity factor by considering various individual productivity factors under capital and their respective weights.

$C_1, C_2, C_3, \dots,$  and  $C_7$  represent the values or levels of the individual productivity factors, e.g., cost of equipment and machinery, cost of labor, cost of technology, cost of managing the facility, cost of supplies and raw materials, cost of transport and logistics, and cost of building and infrastructure.

$$f(M) = \frac{W_1 M_1 + W_2 M_2 + W_3 M_3 + W_4 M_4 + W_5 M_5}{(W_1 + W_2 + W_3 + W_4 + W_5)^5} \quad (5)$$

Eq. (5) represents the material group productivity factor; the equation calculates the overall productivity factors for the material group.

$M_1, M_2, M_3, \dots,$  and  $M_5$  represent the values or levels of the individual productivity factors, e.g., availability of raw materials, quality of raw materials, timely delivery of materials, ease of access to materials, and processing costs of materials.

$$f(E) = \frac{W_1 E_1 + W_2 E_2 + W_3 E_3}{(W_1 + W_2 + W_3)^3} \quad (6)$$

Eq. (6) represents the calculation of the energy group productivity factor.

E<sub>1</sub>, E<sub>2</sub>, and E<sub>3</sub> represent the values or levels of the individual productivity factors, e.g., access to reliable energy sources, quality of energy, and sustainability of energy.

$$f(M_e) = \frac{W_1 M_{e1} + W_2 M_{e2} + W_3 M_{e3} + W_4 M_{e4} + W_5 M_{e5} + W_6 M_{e6} + W_7 M_{e7}}{(W_1 + W_2 + W_3 + W_4 + W_5 + W_6 + W_7)7} \quad (7)$$

Eq. (7) represents the machine group productivity factor; the equation calculates the overall productivity factors for the machine group.

M<sub>c1</sub>, M<sub>c2</sub>, M<sub>c3</sub>..., and M<sub>c7</sub> represent the values or levels of the individual productivity factors, e.g., machine automation, speed and efficiency of machines, machine error reduction, multi-tasking, reliability of machines, flexibility of machines, and versatility of machines.

$$f(F) = \frac{W_1 F_1 + W_2 F_2 + W_3 F_3 + W_4 F_4}{(W_1 + W_2 + W_3 + W_4)4} \quad (8)$$

Eq. (8) represents the calculation of the facility maintenance group productivity factor.

F<sub>1</sub>, F<sub>2</sub>, F<sub>3</sub>, and F<sub>4</sub> represent the values or levels of the individual productivity factors, e.g., access to proper tools and equipment for carrying out maintenance, effective scheduling of time to carry out maintenance, documentation of maintenance activities, and access to standard spare parts.

$$f(S) = \frac{W_1 S_1 + W_2 S_2 + W_3 S_3}{(W_1 + W_2 + W_3)3} \quad (9)$$

Eq. (9) represents the stress level of the workers group productivity factor; the equation calculates the overall productivity factors for the stress level of the workers group.

S<sub>1</sub>, S<sub>2</sub>, and S<sub>3</sub> represent the values or levels of the individual productivity factors, e.g., job autonomy, workload, and work flexibility.

The final productivity model is identified by putting the seven group productivity elements identified in Eqs. (3) to (9) into the productivity index expression:

$$PI = \frac{f(L) + f(C) + f(M) + f(E) + f(Mc) + f(F) + f(S)}{7} \quad (10)$$

With these eight equations, productivity can be successfully measured in a food processing industry, using a re-modified Koss-Lewis-based model.

## 2.2 Model Analysis and Validation

To implement the developed model, a questionnaire was distributed to a sample of 30 personnel, including production supervisors, engineers, and line workers. The questionnaire utilized a rating scale to measure the perceived importance of each productivity factor and assign numerical values to intangible factors. The responses were collected and processed to determine the subjective weightings and numerical values for each identified factor.

The subjective weightings acquired from the questionnaire were used to compute the weighted scores for each identified productivity factor. The weights ensured that no factor had a greater impact on productivity estimation than another. The numerical values for intangible factors were obtained through personal interviews with the production manager. The data generated from the questionnaire provided weights and numerical values for the individual and group productivity components.

To determine the weights of individual productivity factors based on the respondents' ratings, each respondent rated each factor's contribution to its group productivity factor while factors were rated on a scale of 1 to 10, with 10 being the highest importance. The weight indicates the factor's contribution to the overall group's productivity. Weights of energy as a factor, for example, are being analyzed as follows using data obtained from respondents as shown in Table 1.

Table 1 Weights analysis for energy productivity factor

Respondent	Access to reliable energy source (W <sub>1</sub> )	Quality of energy (W <sub>2</sub> )	Energy sustainability (W <sub>3</sub> )
Respondent 1	8	10	6
Respondent 2	7	8	8
...	...	...	...
Respondent 30	10	10	10
Average rating	8.93	9.10	8.77

$$\text{Total average rating} = 8.93 + 9.10 + 8.77 = 26.8$$

$$W_1 = 8.93 \div 26.8 = 0.3333$$

$$W_2 = 9.10 \div 26.8 = 0.3396$$

$$W_3 = 8.77 \div 26.8 = 0.3271$$

Table 2 showcases the survey data on the level of motivation of workers. The level of motivation of workers was assessed using five survey questions (Q<sub>1</sub>-Q<sub>5</sub>) as indicated in the table. Each question was rated on a scale from 1 to 5. Respondents (1-30) were asked to rate their motivation level for each question on a scale from 1 to 5, with 1 being the lowest and 5 being the highest.

Table 2 Survey data for rating analysis of the level of motivation of workers

Respondent	Q <sub>1</sub> : Job Motivation	Q <sub>2</sub> : Accomplishment	Q <sub>3</sub> : Recognition	Q <sub>4</sub> : Growth	Q <sub>5</sub> : Enthusiasm
Respondent 1	5	5	4	4	5
Respondent 2	3	4	3	4	4
...	...	...	...	...	...
Respondent 30	4	5	4	3	5

A sample of calculation involved is as follows:

$$\text{From Table 2, respondent 1 rating} = 5 + 5 + 4 + 4 + 5 = 23$$

The individual score is multiplied by 4 to sum it to over 100.

$$\text{That is, } 23 \times 4 = 92$$

The above steps were repeated for every respondent, and the average score of the 30 respondents was considered the level of motivation of the workers.

After obtaining the values of individual factors under Energy group productivity and their respective weights, Eq. (6) was applied to obtain a baseline productivity factor value for Energy as shown:

$$f(L) = \frac{0.3333 \left(\frac{90}{90}\right) + 0.3396 \left(\frac{95}{95}\right) + 0.3271 \left(\frac{85}{85}\right)}{(0.3333 + 0.3396 + 0.3271)3} = 0.33$$

The same steps were applied to every other individual factor under every productivity group, applying their respective equations. Results are shown in Table 3-Table 16.

To calculate the overall productivity index, Eq. (10) was applied by substituting the baseline productivity factor value for the entire productivity group into the equation as shown:

$$PI = \frac{0.11 + 0.143 + 0.20 + 0.33 + 0.143 + 0.25 + 0.33}{7} = 0.215$$

**3 Results and Discussion**

Table 3-Table 9 present the individual group productivity factors considered in the evaluation of the developed model. These factors encompass: (key aspects of the workforce, including motivation, working hours, workforce size, skills and knowledge, time management, teamwork, workload volume, health, and job satisfaction for the labor group productivity factor), (key aspects of the capital resources, including equipment and machinery, labor, technology, facility maintenance, raw materials, transportation and logistics, and building and infrastructure for the capital group), (key aspects of material resources, including the availability and quality of raw materials, timely delivery, ease of access, and the processing of materials for the material group productivity factor.), (critical features of energy resources such as access to a reliable energy source, energy quality, and energy sustainability for the energy group productivity factor.), (key aspects of machine functionality, including automation, speed and efficiency, error reduction, multi-tasking capabilities, reliability, flexibility, and versatility for machine group productivity factor.), (key aspects of maintenance management, including access to tools, effective scheduling of time, documentation of maintenance activities, and access to standard spare parts for the facility maintenance group productivity factor.), (key aspects considered in controlling the stress level of workers, including job autonomy, controlled volume of workload, and work flexibility).

Table 3 Perceived importance and weight value for Labor group productivity factors

Individual factors – Labor	Average perceived importance	Weight
Level of motivation of workers	8.83	0.1100
Working hours	8.60	0.1071
Workforce size	8.57	0.1066
Skills and knowledge of workers	9.23	0.1149
Time management	9.23	0.1149
Teamwork	9.07	0.1129
Volume of workload	8.50	0.1058
Health	9.43	0.1174
Job satisfaction	8.87	0.1104

Table 4 Perceived importance and weight value for Capital group productivity factors

Individual factors – Capital	Average perceived importance	Weight
Equipment and machinery	9.23	0.1454
Labor	9.03	0.1423
Technology	8.73	0.1375
Facility maintenance	9.07	0.1428
Raw material	8.83	0.1391
Transportation and logistics	9.23	0.1454
Building and infrastructure	9.37	0.1475

Table 5 Perceived importance and weight value for Material group productivity factors

Individual factors – Material	Average perceived importance	Weight
Availability of raw material	9.20	0.2004
Quality of raw material	9.33	0.2033
Timely delivery of raw material	8.93	0.1946
Ease of access to raw material	8.90	0.1939
Processing of materials	9.53	0.2077

The average perceived importance column indicates the ratings given by the evaluators or respondents regarding the significance of each factor. These ratings reflect the subjective perception of the evaluators and were obtained through a

comprehensive assessment process involving discussions and expert opinions. The weight column represents the relative weight assigned to each factor. These weights are derived from the average perceived importance values and provide a quantitative measure of the contribution of each factor in the overall labor assessment. The weights are subjective and subject to variations based on the evaluation criteria and stakeholder opinions.

Table 6 Perceived importance and weight value for Energy group productivity factors

Individual factors – Energy	Average perceived importance	Weight
Access to reliable energy source	8.93	0.3333
Quality of energy	9.10	0.3396
Energy sustainability	8.77	0.3271

Table 7 Perceived importance and weight value for Machines group productivity factors

Individual factors – Machines	Average perceived importance	Weight
Machine automation	8.47	0.1412
Speed and efficiency of machines	9.00	0.1501
Machine error reduction	8.67	0.1445
Multi-tasking	7.90	0.1317
Reliability of machines	8.97	0.1495
Flexibility of machines	8.40	0.1401
Versatility of machines	8.57	0.1429

Table 8 Perceived importance and weight value for Maintenance group productivity factors

Individual factors – Maintenance	Average perceived importance	Weight
Access to tools	9.13	0.2532
Effective scheduling of time	8.90	0.2468
Documentation of maintenance	8.80	0.2440
Access to standard spare part	9.23	0.2560

Table 9 Perceived importance and weight value for stress level of workers group productivity factors

Individual factors – Stress level of workers	Average perceived importance	Weight
Job autonomy	8.73	0.3316
Controlled volume of workload	8.83	0.3354
Work flexibility	8.77	0.3329

Table 10 provides the computed data for each factor under the labor group. Using the expression for the labor group productivity factor (Eq. (3)), and the baseline value, a baseline labor productivity factor value of 0.11 is established. Based on this, a productivity factor value greater than 0.11, denotes an increase in labor factor productivity. On the other hand, a productivity factor value less than 0.11, indicates a declined productivity.

Table 10 Labor group productivity factor values

Individual factors – Labor	Weight	Value
Level of motivation of workers	0.1100	90
Working hours	0.1071	720
Workforce size	0.1066	150
Skills and knowledge of workers	0.1149	92
Time management	0.1149	82
Teamwork	0.1129	91
Volume of workload	0.1058	85
Health	0.1174	95
Job satisfaction	0.1104	90

Table 11 provides the data for each factor under the capital group. Inserting these values into the expression for the capital group productivity factor (Eq. (4)), a baseline capital productivity factor value of 0.143 is established. On this basis, a productivity factor value greater than 0.143 signifies an increase in capital factor productivity. Otherwise, it indicates a decline in productivity.

Table 11 Capital group productivity factor values

Individual factors – Capital	Weight	Value
Equipment and machinery	0.1454	25000
Labor	0.1423	15000
Technology	0.1375	10000
Facility maintenance	0.1428	30000
Raw material	0.1391	2400000
Transportation and logistics	0.1454	27000
Building and infrastructure	0.1475	3000000

Table 12 provides the data for each factor under the material group. Using the material group productivity equation (Eq. (5)), a baseline material productivity factor value of 0.20 is established. Future period values less than 0.20 would indicate a decrease in productivity, while values greater than 0.20 would indicate an increase in productivity.

Table 12 Material group productivity factor values

Individual factors - Material	Weight	Value
Availability of raw material	0.2004	90
Quality of raw material	0.2033	80
Timely delivery of raw material	0.1946	90
Ease of access to raw material	0.1939	88
Processing of materials	0.2077	1000

Table 13 provides the data for each factor under the energy group. Substituting these values into the expression for the energy group productivity factor (Eq. (6)), a baseline capital productivity factor value of 0.33 is established. Future period values less than 0.33 would result in a decrease in productivity, while values greater than 0.33 would bring an increase in productivity.

Table 13 Energy group productivity factor values

Individual factors – Energy	Weight	Value
Access to reliable energy source	0.3333	90
Quality of energy	0.3396	95
Energy sustainability	0.3271	85

The data for each factor under the machines group are presented in Table 14. Using the machines group productivity equation (Eq. (7)), a baseline machines productivity factor value of 0.143 is established. This outcome implies that a productivity factor value greater than 0.143 would witness an increase in machine factor productivity, otherwise, a decrease in productivity would be expected.

Table 14 Machines group productivity factor values

Individual factors – Machines	Weight	Value
Machine automation	0.1412	85
Speed and efficiency of machines	0.1501	98
Machine error reduction	0.1445	97
Multi-tasking	0.1317	1
Reliability of machines	0.1495	0.95
Flexibility of machines	0.1401	85
Versatility of machines	0.1429	30

Table 15 provides the data for each factor under the maintenance group. Substituting these values into the expression for the maintenance group productivity factor (Eq. (8)), a

baseline maintenance group productivity factor value of 0.25 is realized, which indicates a baseline value for the facility maintenance group productivity factor. Therefore, the realization of a value greater than this in the future signifies an increase in productivity while lesser value is a sign of a decrease in productivity.

Table 15 Maintenance group productivity factor values

Individual factors – Maintenance	Weight	Value
Access to tools and equipment for carrying out maintenance	0.2532	91
Effective scheduling of time to carry out maintenance	0.2468	95
Documentation of maintenance	0.2440	90
Access to standard spare parts	0.2560	98

Table 16 provides the data for each factor under the stress level of the workers group. Inserting these values into the expression for the stress level of workers group productivity factor (Eq. (9)), a baseline stress level of workers productivity factor value of 0.33 is established. Future period values less than 0.33 would indicate a decrease in productivity, while values greater than 0.33 would indicate an increase in productivity.

Table 16 Stress level of workers group productivity factor values

Individual factors – Stress level of workers	Weight	Value
Job autonomy	0.3316	20
Controlled volume of workload	0.3354	100
Work flexibility	0.3329	90

Given the baseline values known for each group productivity factor, the overall baseline productivity index was calculated as illustrated in section 2.2, and a value of 0.215 was obtained. The baseline productivity index for this analysis is 0.215. Productivity index values for future periods that exceed 0.215 suggest an overall increase in productivity, while values less than 0.215 would reveal a decrease in productivity. Comparing future values to the baseline values will indicate whether productivity has increased or decreased in each respective group.

#### 4 Conclusion

In this study, a total weighted productivity model has been developed with a special focus on the productivity attributes of the food processing industry. This model is unique because, apart from consideration of both tangible (labor, capital, material, energy, machine, maintenance, and worker’s stress level) and intangible (ease, flexibility, sustainability, accessibility, motivation, autonomy, etc.) productivity factors, these factors were weighted and integrated based on their levels of importance in establishing total productivity indices for a food processing industry. The future direction (increase or decrease) in the productivity of a company was determined based on the established baseline productivity indices. The following conclusions can be drawn from the results obtained after this model was applied to a food processing industry.

- The current productivity level of the company, 90%, is adequate as a baseline value and reference point to enable comparisons and analysis of productivity improvements over time.
- A baseline labor productivity index of 0.11 was established for the labor group productivity factors with any value higher or lesser than that being an indication of an increase or decrease in labor productivity respectively.

- Under the capital productivity group, a baseline productivity index value of 0.143 was realized in which any productivity value above or below that signified an increase or decrease in the capital productivity of the company.
- Material group productivity index of 0.20 was established as a baseline form in which its increase or decrease indicated improvement or decline of the company's productivity.
- In case of energy group productivity factors, a baseline productivity index of 0.33 was established with an indication that future increase or decrease would result in improving or declining productivity.
- Under machines group productivity index, 0.143 was realized as a baseline from which future increases or decreases in productivity could be determined with reference to this index.
- A baseline facility maintenance productivity index of 0.25 realized, has indicated a value greater or less than this in the future would result in an increase or decrease in productivity, respectively.
- In the case of the stress level of the workers group productivity index of 0.33 is an indication of the future greater or less than 0.33 would indicate an increase or decrease in the productivity of the company, respectively.
- By combining all the factors, the overall baseline productivity index of 0.215 was established which revealed that any productivity index values for future periods which exceed or below 0.215 have indicated an overall increase or decrease in productivity of the food processing company.
- Findings generally showed that the direction of overall productivity (improving or declining) of a company in the future could be determined by the level of increase (decrease) above (below) the currently established baseline overall productivity index for such a company.

## References

- [1] Gershwin, S. B., 2005. MIT. [Online] Available at: <http://web.mit.edu/manuf-sys/www/> [Accessed 8 February 2023].
- [2] Teng, H.S.S., 2014. Qualitative productivity analysis: does a non-financial measurement model exist?. *International Journal of Productivity and performance management*, 63(2), pp.250-256.
- [3] Phusavat, K. and Photaranon, W., 2006. Productivity/performance measurement: case application at the government pharmaceutical organization. *Industrial Management & Data Systems*, 106(9), pp.1272-1287.
- [4] Tangen, S., 2004. Evaluation and revision of performance measurement systems (Doctoral dissertation, Industriell produktion).
- [5] Oyeranti, A., 2006. CiteSeerx. [Online] Available at: <http://citeseerx.ist.psu.edu/viewdoc/download?doi=10.1.1.511.9388&rep=rep1&type=pdf> [Accessed 21 February 2023].
- [6] Krugman, P., 1991. Increasing returns and economic geography. *Journal of political economy*, 99(3), pp.483-499.
- [7] Wazed, M.A. and Ahmed, S., 2008. Multifactor productivity measurements model (MFPMM) as effectual performance measures in manufacturing. *Australian Journal of Basic and Applied Sciences*, 2(4), pp.987-996.
- [8] Sink, D. and Tuttle, T., 1989. Planning and measurement of productivity in your organisation of the future. Norcross, USA: Industrial Engineering and Management Press.
- [9] Hannula, M., 2002. Total productivity measurement based on partial productivity ratios. *International Journal of production economics*, 78(1), pp.57-67.
- [10] Kendrick, J. W., and Creamer, A. O., 1961. Improving productivity in construction. McGraw-Hill. London.
- [11] Craig, R. L., and Harris, H. P., 1973. Management for productivity: The Wiley series in management. John Wiley & Sons.
- [12] Taylor, F. W., and Davis, L. J., 1955. Principles of scientific management. Harper & Brothers.
- [13] Grünberg, T., 2004. Performance improvement: Towards a method for finding and prioritizing potential performance improvement areas in manufacturing operations. *International journal of productivity and performance management*, 53(1), pp.52-71.
- [14] Heap, J., 2007. Stormy productivity weather ahead?. *International Journal of Productivity and Performance Management*, 56(2), pp.170-177.
- [15] Koss, E. and Lewis, D.A., 1993. Productivity or efficiency—Measuring what we really want. *National productivity review*, 12(2), pp.273-284.

# Design and Performance Analysis of Defected Ground Slotted Patch Antenna for Sub-6 GHz 5G Applications

Md. Najmul Hossain<sup>1,\*</sup>, Al Amin Islam<sup>1</sup>, Md. Abdur Rahim<sup>2</sup>, Md. Imran Hossain<sup>3</sup>, and Md Arifour Rahman<sup>4</sup>

<sup>1</sup>Department of Electrical, Electronic and Communication Engineering, Pabna University of Science and Technology, Pabna-6600, Bangladesh

<sup>2</sup>Department of Computer Science and Engineering, Pabna University of Science and Technology, Pabna-6600, Bangladesh

<sup>3</sup>Department of Information and Communication Engineering, Pabna University of Science and Technology, Pabna-6600, Bangladesh

<sup>4</sup>Department of Electrical and Electronic Engineering, University of Rajshahi, Rajshahi-6205, Bangladesh

Received: November 04, 2023, Revised: December 25, 2023, Accepted: December 25, 2023, Available Online: December 31, 2023

## ABSTRACT

Recently, there have been notable advancements in wireless communication systems to address the deficiencies of fourth generation (4G) wireless technology, such as insufficient spectrum bandwidth, slow data transfer rates, and constrained network capacity. These issues may be addressed in fifth generation (5G) wireless technology, which is no longer stand-alone. This article proposes and designs a defected ground slotted patch antenna (DGSPA) for 5G (Sub-6 GHz band) applications. It can work at 3.5 GHz in the 5G N77 band, Sub-6 GHz 5G, LTE Band 42, and WiMAX. The suggested antenna has an overall dimension of  $38 \times 38 \times 1.575$  mm<sup>3</sup> and is built on the Rogers RT5880 substrate material, whose dielectric permittivity is 2.2. The CST software is used as the simulation tool to analyze the designed antenna's performance. The novelty of the recommended antenna is in terms of its small size with defective ground structure (DGS), high antenna gain, perfect impedance matching, and improved impedance bandwidth. The role of the DGS is evaluated by comparing the antenna's performance with and without the DGS. It has been noticed that the DGS-backed antenna had an impedance bandwidth improvement of more than 11MHz, whereas the impedance profile is  $(50.086 - j0.179) \Omega$ , which denotes  $50 \Omega$  pure resistivity. It will operate within the frequency range of (3.4828 - 3.522) GHz with an impedance bandwidth of 69.2 MHz. The proposed antenna's reflection coefficient ( $|S_{1,1}|$ ) is obtained as -54.028 dB at the resonating frequency of 3.5176 GHz, whereas the radiation gain and efficiency are observed as 6.463 dB and 93.475%, respectively. Thus, due to its promising performance based on radiation pattern, optimum efficiency, and higher bandwidth, the recommended defected ground slotted patch antenna can efficiently be used for the application of Sub-6 GHz 5G services.

Keywords: Slotted Patch Antenna, DGS, High Gain, Sub-6 GHz Band, 5G Applications



Copyright @ All authors

This work is licensed under a [Creative Commons Attribution-Non Commercial 4.0 International License](https://creativecommons.org/licenses/by-nc/4.0/).

## 1 Introduction

Wireless communication networks (WCNs) have entered a new era by introducing 5G technology. It offers several benefits over multipath environments, such as faster data rates, massive connection, low latency, wide coverage area, and many more. 5G technology is now essential in many sectors of human life, including communication, commerce, education, and transportation [1], [2]. Due to smart devices being defined as mobile users on the Internet of Things (IoT), 4G technology is insufficient to meet the increasing demand for data. In users' eyes, the key difference between 4G and 5G technology is enhanced data rate and lower power consumption with huge coverage. Cellular communication is now commonly employed in the Sub-6 GHz band, mostly at frequencies below 3 GHz. The frequency spectrum of 5G networks is divided into two ranges: Sub-6 GHz band and above-6 GHz band [3], [4].

Compared to today's 4G LTE networks, 5G uses several significant new technology advancements to significantly increase the spectrum used for data transmission and reception. For consumers, these technologies enable substantially higher speeds and more capacity [5], [6]. Following are the few technologies that are compatible with the 5G connectivity:

**Sub-6 GHz:** Most forthcoming 5G networks are expected to function predominantly inside the mid-band frequencies, ranging from 3 to 6 GHz, like WiFi. In addition to being helpful for more powerful outdoor base stations or small cell hubs for usage within, it covers the medium-range spectrum.

**mmWave:** To facilitate fast data transfer, it has a very high-frequency range of 17 to 110 GHz. It is a short-range technology that is intended for usage in crowded environments.

**Beamforming:** Beamforming is an important technology for addressing the limits in range and direction of the high-frequency waveform spectrum. By employing beamforming, wireless communications can be enhanced in terms of strength, speed, and reliability. It is achieved by directing signals towards consumer devices.

**Massive MIMO:** Utilizing multiple antennas on base stations, data is transferred and received to facilitate many users. The high-frequency networks are now significantly more effective due to this technology. Additionally, beamforming may be coupled with it.

A growing standard, 5G combines more spectrums and offers more bandwidth. Fig. 1 shows the networking spectrum bands, whereas carriers also utilize existing 4G LTE channels, low bands below 1 GHz, and new spectrum in the sub-6 GHz

WiFi region [6]. The C band (3.4–3.6 GHz) was suggested for 5G technology by following a thorough review of the 5G candidate frequency bands below 6 GHz in [7]-[11]. Recently, the most developed nations in the world, such as the United States, Canada, United Kingdom, Japan, China, Korea,

Australia, and several other countries, adopted the specifications of 5G communication technology standards. The global spectrum for Sub-6 GHz 5G systems is briefly described in Table 1 [12]-[16].

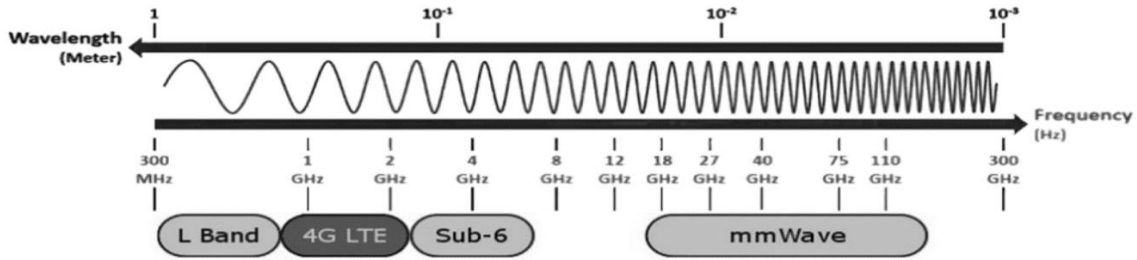


Fig. 1 Networking spectrum bands [6]

Table 1 Global Spectrum Details for Sub-6 GHz 5G [12]-[16]

Countries	(3–4) GHz Band	(4–5) GHz Band	(5–7) GHz Band
China	(3.3 – 3.6) GHz	(4.5 – 5.0) GHz	--
UK	(3.4 – 3.8) GHz	--	--
USA	(3.45 – 3.7) GHz (3.7 – 3.98) GHz	(4.49 – 4.99) GHz	(5.9 – 7.1) GHz
Canada	(3.47 – 3.65) GHz (3.65 – 4.0) GHz	--	(5.9 – 7.1) GHz
Australia	(3.4 – 3.7) GHz	--	--
Italy	(3.6 – 3.8) GHz	--	--
India	(3.4 – 3.6) GHz	--	--
Malaysia	3.5 GHz	--	--
Korea	(3.4 – 3.7) GHz (3.7 – 4.0) GHz	--	--
Japan	(3.6 – 4.1) GHz	(4.5 – 4.9) GHz	--
EU	(3.4 – 3.8) GHz	--	(5.9 – 6.4) GHz

transmission at Sub-6 GHz is challenging. Patch antennas may be a good option for this type of network because of their many benefits, including low profile, affordable price, sustainable gain, ease of fabrication, etc. The signal is fed to the patch antenna through various feeding techniques, including microstrip line, proximity coupled, inset feed, aperture coupled, and coaxial probe feed [18].

In this manuscript, we propose a defected ground slotted patch antenna (DGSPA) using a coaxial feeding technique for 5G services in the Sub-6 GHz frequency band. The main objective of this research is to design a compact high gain 5G smart antenna that operates at Sub-6 GHz and meets the requirements for a variety of 5G wireless applications. The antenna without DGS will operate within the frequency range of (3.6106 - 3.6682) GHz, resonating at 3.6396 GHz with a return loss of -37.916 dB. In the presence of DGS, it resonates at 3.5176 GHz frequency with an excellent return loss of -54.028 dB and operates from 3.4828 GHz to 3.522 GHz frequency range. Due to DGS, the bandwidth of the recommended antenna is increased by 11.6 MHz, and the reflection coefficient is decreased by -16.112 dB. Its impedance profile is  $(50.086 - j0.179) \Omega$ , which denotes perfect impedance matching. Therefore, the proposed patch antenna is suitable for Sub-6 GHz 5G communication services.

2 Literature Review

Numerous research has been conducted and are still working on 5G antennas. Radiofrequency (RF) experts recently created

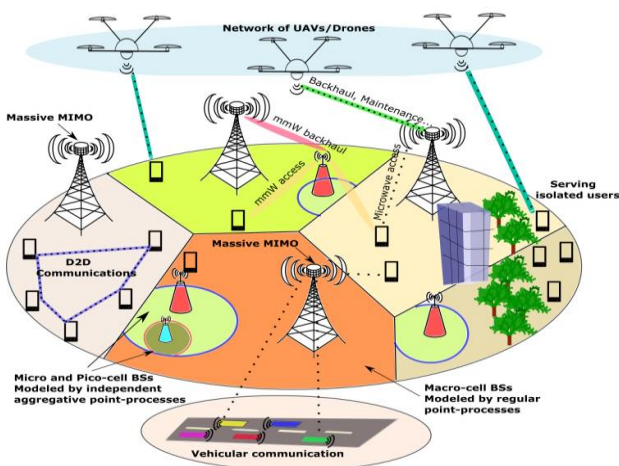


Fig. 2 The primary elements of a typical 5G network architecture [17]

Moreover, micro and macro cells are depicted in a general 5G network in Fig. 2, with the microcells represented by aggregative point processes [17]. An antenna is required for wireless communication systems to transmit and receive data using electromagnetic waves. The antenna serves as an interface between free space and a guiding device. 5G technology necessitates compact antennas with excellent performance. Designing high-performance, small-size antennas for 5G

multiple antennas for 5G sub-6 GHz communications using various methods, i.e., meta-material (MTM), complementary split-ring resonators (CSRR), slot formation, defective ground structure (DGS), artificial dielectric, and many more. The summary information from the research articles and a description of the relevant parameters are discussed below.

The authors of [19] suggested two different types of meta-material (MTM) antennas for 5G IDAS applications. Both antennas can operate at 3.5 GHz. The triangular and rectangular patches that comprise the antenna's radiating structure are combined with two etched complementary split-ring resonators (CSRR) unit cells on the top layer. Both antennas used FR4 material as substrate and have complete ground planes and  $3 \times 3$  cross-slot MTM on the bottom layer. The measured gain characteristics of the two proposed MTM antennas are 2.6 dBi and 2.3 dBi, respectively, which are relatively low. Also, their structures are complicated, although both antennas are small. For 5G wireless applications, a bow-tie patch antenna with DGS is suggested in [20]. The antenna's impedance bandwidth was improved using a defective ground structure (DGS) built on an FR-4 substrate, and the measured impedance bandwidth was 13.37%. At 3.5 GHz, the simulated antenna gain was 8.38 dBi. It has a large volume of  $90 \times 80 \times 1.6 \text{ mm}^3$ , one of its key disadvantages. In [21], a meta-surface hybrid antenna is suggested. It has a huge dimension of  $52.62 \times 40.40 \text{ mm}^2$  but offers excellent impedance bandwidth (185 MHz) and gain (6.74 dB).

The authors of [22] suggest a patch antenna with parasitic strips. It features a low profile and wider bandwidth but a poor gain (0.576 dBi) for 5G services operating at the Sub-7 GHz band. The authors of [23] propose a wideband Y-slot patch antenna with a felt substrate for medical and 5G applications. It combines a fabric-metal barrier operating at 2.4 GHz 65.4% with a low specific absorption rate and a gain of 6.48 dBi. But its overall dimension is relatively large. In [24], a unique miniature 5G antenna is presented using slots and metamaterial components. It has an excellent bandwidth of 774 MHz and a moderate gain of 3.44 dB. A high-gain patch antenna is designed and studied in [25] for mobile TV, radar, and other future wireless applications. It has a narrow band (23.6 MHz) and occupies a huge dimension of  $100 \times 100 \times 1.6 \text{ mm}^3$ .

The authors of [26] proposed a circular patch antenna based on a synthetic dielectric substrate for 5G communications in the Sub-6 GHz range. It has a very good bandwidth (196 MHz) and a 6.391 dB radiation gain at a 3.5 GHz resonant frequency. But its dimensions ( $45 \times 40 \times 4.5 \text{ mm}^3$ ) are comparatively large. In [27], a dual-band slotted shape patch antenna with dimensions of  $50 \times 30 \times 1.57 \text{ mm}^3$  for 5G services is presented. It was constructed on Rogers 5880 material. At the resonant frequencies, there is a radiation gain of 7.52 dBi and 5 dBi, respectively. But it offers both bands a narrow bandwidth. In [28], an array antenna based on a conductive graphene film is presented for 5G services with a 6.77 dBi radiation gain at the resonance frequency. Its volume ( $60 \times 70 \times 1.6 \text{ mm}^3$ ) is relatively very large.

For 5G (C-Band) access point services, the authors of [29] present a high profile ( $88.5 \times 88.5 \times 1.6 \text{ mm}^3$ ) 4-element array antenna, which has been developed on FR4 (Flame Retardant 4) dielectric material. Its radiation efficiency is very poor (approximately 30%), although it offers good impedance bandwidth. Utilizing three different dielectric materials, FR-4, RT-5880, and TLC-30, a rectangular-shaped patch antenna is

proposed in [30]. Design-2 offers a radiation gain of 4.660 at a 3.5 GHz resonant frequency. In [31], another patch antenna for 5G services is introduced utilizing four dielectric materials. The Arlon AD300C material performs the best and offers a radiation gain of 7.15 dBi at 5.65 GHz. But its overall dimension is relatively large. With dimensions of  $47.46 \times 36.57 \times 1.5 \text{ mm}^3$ , a rectangular shape patch antenna for 5G communication systems using rhombic slots is presented in [32]. It has a directivity of 6.158 dBi at a frequency of 3.5305 GHz. A novel metasurface-based patch antenna for Sub-band 5G communication is introduced in [33]. At 4.8 GHz frequency, it provides a high radiation gain and excellent bandwidth (7.68 dBi/220 MHz). But it features a very large volume of  $75 \times 60 \times 15 \text{ mm}^3$ .

A compact ( $32 \times 25 \times 0.254 \text{ mm}^3$ ), flexible CPW-fed patch antenna is presented in [34] specially designed for 3.5 GHz 5G communication and 2.45 GHz ISM band. It has a wide impedance bandwidth (210/1300 MHz) but exhibits a poor radiation gain (1.74, 2.51 dB) in terms of both bands. In [35], a novel fractal geometry-based compact patch antenna for 5G wireless communications was introduced. Over the operational frequency range, it offers a radiation gain of more than 3 dBi and is built on Roger dielectric material. The authors of [36] introduced a letter-slotted dual-band patch antenna for a 5G Sub-6 GHz application. At frequencies of 4.53 GHz and 4.97 GHz, it provides radiation gains of 5 dB and 4.57 dB, respectively. It is printed on the RO5880 dielectric material with a huge dimension ( $77 \times 70.11 \times 1.6 \text{ mm}^3$ ). Moreover, a frequency selective surface (FSS) reflector equipped with a high profile ( $166 \times 66 \times 1.6 \text{ mm}^3$ ) microstrip antenna is proposed in [37] for use in 5G services. Its radiation gain at 4.1 GHz frequency is 12.4 dBi, and its fractional bandwidth is 51.12%.

For LTE/Sub-6 GHz 5G services, a multi-slotted low-profile patch antenna is recommended in [38], which operates from 3.15 to 5.55 GHz frequency. However, its maximum radiation gain in the operational band is only 2.69 dBi. A high-dimensional ( $120 \times 60 \times 0.5 \text{ mm}^3$ ) planar multiband antenna is recommended for GSM, UMTS, LTE, and 5G wireless services [39]. It operates at 900 MHz, 2.4 GHz, 3.5 GHz, and 5.2 GHz. At 2.4 GHz, it exhibits a maximum radiation gain of 4.08 dB. In [40], an octa-band shared aperture square concentric slotted antenna with a size of  $50 \times 50 \times 0.508 \text{ mm}^3$  is presented for mmWave band 5G applications. It has a minimum impedance bandwidth of 180 MHz and exhibits a 10.2 dB gain at 28 GHz. The authors of [41] recommend a novel planar slot antenna with parasitic elements and DGS, which can work on LTE Band 42, WiMAX, and 5G networks. It is relatively small and offers a good radiation gain. However, its bandwidth is very limited (only 19 MHz).

### 3 Design Methodology of the Defected Ground Slotted Patch Antenna

In wireless communication, patch antennas are most typically used to transmit electromagnetic (EM) waves into space. A microstrip patch antenna mainly comprises three basic parts: patch, dielectric substrate, and ground plane. Microstrip antennas are commonly known as patch antennas. The radiating elements and feed lines are typically fabricated by the process of photoetching on the dielectric substrate. Microstrip antennas can be designed using a variety of substrates, both thick and thin. A thick dielectric substrate provides enhanced efficiency, wider bandwidth, and loosely confined fields for radiation into space.

Conversely, a thin dielectric substrate allows for reduced dimensions of the elements. The function of the ground plane between the substrates is to isolate the feed from the radiating element and minimize interference of spurious radiation for pattern formation and polarization purity [42]. It has a ground plane on one side and a dielectric substrate material on the other and can be square, elliptical, circular, rectangular, or even a ring in shape.

### 3.1 Background

The following equations can be used to determine the length  $L$  and width  $W$  of any rectangular patch antenna [20], [22].

$$W = \frac{c}{2f_0\sqrt{\frac{\epsilon_r + 1}{2}}} \quad (1)$$

where  $\epsilon_r$  denotes the dielectric constant and  $f_0$  is the resonance frequency. The radiation propagates through the atmosphere and partially penetrates the substrate to reach the ground. Because the dielectric constants of the air and the substrate are different from each other, it is necessary to consider an effective dielectric constant ( $\epsilon_{eff}$ ), which is determined using the provided equation [22].

$$\epsilon_{eff} = \frac{\epsilon_r + 1}{2} + \frac{\epsilon_r - 1}{2} \left[1 + \frac{12h}{W}\right]^{-1/2} \quad (2)$$

where  $h$  represents the substrate thickness. The patch length is determined by utilizing the following equation [22].

$$L = \frac{c}{2f_0\sqrt{\epsilon_{eff}}} \quad (3)$$

Due to fringing, the antenna's size is expanded electrically by a factor of  $\Delta L$ . The longer length is provided by,

$$\Delta L = 0.412h \frac{(\epsilon_{eff} + 0.3)\left(\frac{W}{h} + 0.264\right)}{(\epsilon_{eff} - 0.258)\left(\frac{W}{h} + 0.8\right)} \quad (4)$$

Eqs. (5) and (6) are used to determine the substrate's minimal length ( $L_{sub}$ ) and width ( $W_{sub}$ ).

$$L_{sub} = 6h + L \quad (5)$$

$$W_{sub} = 6h + W \quad (6)$$

On the FR-4 dielectric substrate, an inset feed microstrip patch antenna employing copper is built using the above formulae [22]. The slotted rectangular shapes are etched on the patch after several optimizations. As the antenna is made for several observable frequencies, only its length and width must be altered; the basic structure is the same for all.

### 3.2 Proposed Antenna Design

A microstrip patch antenna is formed by etching out a metallic patch on a dielectric substrate material. On a ground plane, the dielectric material is mounted. A ground plane is a horizontal conducting surface that is flat or almost flat and used as part of an antenna in communications to reflect radio waves from other antenna elements.

Selecting the substrate is the priority in designing an antenna. The attributes of the substrate, such as the dielectric constant ( $\epsilon_r$ ), tangent loss ( $\tan\delta$ ), and thickness ( $t_s$ ) have an impact on the impedance matching and the bandwidth of an

antenna. A very thin substrate may result in high copper losses, but a thicker substrate may degrade the antenna's performance because of surface waves. Due to its low dielectric constant and loss dispersion, Roger RT5880 dielectric material is utilized as the substrate layer for developing the suggested antenna. It is a suitable material for UHF and SHF applications. Its electrical properties are presented in Table 2.

Table 2 Electrical Properties of Rogers RT5880 Dielectric Material

Name of the attributes	Values
Dielectric constant ( $\epsilon_r$ )	2.2
Tangent loss ( $\tan \delta$ )	0.0009
Thermal cond.	0.2 [W/K/m]

One of the most widely used types of microstrip antennas is the rectangular patch antenna. Several strategies are utilized to improve the radiation properties of the patch antenna. Slot structure on the patch and defective ground structure (DGS) are the most frequently employed. For microstrip antennas, coaxial feed is among the most used feeding techniques.

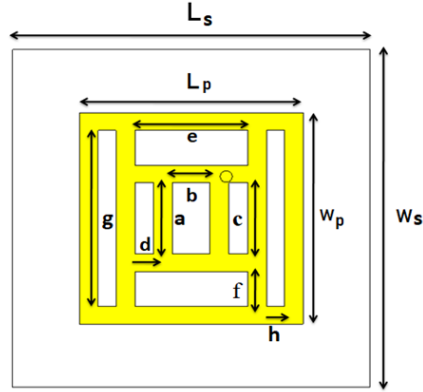
Fig. 3 depicts the geometrical structure of the proposed slotted patch antenna along with its complete ground plane. Using the CST-MWS Simulation Tool, the suggested design and simulation have been performed. Fig. 3(a) and (b) show the top and bottom layers of the antenna, respectively. It comprises a multiple-slotted square patch, Roger RT5880 dielectric substrate layer with a thickness of 1.575 mm, and a complete ground surface. As the ground plane and radiating patch, copper material with a thickness of 0.02 mm is utilized. The optimized dimension of the antenna is  $38 \times 38 \times 1.575 \text{ mm}^3$ . Many rectangular slots have been introduced into the square patch to improve the antenna's performance and shift the operating frequency into the desired Sub-6 GHz application band. The square-shaped radiating patch contains seven rectangular slots divided into four different types. The patch's dimensions ( $L_p \times W_p$ ) is  $23.76 \times 23.76 \text{ mm}^2$ . Table 3 presents the parameters of the recommended patch antenna.

Table 3 Parameters of the recommended patch antenna

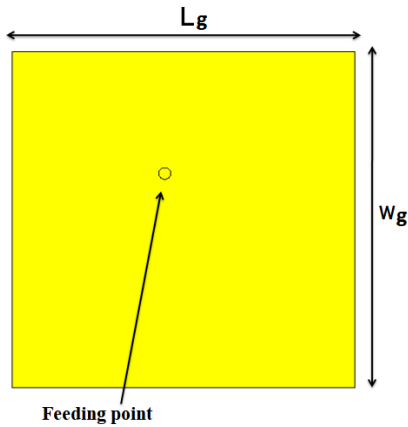
Parameters	Dimensions (mm)	Descriptions
$L_s$	38	The length of the substrate
$W_s$	38	The width of the substrate
$L_g$	38	The ground plane length
$W_g$	38	The ground plane width
$t_s$	1.575	The thickness of the substrate
$t_g$	0.02	Thickness of the copper ground plane
$L_p$	23.76	Square patch length
$W_p$	23.76	Square patch width
$t_p$	0.02	Thickness of the copper patch
$x$	3.71	Distance of feeding point from X-axis
$y$	4.7	Distance of feeding point from Y-axis

In Fig. 3(a), the central rectangular slot with dimensions ( $a \times b$ ) of  $8 \times 4 \text{ mm}^2$  is considered the first type-rectangular

slot. However, the second type-rectangular slots, are the two identically sized ( $c \times d = 8 \times 1.9 \text{ mm}^2$ ) slots on both sides of the central slot. Additionally, the upper and lower sides of two rectangular slots from the first type-rectangular slot are the third type of rectangular slot and possess the same dimensions ( $e \times f = 12 \times 3.9 \text{ mm}^2$ ). The two rectangular slots located on either side of the third type slot are the fourth type-rectangular slots that are similar in size.



(a) Top layer



(b) Bottom layer

Fig. 3 The geometrical structure of the recommended slotted patch antenna with the complete ground plane (without DGS) (a) Top layer (b) Bottom layer

Table 4 presents the dimension details of different rectangular slots. It is excited using a coaxial  $50 \Omega$  probe feed. The feeding location of the coaxial probe is indicated by the little circle that is situated in the patch and ground plane. The feed is placed at 3.71 mm and 4.7 mm distances from the  $X$  and  $Y$  axes to ensure impedance matching, respectively.

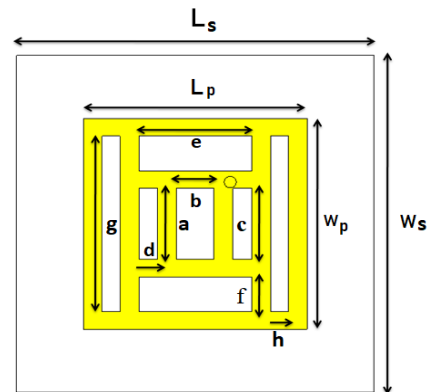
An emerging technique called defected ground structure (DGS) improves the narrow bandwidth, return loss, high selectivity, impedance profile, and other characteristics of antennas, filters, and other microwave components [20], [32]. With all the dimensions remaining the same, the suggested slotted patch antenna is then applied to the defected ground surface to improve the performance characteristics shown in Fig. 4. A rectangular slot with the dimension ( $p \times q$ ) of  $9 \times 7 \text{ mm}^2$  has been introduced into the copper ground plane. This rectangular shape of DGS has been used to disturb the electric field (E-field) on the ground surface. Table 5 depicts the dimensions of the ground plane's rectangular slot. The top and

bottom layers of the defective ground slotted patch antenna (DGSPA) are demonstrated in Fig. 4(a) and (b) respectively.

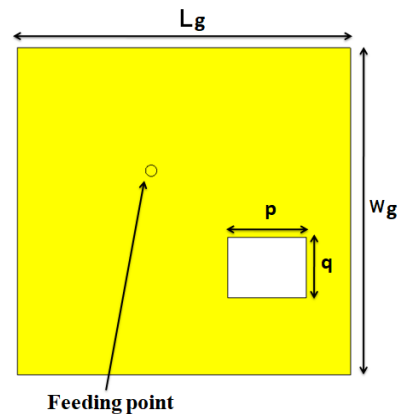
Table 4 Dimension details of different rectangular slots

Parameters	Dimensions (mm)	Descriptions
$a$	8	Length of the 1 <sup>st</sup> type of rectangular slot
$b$	4	Width of the 1 <sup>st</sup> type of rectangular slot
$c$	8	Length of the 2 <sup>nd</sup> type rectangular slot
$d$	1.9	Width of the 2 <sup>nd</sup> type rectangular slot
$e$	12	Length of the 3 <sup>rd</sup> type rectangular slot
$f$	3.9	Width of the 3 <sup>rd</sup> type rectangular slot
$g$	19.8	Length of the 4 <sup>th</sup> type rectangular slot
$h$	1.9	Width of the 4 <sup>th</sup> type rectangular slot

After slotting the ground surface, the performance characteristics of the proposed antenna are significantly changed. The performance of the antenna with DGS is significantly better than that of the antenna without DGS, which is elaborately discussed in the simulation result section. The comparative findings of the proposed antenna without DGS and with DGS are shown in Table 6.



(a) Top layer



(b) Bottom layer

Fig. 4 The geometrical structure of the recommended ground slotted patch antenna (with DGS) (a) Top Layer (b) Bottom Layer

Table 5 Dimensions of the ground plane’s rectangular slot

Parameter	Dimension (mm)	Description
$p$	9	Length of the rectangular slot in the ground plane
$q$	7	Width of the rectangular slot in the ground plane

4 Simulated Results and Performance Analysis

The recommended slotted 5G patch antenna had been designed and simulated using the 3D simulation software CST Microwave Studio 2017v. In this section, the performance parameters of the recommended antenna, such as reflection coefficient, radiation pattern, impedance profile, efficiency, E-field distribution, etc., are elaborately discussed based on the simulation results.

4.1 Reflection Coefficient, Bandwidth, and VSWR

The S-parameter’s ( $S_{1,1}$ ) magnitude, measured in decibels (dB), represents the return loss. Fig. 5 depicts the return loss ( $|S_{1,1}|$ ) graph for the suggested slotted 5G patch antenna in both the “without DGS” and “with DGS” cases. In the absence of DGS (without DGS), the antenna operates from 3.6106 GHz to 3.6682 GHz frequency, offering an impedance bandwidth of 57.6 MHz and resonating at 3.6396 GHz with a return loss of -37.916 dB. In the presence of DGS (with DGS), it operates from 3.4828 GHz to 3.552 GHz frequency and resonates at 3.5176 GHz with an excellent return loss of -54.028 dB. Therefore, the impedance bandwidth is increased by 11.6 MHz because of introducing DGS, and the return loss is decreased by -16.112 dB.

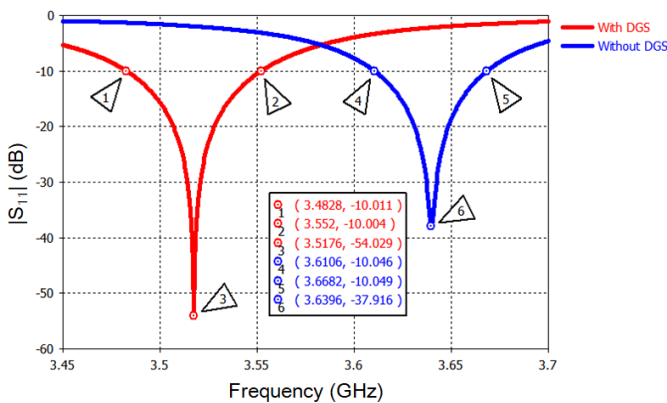


Fig. 5 The suggested slotted 5G patch antenna’s return loss ( $|S_{1,1}|$ ) graph for both the “without DGS” and “with DGS” scenarios

Voltage standing wave ratio (VSWR) indicates how mismatched an antenna and its feeding component are. For antenna and RF applications, the value of VSWR should be less than 2. But unity (VSWR = 1) VSWR ensures the antenna’s impedance is properly matched. The VSWR of the suggested model for both cases is shown in Fig. 6. When DGS is absent, the antenna’s VSWR is 1.0276. When DGS is present, the antenna exhibits approximately unity VSWR ( $1.004 \approx 1$ ), which

is an improvement above the value of VSWR when DGS is not present. Also, it ensures proper impedance matching for the antenna.

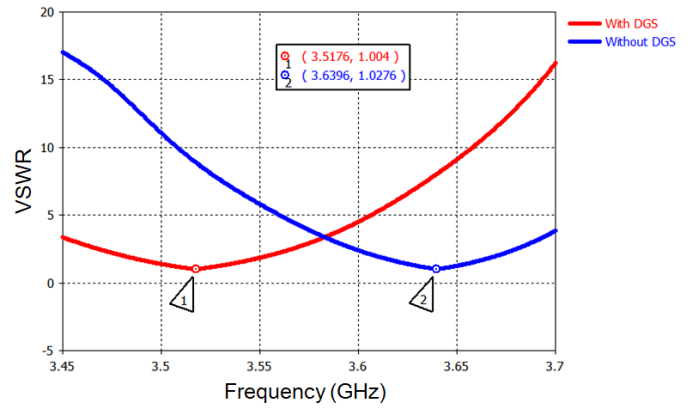
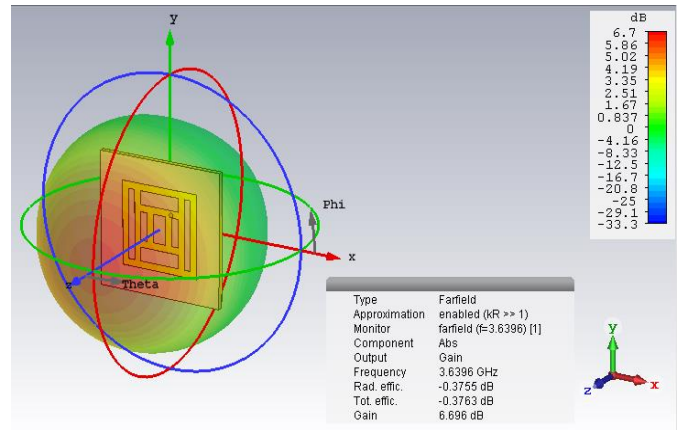


Fig. 6 The VSWR graph of the suggested slotted 5G patch antenna for both the “without DGS” and “with DGS” scenarios

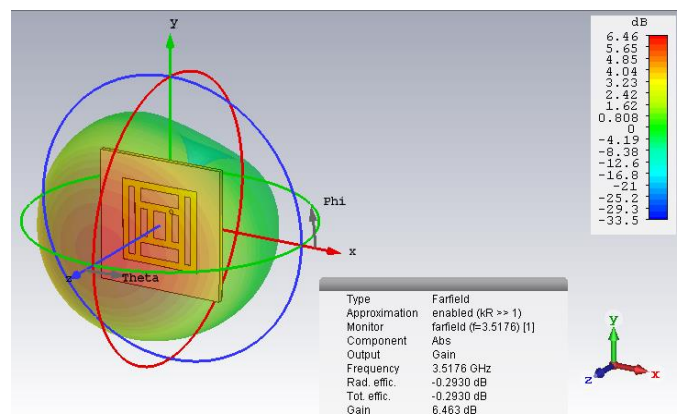
4.2 Radiation Pattern, Gain and Directivity

An antenna’s radiation pattern shows the mode of energy transmission or reception. On the other hand, the radiation gain of an antenna describes how well it converts the power input into radio waves and directs it in a specific direction or how well it converts radio waves from a certain direction into electrical energy.

Fig. 7 shows the simulated 3D gain of the recommended slotted patch antenna. The antenna exhibits a 3D radiation gain of 6.463 dB in the presence of DGS at the resonant frequency of 3.5176 GHz. On the other hand, the beam gain without the DGS structure of the antenna is depicted as 6.696 dB.



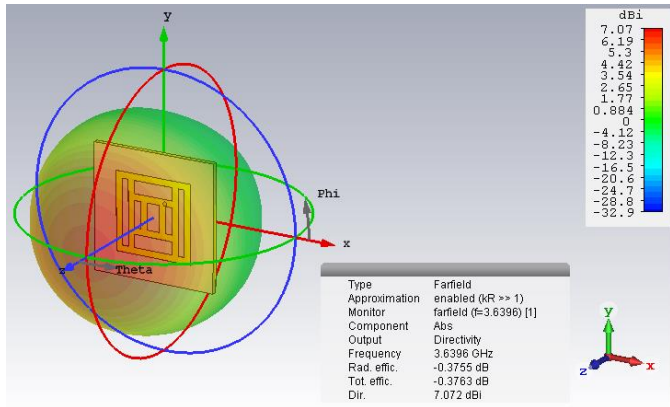
(a) Without DGS



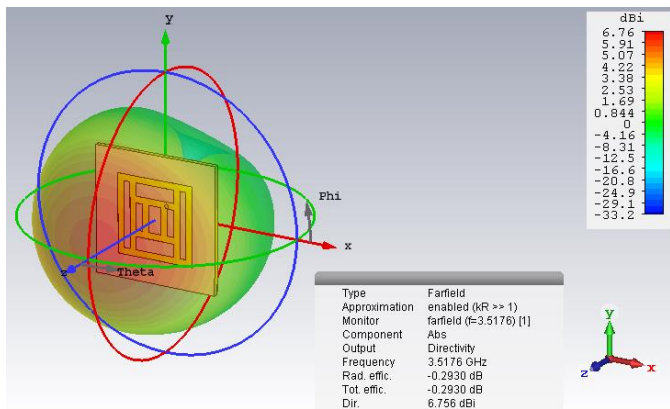
(a) With DGS

Fig. 7 3D radiation gains of the suggested slotted 5G patch antenna model (a) Without DGS (b) With DGS

Moreover, the antenna's main lobe defines the direction of maximum radiation, known as directivity. As seen in Fig. 8, the 3D directivity by applying the DGS technique at the resonance frequency of 3.5176 GHz is 6.756 dBi. Without slotting the ground, its directivity is 7.072 dBi.



(a) Without DGS



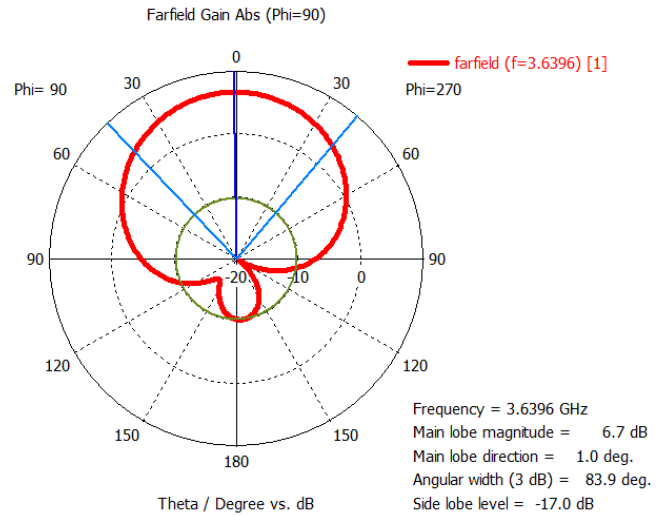
(b) With DGS

Fig. 8 3D directivity of the suggested slotted 5G patch antenna model (a) Without DGS (b) With DGS

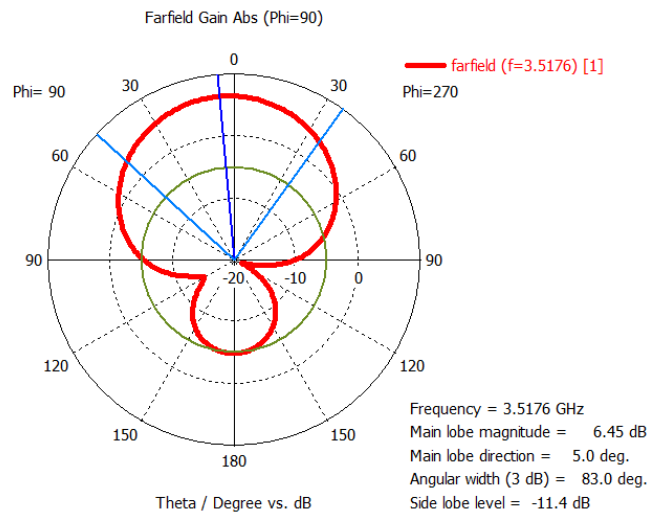
An antenna's radiating farfield term is the region where the effective radiation pattern is observed. Fig. 9(a) and (b) demonstrate the polar radiation pattern (Farfield gain Abs) for both cases when  $\phi = 90^\circ$ . Without DGS, the major lobe's magnitude, and angular width (3 dB) at 3.6396 GHz are 6.7 dB and 83.9°, respectively. As seen in Fig. 9(b), the main lobe's magnitude and angular width (3 dB) at the resonance frequency of 3.5176 GHz are 6.45 dB and 83°, respectively, in the presence of DGS. In addition, its side lobe level is -11.4 dB.

Alternatively, when  $\phi = 0^\circ$ , the polar radiation pattern (Farfield Directivity Abs) for both cases is illustrated in Fig. 10(a) and (b). The main lobe has a magnitude level of 7.07 dBi and a direction of  $0^\circ$  in the absence of DGS, as shown in Fig. 10(a). Additionally, the angular width and side lobe level are 88.6° and -17 dB, respectively. Fig. 10(b) shows that the major lobe in the presence of DGS has a magnitude level of 6.71 dBi, and the angular width is 92°. Moreover, its direction is  $3^\circ$ , and the side lobe level is -11.3 dB. The directive pattern's angular beam width at 3 dB is higher than the gain pattern, both with and

without slotting. On the other hand, the side lobe values for the gain and directive pattern are reversely equal before and after slotting.

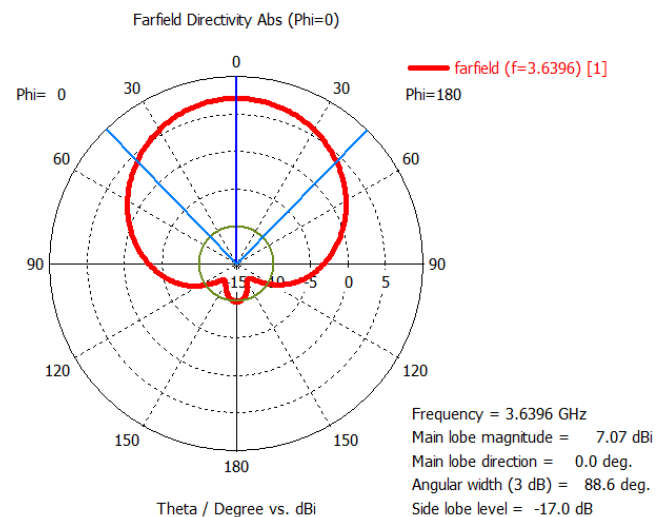


(a) Without DGS



(b) With DGS

Fig. 9 Farfield (2-D) gain pattern of the suggested slotted patch antenna when  $\phi=90^\circ$  (a) Without DGS (b) With DGS



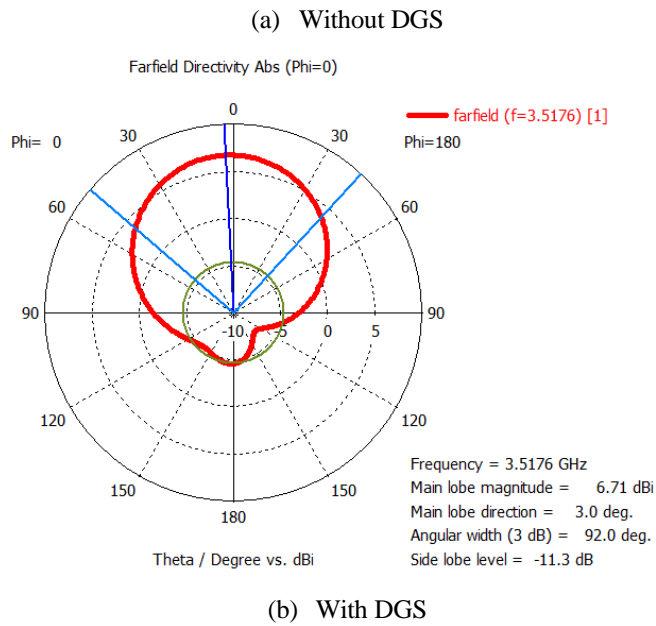


Fig. 10 Farfield (2-D) gain pattern of the suggested slotted patch antenna when  $\phi=0^\circ$  (a) Without DGS (b) With DGS

The suggested antenna’s gain versus frequency 1-D linear graph is shown in Fig. 11 for both cases. Without slotting the ground plane, its gain is 6.6959 dB. Applying the DGS technique results in a gain of 6.4628 dB at a resonance frequency of 3.5176 GHz. Fig. 12 shows a 1D linear graph of the antenna’s directivity versus frequency. The antenna’s directivity is 6.7486 dBi and 7.0706 dBi, respectively, with and without DGS. As a result, after slotting the ground, the gain and directive values are reduced.

### 4.3 Impedance Profile, Efficiency, Surface Current, and E-field

The proposed defected ground slotted patch antenna (DGSPA), also known as the antenna with DGS, has an impedance profile (Z-Parameter) of  $(50.086 - j0.179) \Omega$ , which is shown in Fig. 13. It denotes  $50 \Omega$  pure resistivity at the resonance frequency of 3.5176 GHz. Fig. 14 demonstrates the proposed antenna model’s radiation efficiency versus frequency graph. The antenna’s efficiency when DGS is not present is 91.718%. After using the DGS technique, the suggested antenna’s efficiency has increased; at the resonant frequency, the efficiency is approximately 93.475%.

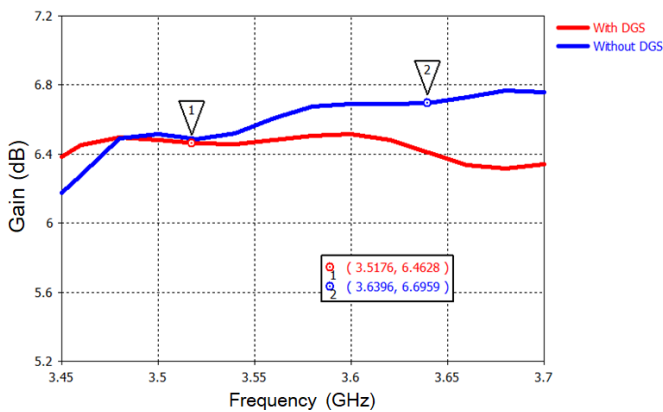


Fig. 11 Gain versus frequency 1-D linear graph for both the “without DGS” and “with DGS” scenarios of the proposed slotted 5G patch antenna

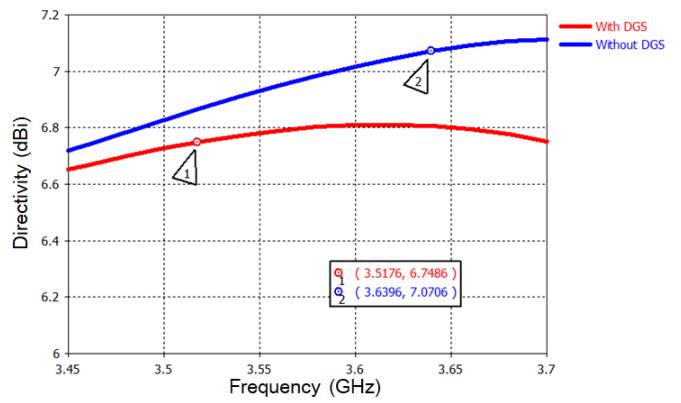


Fig. 12 Directivity versus frequency 1-D linear graph for both the “without DGS” and “with DGS” scenarios of the proposed slotted 5G patch antenna

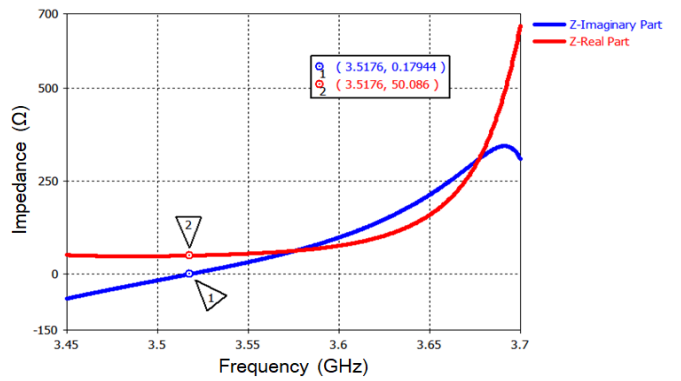


Fig. 13 Impedance profile of the proposed defected ground slotted patch antenna (DGSPA) at 3.5176 GHz resonant frequency

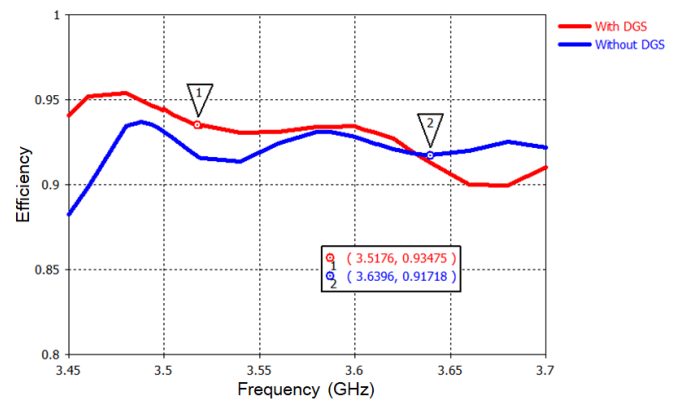


Fig. 14 Efficiency versus frequency graph for both the “without DGS” and “with DGS” scenarios of the suggested slotted patch antenna

The current distribution through the patch of the proposed 5G patch antenna at 3.5176 GHz (with DGS) and 3.6396 GHz (without DGS) frequency is depicted in Fig. 15. On the radiating patch, a strong surface current distribution is noticed around the rectangular slots that are mainly responsible for creating the 5G frequency band. Through the patch, the red color indicates the highest current density, while the blue hue indicates the lowest current density. It is seen that after slotting, the current density through the patch is increased. Fig. 15(a) shows a strong electric current through the patch at 3.5176 GHz frequency.

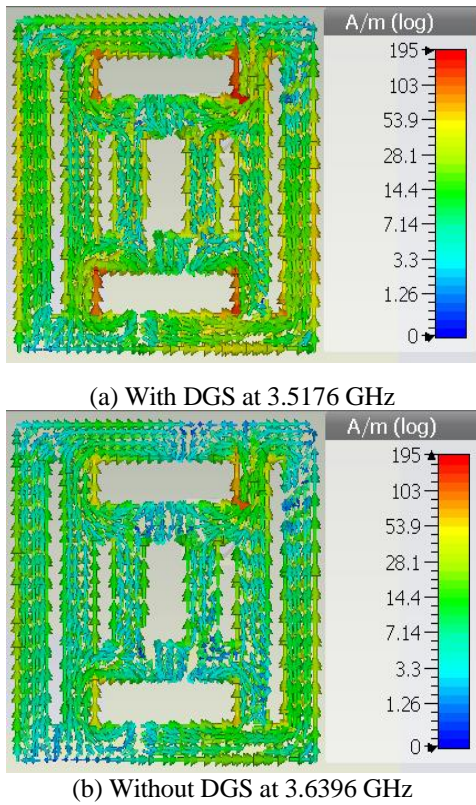


Fig. 15 Current distributions through the patch of the suggested 5G antenna (a) With DGS (b) Without DGS

The distributions of the E-field through the designed antenna at 3.5176 GHz (with DGS) and 3.6396 GHz (without DGS) frequency are shown in Fig. 16.

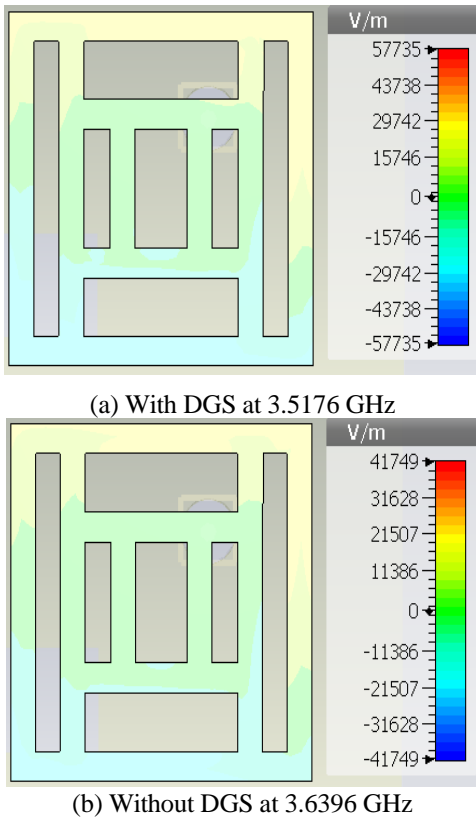


Fig. 16 Distributions of the E-field within the proposed patch antenna (a) With DGS (b) Without DGS

A strong distribution of the E-field is obtained at the 3.5176 GHz frequency band. An approximately 57735 V/m E-field present through the antenna patch at this frequency is illustrated in Fig. 16(a). During 3.6396 GHz frequency, an approximately 41749 V/m E-field exists at the antenna patch. Nevertheless, it has been seen that the E-field is focused within the patch and at the outer edges of the radiating patch. It forms the energy loop and enables effective radiation. Moreover, the E-field around the patch is very high after ground slots compared to the shape without slotting. The comparative study of the suggested slotted 5G patch antenna for both with and without DGS is presented in Table 6.

Table 6 The comparative findings of the proposed slotted patch antenna without DGS and with DGS

Proposed antenna	Without DGS	With DGS
Frequency (GHz)	3.6396	3.5176
Return loss (dB)	-37.916	-54.028
VSWR	1.0276	1.004
Bandwidth (MHz)	57.6	69.2
Gain (dB)	6.696	6.463
Efficiency	91.718%	93.475%

### 5 Comparison with Relevant Work

For use in 5G wireless applications, several types of antennas are presented in the literature [19]-[41], some of which are larger or have lower performance. Small antennas with improved performance are required for 5G communication technology. In Table 7, there is a comparison of the recommended defected ground slotted patch antenna (DGSPA) with the previously published works. In terms of the reflection coefficient ( $|S_{1,1}|$ ), impedance bandwidth, radiation gain, impedance profile, radiation efficiency, etc., the recommended antenna model exhibits excellent performance.

Table 7 Comparison of the recommended defected ground slotted patch antenna (DGSPA) with several relevant previous works

Ref.	Antenna Size (mm <sup>3</sup> )	Frequency (GHz)	BW (MHz)	Gain (dB)
[19]	34 × 18 × 1.6	3.5	100	2.6
[25]	100 × 100 × 1.6	3.5	23.6	7.55
[26]	45 × 40 × 4.5	3.5	196	6.391
[27]	50 × 30 × 1.575	3	50	7.52
		3.3	50	5
[28]	60 × 70 × 1.6	3.51	~100	6.77
[30]	47 × 31.69 × 1.575	3.50	129.7	4.660
[31]	52.92 × 55.56 × 1.2	5.65	135	7.15
[32]	47.46 × 36.57 × 1.5	3.5305	116.4	N/A
[41]	32.4 × 27.9 × 1.6	3.5	19	4.2
<b>This Work</b>	38 × 38 × 1.575	3.5176	69.2	6.46

## 6 Conclusions

In this article, a coaxial-fed defected ground slotted patch antenna (DGSPA) is suggested for Sub-6 GHz 5G services. The proposed antenna's dimension is  $38 \times 38 \text{ mm}^2$  with a thickness of 1.575 mm, and Rogers RT5880 material is utilized as the substrate layer to construct it. It can operate in the LTE Band 42, WiMAX, and the 5G N77 band. The special features of the recommended antenna are its compact size, proper impedance matching, improved impedance bandwidth, high efficiency, and high gain of the antenna. The antenna without DGS resonates at 3.6396 GHz with a return loss ( $|S_{1,1}|$ ) of -37.916 dB, offering a bandwidth of 57.6 MHz. The operational frequency range of the antenna with DGS is from 3.4828 GHz to 3.552 GHz and has an excellent return loss of -54.028 dB at 3.5176 GHz resonance frequency and approximately unity ( $1.004 \approx 1$ ) VSWR. Because of introducing DGS, 11.6 MHz increases the impedance bandwidth, and the return loss is decreased by -16.112 dB. Also, the DGS-backed antenna has an excellent impedance profile of  $(50.086 - j0.179) \Omega$ , which denotes  $50 \Omega$  pure resistivity. Additionally, it exhibits a radiation gain of 6.463 dB and a radiation efficiency of 93.475% at the resonance frequency point. The suggested antenna would be a good option for use in 5G services due to its small size and excellent performance features.

## References

- [1] AIRikabi, H.T.S., Alaidi, A.H., Abdalrada, A.S. and Abed, F.T., 2019. Analysis the Efficient Energy Prediction for 5G Wireless Communication Technologies. *Int. J. Emerg. Technol. Learn.*, 14(8), pp.23-37.
- [2] Habibi, M.A., Nasimi, M., Han, B. and Schotten, H.D., 2019. A comprehensive survey of RAN architectures toward 5G mobile communication system. *Ieee Access*, 7, pp.70371-70421.
- [3] Ullah, R., Ullah, S., Ullah, R., Faisal, F., Mabrouk, I.B. and Al Hasan, M.J., 2020. A 10-ports MIMO antenna system for 5G smart-phone applications. *IEEE access*, 8, pp.218477-218488.
- [4] Talukder, A. and Islam, E., 2021, December. Design and simulation study of e shaped slotted microstrip patch antenna by HFSS for 5G applications. In *2021 IEEE International Symposium on Antennas and Propagation and USNC-URSI Radio Science Meeting (APS/URSI)* (pp. 1909-1910). IEEE.
- [5] Attaran, M., 2023. The impact of 5G on the evolution of intelligent automation and industry digitization. *Journal of ambient intelligence and humanized computing*, 14(5), pp.5977-5993.
- [6] Attaran, M. and Attaran, S., 2020. Digital transformation and economic contributions of 5G networks. *International Journal of Enterprise Information Systems (IJEIS)*, 16(4), pp.58-79.
- [7] Biddut, N.H., Haque, M.E. and Jahan, N., 2022, March. A wide band microstrip patch antenna design using multiple slots at v-band. In *2022 International Mobile and Embedded Technology Conference (MECON)* (pp. 113-116). IEEE.
- [8] Rahman, M.M. and Ryu, H.G., 2021, October. Compact multiple wideband slotted circular patch antenna for satellite and millimeter-wave communications. In *2021 International Conference on Information and Communication Technology Convergence (ICTC)* (pp. 233-236). IEEE.
- [9] Nahas, M., 2022. Design of a high-gain dual-band LI-slotted microstrip patch antenna for 5G mobile communication systems. *Journal of Radiation Research and Applied Sciences*, 15(4), p.100483.
- [10] Saif, H.M., Abdo, E.A., Qahtan, A.H. and Shaddad, R.Q., 2021, August. Improved Performance in Compact Antenna by Using E-slotted and DGS for V and E band 5G Applications. In *2021 1st International Conference on Emerging Smart Technologies and Applications (eSmarTA)* (pp. 1-4). IEEE.
- [11] Moussa, F.Z., Ferouani, S., Belhadeif, Y. and Abdellaoui, G., 2021, December. New design of miniature rectangular patch antenna with DGS for 5G mobile communications. In *2021 International Conference on Information Systems and Advanced Technologies (ICISAT)* (pp. 1-5). IEEE.
- [12] Hasan, M.M., Islam, M.T., Samsuzzaman, M., Baharuddin, M.H., Soliman, M.S., Alzamil, A., Abu Sulayman, I.I. and Islam, M.S., 2022. Gain and isolation enhancement of a wideband MIMO antenna using metasurface for 5G sub-6 GHz communication systems. *Scientific reports*, 12(1), p.9433.
- [13] Prasad, B.S.H. and Prasad, M.V., 2020. Design and analysis of compact periodic slot multiband antenna with defected ground structure for wireless applications. *Progress In Electromagnetics Research M*, 93, pp.77-87.
- [14] Khandelwal, M.K., Kanaujia, B.K. and Kumar, S., 2017. Defected ground structure: fundamentals, analysis, and applications in modern wireless trends. *International Journal of Antennas and Propagation*, 2017.
- [15] Gopi, D., Vadaboyina, A.R. and Dabbakuti, J.K., 2021. DGS based monopole circular-shaped patch antenna for UWB applications. *SN Applied Sciences*, 3(2), p.198.
- [16] Nahas, M., 2022. A super high gain l-slotted microstrip patch antenna for 5G mobile systems operating at 26 and 28 GHz. *Engineering, Technology & Applied Science Research*, 12(1), pp.8053-8057.
- [17] Hmamouche, Y., Benjillali, M. and Saoudi, S., 2018, November. Closed-form Coverage Probability under the Idle Mode Capability: A Stochastic Geometry Approach. In *2018 9th International Symposium on Signal, Image, Video and Communications (ISIVC)* (pp. 135-140). IEEE.
- [18] Irfansyah, A., Harianto, B.B. and Pambudiyatno, N., 2021, November. Design of rectangular microstrip antenna 1x2 array for 5G communication. In *Journal of Physics: Conference Series* (Vol. 2117, No. 1, p. 012028). IOP Publishing.
- [19] Karimbu Vallappil, A., Khawaja, B.A., Rahim, M.K.A., Iqbal, M.N. and Chattha, H.T., 2022. Metamaterial-inspired electrically compact triangular antennas loaded with CSRR and  $3 \times 3$  cross-slots for 5G indoor distributed antenna systems. *Micromachines*, 13(2), p.198.
- [20] Astuti, D.W., Fadilah, R., Muslim, D.R., Rusdiyanto, D., Alam, S. and Wahyu, Y., 2022. Bandwidth Enhancement of Bow-tie Microstrip Patch Antenna Using Defected Ground Structure for 5G. *J. Commun.*, 17(12), pp.995-1002.

- [21] Fadhil, T.Z., Murad, N.A., Rahim, M.K.A., Hamid, M.R. and Nur, L.O., 2021. A beam-split metasurface antenna for 5G applications. *IEEE Access*, 10, pp.1162-1174.
- [22] Noor, S.K., Jusoh, M., Sabapathy, T., Rambe, A.H., Vettikalladi, H., M. Albishi, A. and Himdi, M., 2023. A Patch Antenna with Enhanced Gain and Bandwidth for Sub-6 GHz and Sub-7 GHz 5G Wireless Applications. *Electronics*, 12(12), p.2555.
- [23] Hashim, F.F., Mahadi, W.N.L.B.W., Abdul Latef, T.B. and Othman, M.B., 2023. Fabric–Metal Barrier for Low Specific Absorption Rate and Wide-Band Felt Substrate Antenna for Medical and 5G Applications. *Electronics*, 12(12), p.2754.
- [24] Moussa, F.Z., Ferouani, S. and Belhadef, Y., 2022. New Design of Metamaterial Miniature Patch Antenna with DGS for 5G Mobile Communications. *Microwave Review*, 28(2).
- [25] Rana, M.S., Islam, S.I., Al Mamun, S., Mondal, L.K., Ahmed, M.T. and Rahman, M.M., 2022. An S-Band Microstrip Patch Antenna Design and Simulation for Wireless Communication Systems. *Indonesian Journal of Electrical Engineering and Informatics (IJEI)*, 10(4), pp.945-954.
- [26] Rahmawati, Y.N. and Ludiyati, H., 2021, November. The characteristic of a 3.5 GHz circular patch antenna using open-ring artificial dielectric. In *2nd International Seminar of Science and Applied Technology (ISSAT 2021)* (pp. 387-393). Atlantis Press.
- [27] Amjad, Q., Kamran, A., Tariq, F. and Karim, R., 2019, November. Design and characterization of a slot based patch antenna for Sub-6 GHz 5G applications. In *2019 Second International Conference on Latest trends in Electrical Engineering and Computing Technologies (INTELLECT)* (pp. 1-6). IEEE.
- [28] Song, R., Huang, G.L., Liu, C., Zhang, N., Zhang, J., Liu, C., Wu, Z.P. and He, D., 2019. High-conductive graphene film based antenna array for 5G mobile communications. *International Journal of RF and Microwave Computer-Aided Engineering*, 29(6), p.e21692.
- [29] Chen, W.S. and Lin, Y.C., 2018, August. Design of  $2 \times 2$  Microstrip Patch Array Antenna for 5G C-Band Access Point Applications. In *2018 IEEE International Workshop on Electromagnetics: Applications and Student Innovation Competition (iWEM)* (pp. 1-2). IEEE.
- [30] Ramli, N., Noor, S.K., Khalifa, T. and Abd Rahman, N.H., 2020. Design and performance analysis of different dielectric substrate based microstrip patch antenna for 5G applications. *International Journal of Advanced Computer Science and Applications*, 11(8).
- [31] Tütüncü, B. and Kösem, M., 2022. Substrate analysis on the design of wide-band antenna for sub-6 GHz 5G communication. *Wireless Personal Communications*, 125(2), pp.1523-1535.
- [32] Hakanoglu, B.G., Sen, O., Koc, B., Hayber, S.E. and Turkmen, M., 2020, August. Defected Grounded Rectangular Patch Antenna with Rhombic-Shaped Slots for Early Phase 5G Applications. In *2020 XXXIIIrd General Assembly and Scientific Symposium of the International Union of Radio Science* (pp. 1-4). IEEE.
- [33] Ashfaq, M., Bashir, S., Shah, S.I.H., Abbasi, N.A., Rmili, H. and Khan, M.A., 2022. 5G antenna gain enhancement using a novel metasurface. *Computers, Materials & Continua*, 72(2), pp.3601-3611.
- [34] Awan, W.A., Hussain, N., Ghaffar, A., Zaidi, A. and Li, X.J., 2020, February. A compact flexible antennas for ISM and 5G sub-6-GHz band Application. In *WSA 2020; 24th International ITG Workshop on Smart Antennas* (pp. 1-3). VDE.
- [35] Rizvi, S.N.R., Mazher, A., Chaudary, E., Alibakhshikenari, M., Falcone, F. and Limiti, E., 2021, August. Wideband Small Fractal Antenna with Simple Design Strategy for 5G Sub-6-GHz Wireless Communications. In *2021 XXXIVth General Assembly and Scientific Symposium of the International Union of Radio Science (URSI GASS)* (pp. 1-4). IEEE.
- [36] Sree, M.F.A., Abd Elazeem, M.H. and Swelam, W., 2021, December. Dual Band Patch Antenna Based on Letter Slotted DGS for 5G Sub-6GHz Application. In *Journal of Physics: Conference Series* (Vol. 2128, No. 1, p. 012008). IOP Publishing.
- [37] Alwareth, H., Ibrahim, I.M., Zakaria, Z., Al-Gburi, A.J.A., Ahmed, S. and Nasser, Z.A., 2022. A wideband high-gain microstrip array antenna integrated with frequency-selective surface for Sub-6 GHz 5G applications. *Micromachines*, 13(8), p.1215.
- [38] Azim, R., Meaze, A.M.H., Affandi, A., Alam, M.M., Aktar, R., Mia, M.S., Alam, T., Samsuzzaman, M. and Islam, M.T., 2021. A multi-slotted antenna for LTE/5G Sub-6 GHz wireless communication applications. *International Journal of Microwave and Wireless Technologies*, 13(5), pp.486-496.
- [39] Khalilabadi, A.J. and Zadehgo, A., 2018, March. Multiband antenna for wireless applications including GSM/UMTS/LTE and 5G bands. In *2018 International Applied Computational Electromagnetics Society Symposium (ACES)* (pp. 1-2). IEEE.
- [40] Hussain, R., 2021. Shared-aperture slot-based sub-6-GHz and mm-wave IoT antenna for 5G applications. *IEEE Internet of Things Journal*, 8(13), pp.10807-10814.
- [41] Chowdhury, M.Z.B., Islam, M.T., Rmili, H., Hossain, I., Mahmud, M.Z. and Samsuzzaman, M., 2022. A low-profile rectangular slot antenna for sub-6 GHz 5G wireless applications. *International Journal of Communication Systems*, 35(17), p.e5321.
- [42] Balanis, C.A., 2016. *Antenna theory: analysis and design*. John Wiley & sons.

This page is left intentionally blank

# Journal of Engineering Advancements (JEA)

DOI: <https://doi.org/10.38032/jea>

---

Indexed by:



Volume 04 Issue 04

DOI: <https://doi.org/10.38032/jea.2023.04>

---

**Published by: SciEn Publishing Group**

Website: [www.scienpg.com](http://www.scienpg.com)